DEFORMABLE MODELS WITH APPLICATION TO HUMAN CEREBRAL CORTEX RECONSTRUCTION FROM MAGNETIC RESONANCE IMAGES

by

Chenyang Xu

A dissertation submitted to the Johns Hopkins University in conformity with the requirements for the degree of Doctor of Philosophy

Baltimore, Maryland
April, 2000

Abstract

Constructing a mathematical representation of an object boundary (boundary mapping) from images is an important problem that is of importance to several active research areas such as image analysis, computer vision, and medical imaging. The focus of this dissertation is to investigate deformable models, a boundary mapping technique that incorporates both image information and prior knowledge about the boundary geometry to extract a meaningful boundary description. A key problem with methods reported in the literature is that they have difficulties in reliably mapping boundaries when the models are not initialized near target boundaries or are applied to reconstruct boundaries with concavities.

In this research, we make three main contributions to the area of boundary mapping. First, we developed a method called the gradient vector flow deformable model that is robust to both model initialization and boundary concavities. Second, we developed a generalization of the first method that allows for improved performance in converging to narrow boundary indentations and greater accuracy in localizing boundaries. Third, we developed a method for reconstructing the central layer of the human cerebral cortex from magnetic resonance images that uses our proposed deformable model as a core component. Our methods are validated on both simulated images and real magnetic resonance images.

This thesis is prepared under the direction of Dr. Jerry L. Prince.

Acknowledgements

I would like to thank my research advisor, Dr. Jerry L. Prince, for his friendship, encouragement, and guidance during the course of my research. He has been a valuable source of ideas and stimulating discussions on both technical and non-technical topics. It has been my great fortune and honor to earn my degree under his supervision. I would like to thank those who served as members of my Graduate Board Oral committee. Their time and energy is gratefully acknowledged. I would like to thank Dr. John Goutsias, Dr. Howard L. Weinert, and Dr. Lawrence B. Wolff for their supportive role throughout my graduate student career. I would like to thank both Dr. Michael I. Miller and Dr. Howard L. Weinert for their helpful comments and suggestions in helping this dissertation take its final form. Both the assistance of the faculty and staff and the financial support from the Department of Electrical and Computer Engineering throughout the years deserves much appreciation. The support of the National Science Foundation is gratefully acknowledged.

I would like to thank all of my colleagues and friends whose friendship and encouragement have made my experience at the Johns Hopkins University a memorable one. In particular, I would like to thank Dzung L. Pham for his helpful input and stimulating discussions regarding my research as well as his proofreading of my technical publications to improve their overall presentation quality. I would like to thank Maryam E. Etemad and Daphne N. Yu for their assistance in processing brain MR data for my research and proofreading several papers. I would like to thank Diego Socolinsky for pointing out the references to the solvability of the GVF Euler equation. I would like to thank Carol Prince who has prepared desserts for our weekly group meeting throughout the years, which is no doubt a great source of energy and support to my research. I would like to thank Dr. Nick Bryan, Dr. Christos Davatzikos, and Dr. Susan Resnick for having many helpful discussions on brain mapping and providing much needed data and expertise. I would like to thank Dr. Ron Kikinis at the Harvard Medical School for providing brain MR data used in this research.

Finally I would like to thank my parents Dechang Xu and Yongtuan Yang and my brother Chenguan Xu back home for all that they have done for me. I would especially like to thank my wife Wei Shu who with her patience, understanding, and love has helped me to achieve this goal. This dissertation is dedicated to them.

Contents

List of Figures

List of Tables

Chapter 1

Introduction

Over the last decade, there has been increasing research activity on deriving a mathematical description of object boundaries from images. This task, also known as *boundary mapping*, is a fundamental step for many active research areas in image analysis, computer vision, and medical imaging. Boundary mapping is aimed at helping us to augment our understanding of and to form conclusions about various properties of objects of interest in images. The applications of boundary mapping include image segmentation [45, 81, 100, 93, 125, 6], motion tracking [69, 107, 21, 76], shape modeling [106, 98, 76, 24], object recognition [24, 124, 49], and image registration and warping [30, 15, 109].

Mapping object boundaries from images is a difficult task due to the tremendous variability of object shapes and diverse image sources. For example, one important task in medical imaging is the boundary mapping of the brain cortex from 3-D magnetic resonance (MR) images (Fig. 1.1), where we are facing highly convoluted shape of brain cortex, imaging noise, sampling artifacts, and large-scale image data set. Imaging noise and sampling artifacts especially may cause the boundaries of objects of interest to be indistinct and disconnected. How to integrate these boundaries into a coherent and consistent mathematical description is a challenging problem that a boundary mapping technique has to address.

Boundary mapping methods abound in the literature of image analysis, computer vision, and medical imaging. Edge detection and linking, region growing, and

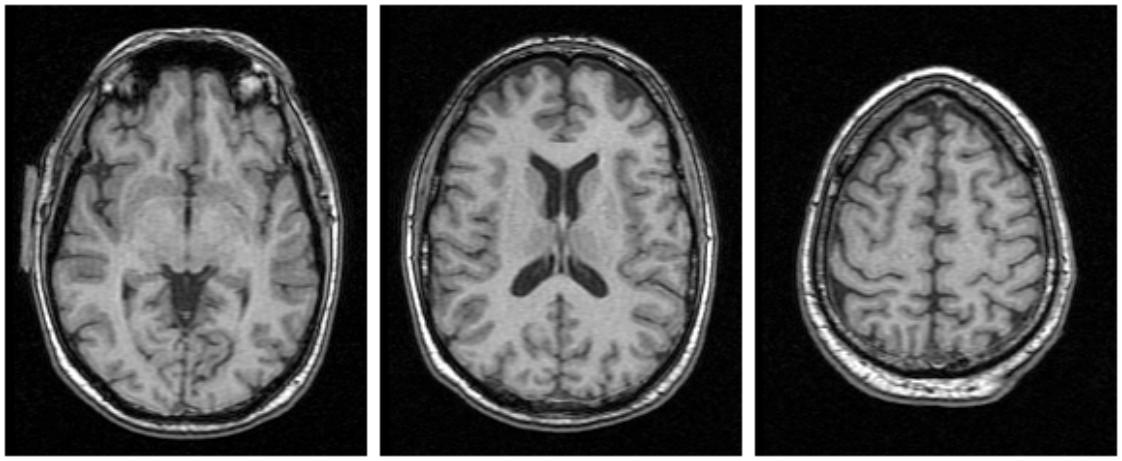

(a) (b) (c)

Figure 1.1: Sample image slices from acquired 3-D MRI data set

relaxation labeling are among the most widely used "classical" boundary mapping techniques. Edge detection and linking is a two step technique. First, an edge detector is applied to an image to identify boundary elements through detecting intensity discontinuities. Then, an edge linking algorithm is used to link the boundary elements together to obtain a parameterized curve or surface representation. Region growing is a region-based technique that usually starts with a set of "seed" points and from these grows regions by merging neighboring pixels or voxels that share similar properties. Relaxation labeling is a technique for segmenting objects through a class of locally cooperative and parallel processes based on the intensity difference among neighboring pixels or voxels. Further information about these classical boundary mapping methods can be found in most image analysis and computer vision textbooks (cf. [75, 56, 58, 47]).

One limitation of these classical methods is that they only consider local information, so that incorrect assumptions may be made during the boundary integration process causing generation of infeasible object boundaries. Furthermore, these methods usually generate results that are constrained by the resolution of the images and do not necessarily lead to accurate results. To address these problems, we have ex-

plored a boundary mapping technique called *deformable models* which is based on the work of Kass et al. [62]. Various names have been used to refer deformable models in the literature. In 2-D, deformable models are usually referred as snakes, active contours, balloons, and deformable contours. In 3-D, they are usually referred as active surfaces and deformable surfaces. In this thesis, we shall refer 2-D deformable models as deformable contours and 3-D deformable models as deformable surfaces.

1.1 Deformable Models

Deformable models are elastic curves or surfaces defined within an image domain that can move under the influence of internal forces coming from within the curve or surface itself and external forces computed from the image data. The internal and external forces are defined so that the deformable model will conform to an object boundary or other desired features within an image. Fig. 1.2 shows two examples of using both a deformable contour and a deformable surface to reconstruct anatomical boundaries from MR images. The results shown in this figure are obtained using the deformable models developed in this thesis.

Mathematically, deformable models are represented as parameterized manifolds (curves or surfaces) $\mathbf{x}(\mathbf{u})$, where $\mathbf{u}$ is the parameter of the manifold. The shape of the manifold is typically determined by a variational formulation whose general form is the following: find the $\mathbf{x}(\mathbf{u})$ that minimize the energy functional

$$\mathcal{E} = \mathcal{E}_{\text{int}} + \mathcal{E}_{\text{ext}} = \int_{\mathbf{U}} \mathbf{E}_{\text{int}}(\mathbf{x}(\mathbf{u})) + \mathbf{E}_{\text{ext}}(\mathbf{x}(\mathbf{u}))\, d\mathbf{u}. \tag{1.1}$$

This functional can be viewed as a representation of the energy of the manifold, and the final shape of the manifold corresponds to the minimum of this energy. The first term $\mathcal{E}_{\text{int}}$ prescribes *a priori* knowledge about the model such as its material properties (elasticity and rigidity). It can be used to characterize the deformation of a membrane or a thin-plate, for example. The second term $\mathcal{E}_{\text{ext}}$ is usually derived from image data and takes a minimum when the deformable model lies in the feature of interest such as object boundary. More discussion about deformable models is provided in Chapter 2.

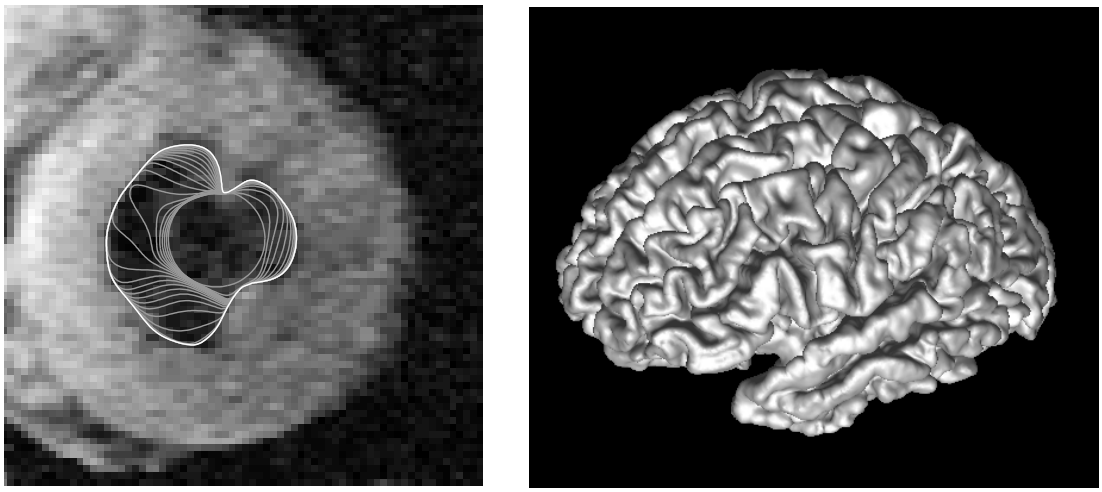

(a) (b)

Figure 1.2: (a) A 2-D example of using a deformable contour to extract the inner wall of the left ventricle of a human heart from an MR image. A sequence of deformable contours (plotted in a shade of gray) and the final converged result (plotted in white). (b) A 3-D example of using a deformable surface to reconstruct the brain cortical surface from a 3-D MR image.

1.2 Related Work

Although the name *deformable models* or *snakes* first appeared in work by Terzopoulos and his collaborators [105, 62, 106, 108], the ideas of deforming an elastic template date back much further to the work of Fischler and Elschlager's spring-loaded templates [43] (1973) and Widrow's rubber mask technique [114] (1973). However, the popularity of deformable models to date is mostly credited to the work of "Snakes" by Kass, Witkin, and Terzopoulos [62] (1987). Since the publication of "Snakes", deformable models have grown to be one of the most active research areas in the boundary mapping community. A complete review of deformable models is beyond the scope of this thesis. Instead, we refer the interested readers to a survey paper by McInerney and Terzopoulos [77]. Here, we shall only review work that is needed to understand the methods developed in this thesis.

There are basically two types of deformable models discussed in the literature: *parametric deformable models* (cf. [62, 5, 20, 76]) and *geometric deformable models*

(cf. [11, 73, 12, 113]). Geometric deformable models, based on the theory of curve evolution and geometric flows [96, 63, 64, 3], represents curves and surfaces implicitly as a level set of an evolving scalar function. Parametric deformable models, on the other hand, represents curves and surfaces explicitly in its parametric forms. In this thesis, we shall focus on parametric deformable models, although we expect our results to have applications in geometric deformable models as well.

Parametric deformable models synthesize parametric curves or surfaces within an image domain and allow them to move towards desired features, usually edges. Typically, the model is drawn toward the edges by *potential forces*, which are defined to be the negative gradient of a potential function. Additional forces, such as pressure forces [20], together with the potential forces comprise the external forces. There are also internal forces designed to hold the model together (elasticity forces) and to keep it from bending excessively (bending forces).

There are two key difficulties with parametric deformable models. First, the initial model must, in general, be close to the true boundary or else it will likely converge to the wrong result. Several methods have been proposed to address this problem including multiresolution methods [68], pressure forces [20], and distance potentials [21]. The basic idea is to increase the capture range of the external force fields and to guide the model toward the desired boundary. The second problem is that deformable models have difficulties progressing into boundary concavities [33, 1]. Although pressure forces [20], control points [33], domain-adaptivity [32], directional attractions [1], and the use of solenoidal fields [90] have been proposed, these methods solve only one problem or both problems but with the price of creating new difficulties. For example, multiresolution methods have addressed the issue of capture range, but specifying how the deformable model should move across different resolutions remains problematic. Another example is that of pressure forces, which can push a deformable model into boundary concavities, but cannot be too strong or "weak" edges will be overwhelmed [103]. Pressure forces must also be initialized to push out or push in, a condition that mandates careful initialization.

One of the contributions of this thesis is the development of two new classes of external force fields derived from generalized vector diffusion equations that address

both problems listed above.

1.3 Brain Cortex Reconstruction

Our research on deformable models was motivated by one of the most interesting and challenging problems in computational neuroanatomy: human cerebral cortex reconstruction from MR images. This research is an important and fundamental step in both image-guided neurosurgery [50, 110] and human brain mapping such as brain geometry analysis [48, 59, 42, 91], functional mapping [27, 104, 41], spatial normalization of brain images [102, 10, 29], and brain image registration [16, 22, 17, 30, 15]. Furthermore, extracted cortical surfaces can be used to study the morphological variability of the brain in aging and among different populations.

Geometrically, the human cerebral cortex is a thin folded sheet of gray matter (GM) that lies inside the cerebrospinal fluid (CSF) and outside the white matter (WM) of the brain, as shown in Fig. 1.3. Reconstruction of the cortex from MR images is problematic, however, due to difficulties such as imaging noise, partial volume averaging, image intensity inhomogeneities, convoluted cortical structures, and the requirement to preserve anatomical topology. Preservation of topology is important for morphometric analysis, surgical path planning, and functional mapping where a representation consistent with anatomical structure is required.

Recently, there has been a considerable amount of work in this area of research. Mangin et al. [74] and Teo et al. [104] reconstructed the cortex using a voxel-based method. Volumetric registration proposed by Collins et al. [22] and Christensen et al. [15] allows the generation of cortical surfaces from MR brain image volumes given a template volume and its associated reconstructed cortical surface. Methods of tracing 2-D contours either manually or automatically through 2-D image slices followed by contour tiling to reconstruct the cortical surface have been described by Drury et al. [42] and Klein et al. [65]. Dale & Sereno [27], MacDonald et al. [72], Davatzikos & Bryan [31], and Sandor & Leahy [95] have used methods based on deformable surface models to reconstruct cortical surfaces. The deformable surface model is a suitable tool for cortical surface reconstruction due to its ability to deform

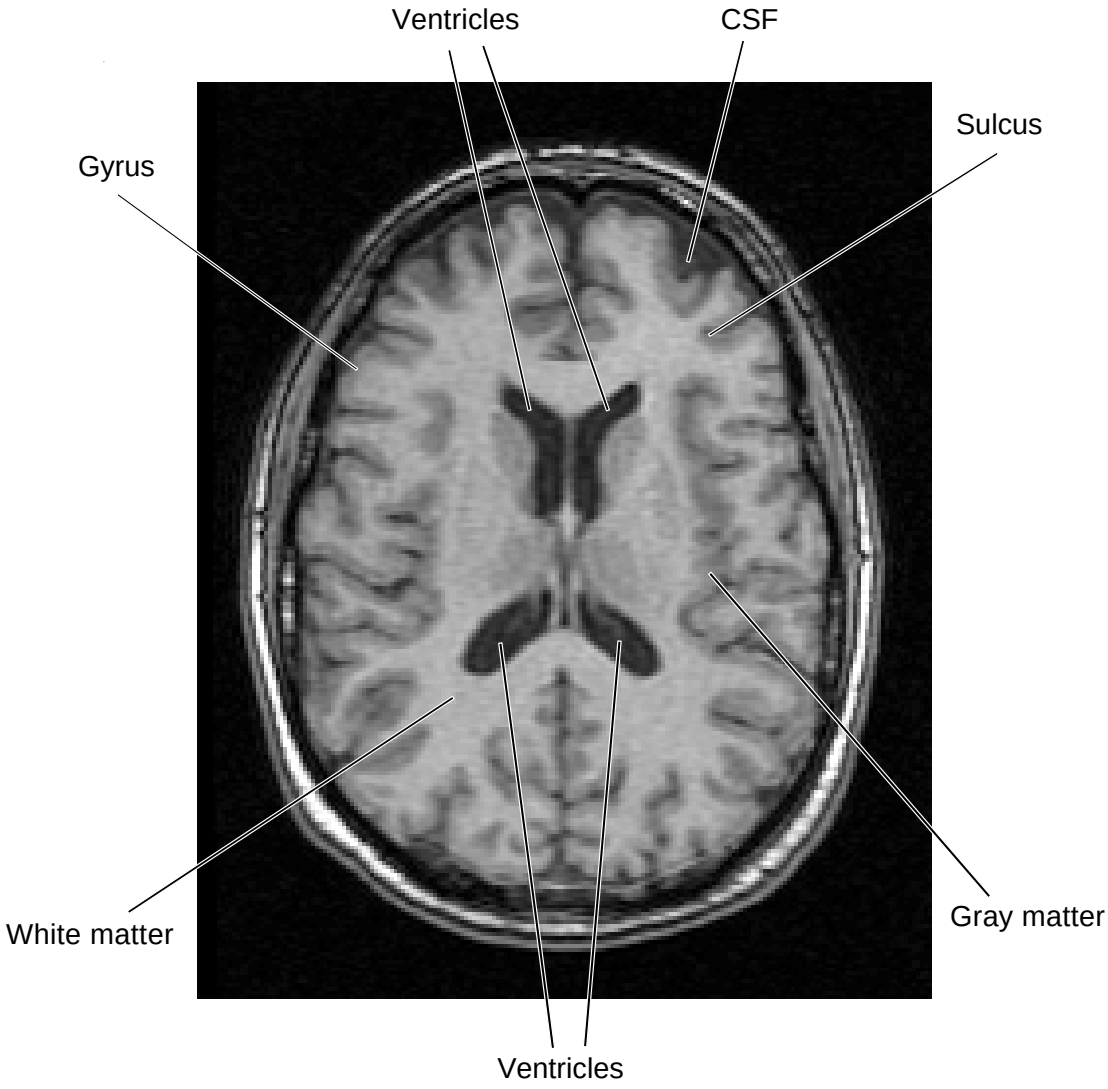

Figure 1.3: A transaxial MR image of the human brain.

through a continuum and yield a continuous, smooth surface representation of the cortex. Traditional deformable surface models, however, have difficulties progressing into convoluted regions resulting in reconstructed surfaces that lack the deep cortical folds [74, 31, 95, 72].

In this thesis, we developed a systematic method for obtaining a parametric surface representation of the central layer of the human cerebral cortex that addresses the above difficulties.

1.4 Thesis Contributions

Three main contributions are made in this thesis:

1. **Gradient vector flow**: A new deformable model formulation for boundary mapping is developed. This new model uses a new type of external force called *gradient vector flow* (GVF). The GVF external force has three advantages compared to traditional external forces. First, it has a large capture range and allows deformable models to be initialized far away from the object boundary. Second, it can attract deformable models to move into boundary concavities where conventional methods have difficulties. Third, the GVF formulation is applicable to any dimension allowing it to be applied in a wide range of applications. This method is applied to both simulated images and real MR images.

2. **Generalized gradient vector flow**: Based on the GVF formulation, a generalization is developed to generate a family of vector fields that share similar properties as those of the GVF vector field. This generalization, called generalized gradient vector flow (GGVF), allows selection of external forces that are superior to the GVF external forces for certain applications. An important property called GGVF medialness, which results in an effective method for reconstructing the central layer of thick boundaries, is introduced and analyzed. We validate this method with both simulated and real MR images.

3. **Brain cortex reconstruction**: A new method based on the GGVF deformable surfaces for reconstructing the human brain cortex is developed. Important ad-

vantages of this method over existing methods are that it reconstructs the entire cortical surface including deep convoluted folds and that the reconstructed cortical surface maintains the correct anatomical topology. This method is validated on both phantom and real MR brain images. Next, a method for computing differential geometry quantities on the reconstructed cortical surface and a preliminary method for estimating the cortex thickness is developed. Finally, a method that transforms the reconstructed cortical surface to a spherical map is presented.

1.5 Previous Publications

Portions of this thesis have been previously published. The gradient vector flow algorithm was published in [121, 123]. The generalized gradient vector flow algorithm was published in [120, 122]. The brain cortex reconstruction method was published in [118, 117, 119] and a journal version of this reconstruction technique has been submitted as well [116]. The spherical mapping method was published in [115].

1.6 Thesis Organization

This thesis is organized as follows. In Chapter 2, we provide background materials about deformable models. In Chapter 3, we develop the GVF deformable model. In Chapter 4, we develop the GGVF deformable model, and study the medialness property of GGVF vector field as well as the problem of central layer reconstruction of thick boundaries. In Chapter 5, we develop the brain cortex reconstruction method as well as methods for computing differential geometry quantities and mapping the cortical surface to a sphere. Details of implementing deformable models and computing differential geometry quantities can be found in thesis Appendices A and B. Finally, we conclude the thesis in Chapter 6 with a summary and a discussion of future research areas.

Chapter 2

Background

In this chapter, we provide a brief overview of traditional deformable contours and surfaces. For each model, we start by introducing its variational formulation. We then describe the commonly used external energy. Finally, we provide the solution to the variational formulation known as the Euler equation. Details of discrete implementation are deferred to the end of this dissertation (Appendix A). A more comprehensive treatment of deformable models can be found in [62, 21, 76].

2.1 Deformable Contours

A traditional deformable contour is a curve $\mathbf{x}(s) = [x(s), y(s)]$, $s \in [0, 1]$, that moves through the spatial domain of an image to minimize the energy functional

$$E = \int_0^1 \frac{1}{2}(\alpha|\mathbf{x}'(s)|^2 + \beta|\mathbf{x}''(s)|^2) + E_{\text{ext}}(\mathbf{x}(s))ds \tag{2.1}$$

where α and β are weighting parameters that control the contour's tension and rigidity, respectively, and $\mathbf{x}'(s)$ and $\mathbf{x}''(s)$ denote the first and second derivatives of $\mathbf{x}(s)$ with respect to s. The external energy E_{ext} is a function derived from the image so that it takes on its smaller values at the features of interest, such as boundaries. Given a gray-level image $I(x, y)$, viewed as a function of continuous position variables (x, y), typical external energies designed to lead a deformable contour toward step

edges are [62]:

$$E_{\text{ext}}^{(1)}(x,y) = -|\nabla I(x,y))|^2 \tag{2.2}$$

$$E_{\text{ext}}^{(2)}(x,y) = -|\nabla(G_\sigma(x,y) * I(x,y))|^2 \tag{2.3}$$

where $G_\sigma(x,y)$ is a two-dimensional Gaussian function with standard deviation σ and ∇ is the gradient operator. If the image is a line drawing (black on white), then appropriate external energies include [20]:

$$E_{\text{ext}}^{(3)}(x,y) = I(x,y) \tag{2.4}$$

$$E_{\text{ext}}^{(4)}(x,y) = G_\sigma(x,y) * I(x,y) \tag{2.5}$$

It is easy to see from these definitions that larger σ's will cause the boundaries to become blurry. Such large σ's are often necessary, however, in order to increase the capture range[1] of the deformable contour.

The problem of finding a parameterized curve $\mathbf{x}(s)$ that minimizes E is known as the variational problem [25]. It has be shown that the curve $\mathbf{x}(s)$ that minimizes E must satisfy the following Euler equation [62, 20]

$$\alpha\mathbf{x}''(s) - \beta\mathbf{x}''''(s) - \nabla E_{\text{ext}} = 0 \tag{2.6}$$

Various choices of boundary conditions for $\mathbf{x}(s)$ may be used, we use periodic boundary condition $\mathbf{x}(0) = \mathbf{x}(1)$ since we deal only with closed contours.

To gain some insight about the physical behaviour of deformable contours, we can view Eq. (2.6) as a force balance equation

$$\mathbf{F}_{\text{int}} + \mathbf{F}_{\text{ext}}^{(\text{p})} = 0 \tag{2.7}$$

where $\mathbf{F}_{\text{int}} = \alpha\mathbf{x}''(s) - \beta\mathbf{x}''''(s)$ and $\mathbf{F}_{\text{ext}}^{(\text{p})} = -\nabla E_{\text{ext}}$. The internal force $\mathbf{F}_{\text{int}}$ discourages stretching and bending while the external potential force $\mathbf{F}_{\text{ext}}^{(\text{p})}$ pulls the contour towards the desired image edges.

Euler equation (2.6) provides the necessary condition for any curve that minimize the energy functional E. In general, however, since the energy functional E is non-convex, the Euler equation has many solutions that correspond to the local minimum

[1] Capture range is a region where a deformable contour can be initialized while still finding the desired boundary under the guidance of external forces.

of E [20, 19]. Although a global minimum can be found using several existing global optimization techniques such as graduated non-convexity algorithms [8] and genetic algorithms [34, 66], they are generally much more computational intensive than local minimization techniques such as gradient descent methods. In this work, we will use gradient descent methods to find the minimum. One of the consequence of using gradient descent methods is that a good initialization is required to obtain a satisfactory solution. This issue will be discussed in detail later in this thesis, and methods to address this issue will be proposed as well. We note that the solution to the Euler equation is assured to be a smooth curve that is at least twice-differentiable, as long as either α or β is non-zero. Details on the mathematic properties of deformable models can be found in [19].

To find a solution to (2.6), the deformable contour is made dynamic by treating $\mathbf{x}$ as function of time t as well as s — i.e., $\mathbf{x}(s,t)$. We note that adding a time directive term of $\mathbf{x}$ is equivalent to applying gradient descent algorithm to find the local minimum of Eq. (2.1) [19]. Then, the partial derivative of $\mathbf{x}$ with respect to t is then set equal to the left hand side of (2.6) as follows

$$\mathbf{x}_t(s,t) = \alpha\mathbf{x}''(s,t) - \beta\mathbf{x}''''(s,t) - \nabla E_{\text{ext}} \tag{2.8}$$

When the solution $\mathbf{x}(s,t)$ stabilizes, the term $\mathbf{x}_t(s,t)$ vanishes and we achieve a solution of (2.6). A numerical solution to (2.8) can be found by discretizing the equation and solving the discrete system iteratively (cf. [62]). Details are provided in Appendix A.1. We note that most deformable contour implementations use either a parameter that multiplies $\mathbf{x}_t$ in order to control the temporal step-size, or a parameter that multiplies ∇E_{ext}, which permits separate control of the external force strength. In this thesis, we normalize the external forces so that the maximum magnitude is equal to one, and use a unit temporal step-size for all the experiments.

2.2 Deformable Surfaces

A traditional deformable surface is a surface $\mathbf{x}(\mathbf{u}) = [x(\mathbf{u}), y(\mathbf{u}), z(\mathbf{u})]$, $\mathbf{u} = (u^1, u^2) \in [0,1] \times [0,1]$, that moves through the spatial domain of a 3-D image to

minimize an energy functional [21, 77]. A typical example of such an energy functional is

$$E = \int \frac{1}{2}(\alpha \sum_{i=1}^{2} |\mathbf{x}_i|^2 + \beta \sum_{i,j=1}^{2} |\mathbf{x}_{ij}|^2) + E_{\text{ext}}(\mathbf{x}) d\mathbf{u} \tag{2.9}$$

where α and β are weighting parameters that control the surface's tension and rigidity, $\mathbf{x}_i$ and $\mathbf{x}_{ij}$ denote the first and second partial derivatives of $\mathbf{x}$ with respect to u^i, and $E_{\text{ext}}(\mathbf{x})$ is the external energy function derived from the image that can be defined similarly as that of deformable contours. It can also be shown that the deformable surface minimizing the above energy functional can be obtained by finding the steady state solution of the following dynamic equation:

$$\mathbf{x}_t = \mathbf{F}_{\text{int}} + \mathbf{F}_{\text{ext}} \tag{2.10}$$

where the internal forces are given by $\mathbf{F}_{\text{int}} = \alpha \nabla^2_{\mathbf{u}} \mathbf{x} - \beta \nabla^2_{\mathbf{u}} (\nabla^2_{\mathbf{u}} \mathbf{x})$ and the external forces are $\mathbf{F}_{\text{ext}} = -\nabla E_{\text{ext}}(\mathbf{x})$. The symbol $\nabla^2_{\mathbf{u}} = \frac{\partial^2}{(\partial u^1)^2} + \frac{\partial^2}{(\partial u^2)^2}$ is the Laplacian operator. Note that in Eq. (2.10) an auxiliary variable time t is introduced to make deformable surface $\mathbf{x}$ dynamic. A detailed discussion of implementation of deformable surfaces is provided in Appendix A.2.

The comments made in Section 2.1 about the global versus local nature of the solution of the deformable contours also applies to deformable surfaces.

Chapter 3

Gradient Vector Flow Deformable Models

It is known that traditional deformable models have problems associated with initialization and poor convergence to boundary concavities [83, 33, 1]. In this chapter, we present a new class of external forces for deformable models that addresses both problems listed above. These fields, which we call *gradient vector flow* (GVF) fields, are dense vector fields derived from images by minimizing a certain energy functional in a variational framework. The minimization is achieved by solving a pair of decoupled linear partial differential equations which diffuses the gradient vectors of a gray-level or binary edge map computed from the image. We call the deformable models that uses the GVF field as its external force a *GVF deformable model*. The GVF deformable model is distinguished from nearly all previous deformable formulations in that its external forces cannot be written as the negative gradient of a potential function. Because of this, it cannot be formulated using the standard energy minimization framework; instead, it is specified directly from a force balance condition.

GVF can be defined in any dimension; however, in this chapter, we focus our attention on two-dimensional problems for convenience. We shall refer 2-D deformable models as deformable contours and those that use GVF as their external forces *GVF deformable contours*. We note that all the discussions on GVF deformable contours

are valid to GVF deformable models in general. Accordingly, we show several 2-D examples and one 3-D example at the end of the chapter.

Particular advantages of a GVF deformable contour over a traditional deformable contour are its insensitivity to initialization and its ability to move into boundary concavities. As we show in this chapter, its initializations can be inside, outside, or across the object's boundary. Unlike the balloon model, the GVF deformable contour does not need prior knowledge about whether to shrink or expand towards the boundary. The GVF deformable contour also has a large capture range, which means that, barring interference from other objects, it can be initialized far away from the boundary. This increased capture range is achieved through a diffusion process that does not blur the edges themselves, so multiresolution methods are not needed. The external force model that is closest in spirit to GVF is the distance potential forces of Cohen and Cohen [21]. Like GVF, these forces originate from an edge map of the image and can provide a large capture range. We show, however, that unlike GVF, distance potential forces cannot move a deformable contour into boundary concavities. We believe that this is a property of all conservative forces which characterize nearly all deformable contour external forces, and that exploring non-conservative external forces, such as GVF, is an important direction for future research in deformable contour models.

3.1 Behavior of Traditional Deformable Contours

An example of the behavior of a traditional deformable contour is shown in Fig. 3.1. Fig. 3.1a shows a 64×64-pixel line-drawing of a U-shaped object (shown in gray) having a boundary concavity at the top. It also shows a sequence of curves (in black) depicting the iterative progression of a traditional deformable contour ($\alpha = 0.6$, $\beta = 0.0$) initialized outside the object but within the capture range of the potential force field. The potential force field $\mathbf{F}_{\text{ext}}^{(\text{p})} = -\nabla E_{\text{ext}}^{(4)}$ (defined in Eq. (2.5)) where $\sigma = 1.0$ pixel is shown in Fig. 3.1b. We note that the final solution in Fig. 3.1a solves the Euler equations of the deformable contour formulation, but remains split across the concave region.

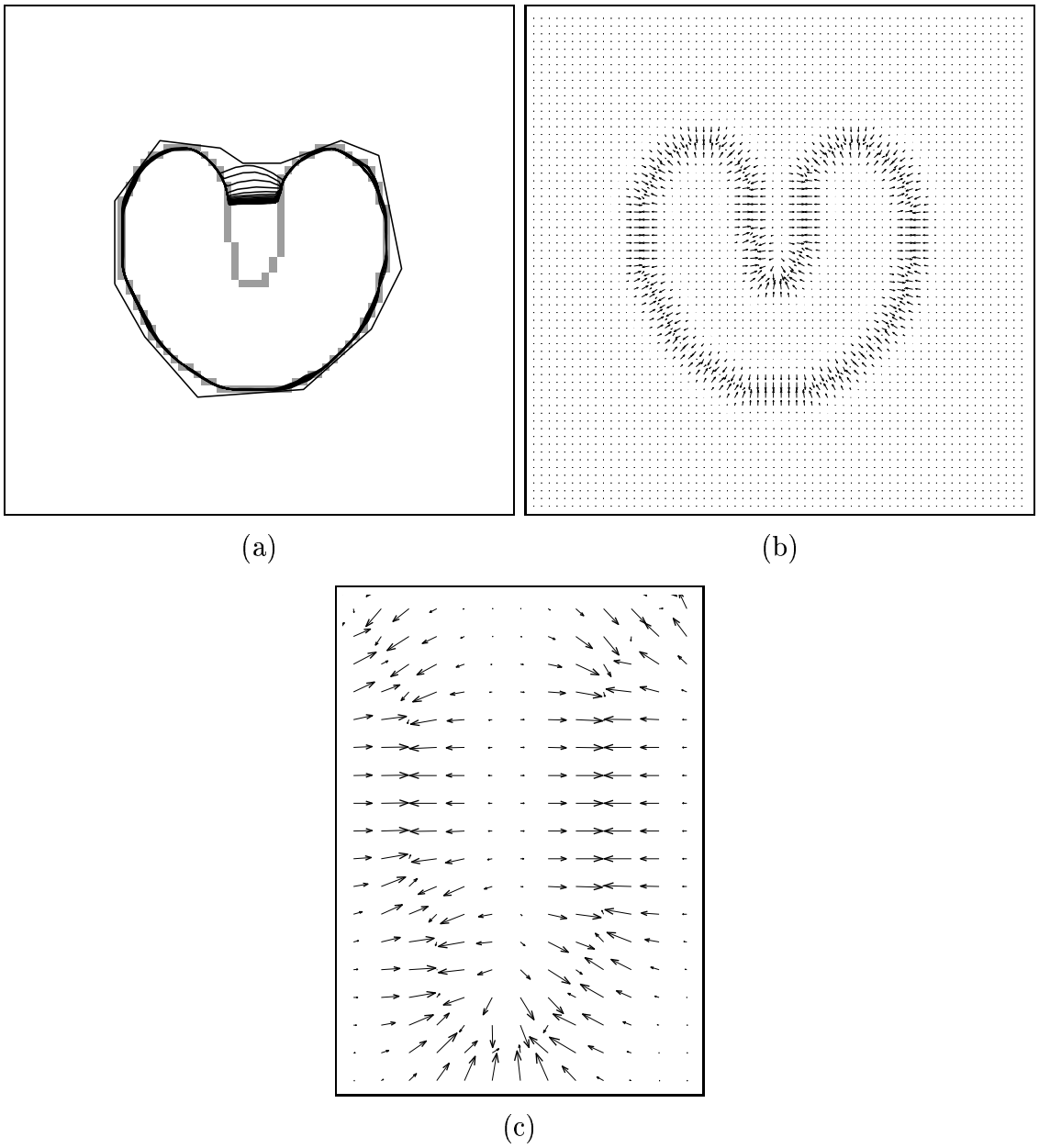

Figure 3.1: (a) The convergence of a deformable contour using (b) traditional potential forces, (c) shown close-up within the boundary concavity.

The reason for the poor convergence of this deformable contour is revealed in Fig. 3.1c, where a close-up of the external force field within the boundary concavity is shown. Although the external forces correctly point toward the object boundary, within the boundary concavity the forces point horizontally *in opposite directions*. Therefore, the deformable contour is pulled apart toward each of the "fingers" of the U-shape, but not made to progress downward into the concavity. There is no choice of α and β that will correct this problem.

Another key problem with traditional deformable contour formulations, the problem of limited capture range, can be understood by examining Fig. 3.1b. In this figure, we see that the magnitude of the external forces die out quite rapidly away from the object boundary. Increasing σ in (2.5) will increase this range, but the boundary localization will become less accurate and distinct, ultimately obliterating the concavity itself when σ becomes too large.

Cohen and Cohen [21] proposed an external force model that significantly increases the capture range of a traditional deformable contour. These external forces are the negative gradient of a potential function that is computed using a Euclidean (or chamfer) distance map. We refer to these forces as *distance potential forces* to distinguish them from the traditional potential forces defined in Section 2.1. Fig. 3.2 shows the performance of a deformable contour using distance potential forces. Fig. 3.2a shows both the U-shaped object (in gray) and a sequence of contours (in black) depicting the progression of the deformable contour from its initialization far from the object to its final configuration. The distance potential forces shown in Fig. 3.2b have vectors with large magnitudes far away from the object, explaining why the capture range is large for this external force model.

As shown in Fig. 3.2a, this deformable contour also fails to converge to the boundary concavity. This can be explained by inspecting the magnified portion of the distance potential forces shown in Fig. 3.2c. We see that, like traditional potential forces, these forces also point horizontally in opposite directions, which pulls the deformable contour apart but not downward into the boundary concavity. We note that Cohen and Cohen's modification to the basic distance potential forces, which applies a nonlinear transformation to the distance map [21], does not change the direction of the

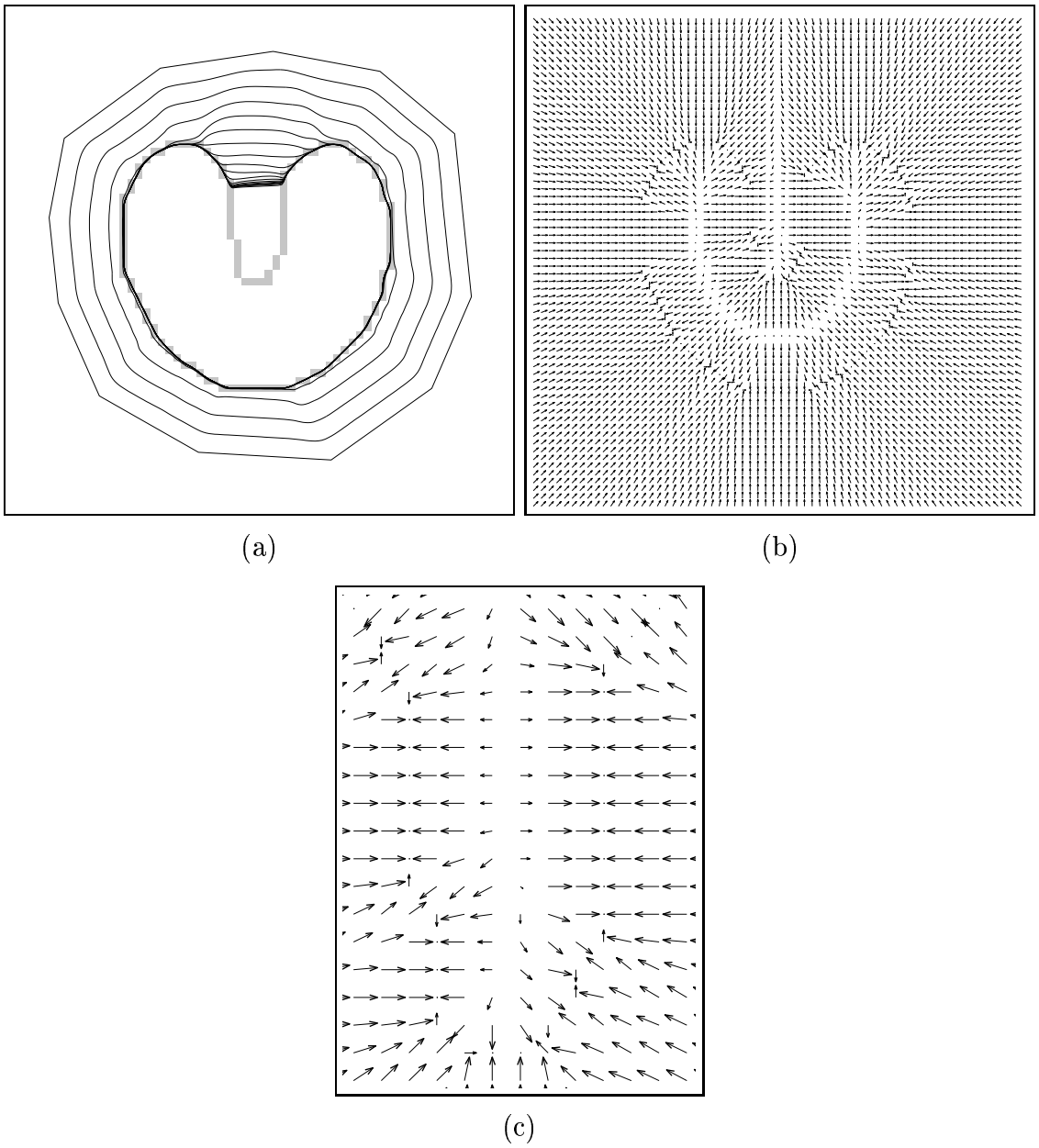

Figure 3.2: (a) The convergence of a deformable contour using (b) distance potential forces, (c) shown close-up within the boundary concavity.

forces, only their magnitudes. Therefore, the problem of convergence to boundary concavities is not solved by distance potential forces.

3.2 Generalized Force Balance Equations

The deformable contour solutions shown in Figs. 3.1a and 3.2a both satisfy the Euler equations (2.6) for their respective energy model. Accordingly, the poor final configurations can be attributed to convergence to a local minimum of the objective function (2.1). Several researchers have sought solutions to this problem by formulating deformable contours directly from a force balance equation in which the standard external force $\mathbf{F}_{\text{ext}}^{(\text{p})}$ is replaced by a more general external force $\mathbf{F}_{\text{ext}}^{(\text{g})}$ as follows

$$\mathbf{F}_{\text{int}} + \mathbf{F}_{\text{ext}}^{(\text{g})} = 0 \tag{3.1}$$

The choice of $\mathbf{F}_{\text{ext}}^{(\text{g})}$ can have a profound impact on both the implementation and the behavior of a deformable contour. Broadly speaking, the external forces $\mathbf{F}_{\text{ext}}^{(\text{g})}$ can be divided into two classes: static and dynamic. Static forces are those that are computed from the image data, and do not change as the deformable contour progresses. Standard deformable contour potential forces are static external forces. Dynamic forces are those that change as the deformable contour deforms.

Several types of dynamic external forces have been invented to try to improve upon the standard deformable contour potential forces. For example, the forces used in multiresolution deformable contours [68] and the pressure forces used in balloons [20] are dynamic external forces. The use of multiresolution schemes and pressure forces, however, adds complexity to a deformable contour's implementation and unpredictability to its performance. For example, pressure forces must be initialized to either push out or push in, and may overwhelm weak boundaries if they act too strongly [103]. Conversely, they may not move into boundary concavities if they are pushing in the wrong direction or act too weakly.

In this chapter, we present a new type of *static external force*, one that does not change with time or depend on the position of the deformable contour itself. The underlying mathematical premise for this new force comes from the Helmholtz theorem

(cf. [80]), which states that the most general static vector field can be decomposed into two components: an irrotational (curl-free) component and a solenoidal (divergence-free) component.[2] An external potential force generated from the variational formulation of a traditional deformable contour must enter the force balance equation (2.6) as a static irrotational field, since it is the gradient of a potential function. Therefore, a more general static field $\mathbf{F}_{\text{ext}}^{(\text{g})}$ can be obtained by allowing the possibility that it comprises *both* an irrotational component and a solenoidal component. Our previous paper [90] explored the idea of constructing a separate solenoidal field from an image, which was then added to a standard irrotational field. In the following section, we pursue a more natural approach in which the external force field is designed to have the desired properties of both a large capture range and the presence of forces that point into boundary concavities. The resulting formulation produces external force fields that can be expected to have both irrotational and solenoidal components.

3.3 Gradient Vector Flow Deformable Contour

Our overall approach is to use the force balance condition (2.7) as a starting point for designing a deformable contour. We define below a new static external force field $\mathbf{F}_{\text{ext}}^{(\text{g})} = \mathbf{v}(x, y)$, which we call the *gradient vector flow* (GVF) field. To obtain the corresponding dynamic deformable contour equation, we replace the potential force $-\nabla E_{\text{ext}}$ in (2.8) with $\mathbf{v}(x, y)$, yielding

$$\mathbf{x}_t(s,t) = \alpha \mathbf{x}''(s,t) - \beta \mathbf{x}''''(s,t) + \mathbf{v} \tag{3.2}$$

We call the parametric curve solving the above dynamic equation a *GVF deformable contour*. It is solved numerically by discretization and iteration, in identical fashion to the traditional deformable contour.

Although the final configuration of a GVF deformable contour will satisfy the force-balance equation (2.7), this equation does not, in general, represent the Euler equations of the energy minimization problem in (2.1). This is because $\mathbf{v}(x, y)$ will

[2]Irrotational fields are sometimes called conservative fields; they can be represented as the gradient of a scalar potential function.

not, in general, be an irrotational field. The loss of this optimality property, however, is well-compensated by the significantly improved performance of the GVF deformable contour.

3.3.1 Edge Map

To define the GVF field, we begin by defining an *edge map* $f(x, y)$ derived from the image $I(x, y)$ having the property that it is larger near the image edges.[3] We can use any gray-level or binary edge map defined in the image processing literature (cf. [58]); for example, we could use

$$f(x, y) = -E_{\text{ext}}^{(i)}(x, y) \tag{3.3}$$

where $E_{\text{ext}}^{(i)}(x, y)$, $i = 1, 2, 3,$ or 4, is the external energy defined in Eq. (2.0) and Eq. (2.0). Three general properties of edge maps are important in the present context. First, the gradient of an edge map ∇f has vectors pointing toward the edges, which are normal to the edges at the edges. Second, these vectors generally have large magnitudes only in the immediate vicinity of the edges. Third, in homogeneous regions, where $I(x, y)$ is nearly constant, ∇f is nearly zero.

Now consider how these properties affect the behavior of a traditional deformable contour when the gradient of an edge map is used as an external force. Because of the first property, a deformable contour initialized close to the edge will converge to a stable configuration near the edge. This is a highly desirable property. Because of the second property, however, the capture range will be very small, in general. Because of the third property, homogeneous regions will have no external forces whatsoever. These last two properties are undesirable. Our approach is to keep the highly desirable property of the gradients near the edges, but to extend the gradient map farther away from the edges and into homogeneous regions using a computational diffusion process. As an important benefit, the inherent competition of the diffusion process will also create vectors that point into boundary concavities.

[3] Other features can be sought by redefining $f(x, y)$ to be larger at the desired features.

3.3.2 Gradient Vector Flow

We define the gradient vector flow to be the vector field $\mathbf{v}(x,y) = [u(x,y), v(x,y)]$ that minimizes the energy functional

$$\mathcal{E} = \iint \mu({u_x}^2 + {u_y}^2 + {v_x}^2 + {v_y}^2) + |\nabla f|^2 |\mathbf{v} - \nabla f|^2 dxdy \tag{3.4}$$

This variational formulation follows a standard principle, that of making the result smooth when there is no data. In particular, we see that when $|\nabla f|$ is small, the energy is dominated by sum of the squares of the partial derivatives of the vector field, yielding a slowly-varying field. On the other hand, when $|\nabla f|$ is large, the second term dominates the integrand, and is minimized by setting $\mathbf{v} = \nabla f$. This produces the desired effect of keeping $\mathbf{v}$ nearly equal to the gradient of the edge map when it is large, but forcing the field to be slowly-varying in homogeneous regions. The parameter μ is a regularization parameter governing the tradeoff between the first term and the second term in the integrand. This parameter should be set according to the amount of noise present in the image (more noise, increase μ).

We note that the smoothing term — the first term within the integrand of (3.4) — is the same term used by Horn and Schunck in their classical formulation of optical flow [57]. It has recently been shown that this term corresponds to an equal penalty on the divergence and curl of the vector field [51]. Therefore, the vector field resulting from this minimization can be expected to be neither entirely irrotational nor entirely solenoidal.

Using the *calculus of variations* [25], it can be shown that the GVF field can be found by solving the following Euler equations

$$\mu\nabla^2 u - (u - f_x)({f_x}^2 + {f_y}^2) = 0 \tag{3.5a}$$

$$\mu\nabla^2 v - (v - f_y)({f_x}^2 + {f_y}^2) = 0 \tag{3.5b}$$

where ∇^2 is the Laplacian operator. These equations provide further intuition behind the GVF formulation. We note that in a homogeneous region (where $I(x,y)$ is constant), the second term in each equation is zero because the gradient of $f(x,y)$ is zero. Therefore, within such a region, u and v are each determined by Laplace's

equation, and the resulting GVF field is interpolated from the region's boundary, reflecting a kind of competition among the boundary vectors. This explains why GVF yields vectors that point into boundary concavities.

3.3.3 Numerical Implementation

Equations (3.5a) and (3.5b) can be solved by treating u and v as functions of time and solving

$$u_t(x,y,t) = \mu\nabla^2 u(x,y,t) - (u(x,y,t) - f_x(x,y))(f_x(x,y)^2 + f_y(x,y)^2) \tag{3.6a}$$

$$v_t(x,y,t) = \mu\nabla^2 v(x,y,t) - (v(x,y,t) - f_y(x,y))(f_x(x,y)^2 + f_y(x,y)^2) \tag{3.6b}$$

The steady-state solution of these linear parabolic equations is the desired solution of the Euler equations (3.5a) and (3.5b). Note that these equations are decoupled, and therefore can be solved as separate scalar partial differential equations in u and v. The equations in (3.6) are known as *generalized diffusion equations*, and are known to arise in such diverse fields as heat conduction, reactor physics, and fluid flow [14]. Here, they have appeared from our description of desirable properties of deformable contour external force fields as represented in the energy functional of (3.4).

For convenience, we rewrite Equation (3.6) as follows

$$u_t(x,y,t) = \mu\nabla^2 u(x,y,t) - b(x,y)u(x,y,t) + c^1(x,y) \tag{3.7a}$$

$$v_t(x,y,t) = \mu\nabla^2 v(x,y,t) - b(x,y)v(x,y,t) + c^2(x,y) \tag{3.7b}$$

where

$$\begin{aligned} b(x,y) &= f_x(x,y)^2 + f_y(x,y)^2 \\ c^1(x,y) &= b(x,y)f_x(x,y) \\ c^2(x,y) &= b(x,y)f_y(x,y) \end{aligned}$$

Any digital image gradient operator (cf. [58]) can be used to calculate f_x and f_y. In the examples shown in this paper, we use simple central differences. The coefficients $b(x,y)$, $c^1(x,y)$, and $c^2(x,y)$, can then be computed and fixed for the entire iterative process.

To set up the iterative solution, let the indices i, j, and n correspond to x, y, and t, respectively, and let the spacing between pixels be Δx and Δy and the time step for each iteration be Δt. Then the required partial derivatives can be approximated as

$$\begin{aligned}
u_t &= \frac{1}{\Delta t}(u_{i,j}^{n+1} - u_{i,j}^{n}) \\
v_t &= \frac{1}{\Delta t}(v_{i,j}^{n+1} - v_{i,j}^{n}) \\
\nabla^2 u &= \frac{1}{\Delta x \Delta y}(u_{i+1,j} + u_{i,j+1} + u_{i-1,j} + u_{i,j-1} - 4u_{i,j}) \\
\nabla^2 v &= \frac{1}{\Delta x \Delta y}(v_{i+1,j} + v_{i,j+1} + v_{i-1,j} + v_{i,j-1} - 4v_{i,j})
\end{aligned}$$

Substituting these approximations into (3.7) gives our iterative solution to GVF:

$$\begin{aligned}
u_{i,j}^{n+1} &= (1 - b_{i,j}\Delta t)u_{i,j}^{n} + \\
&\quad r(u_{i+1,j}^{n} + u_{i,j+1}^{n} + u_{i-1,j}^{n} + u_{i,j-1}^{n} - 4u_{i,j}^{n}) + c_{i,j}^{1}\Delta t \qquad (3.8a) \\
v_{i,j}^{n+1} &= (1 - b_{i,j}\Delta t)v_{i,j}^{n} + \\
&\quad r(v_{i+1,j}^{n} + v_{i,j+1}^{n} + v_{i-1,j}^{n} + v_{i,j-1}^{n} - 4v_{i,j}^{n}) + c_{i,j}^{2}\Delta t \qquad (3.8b)
\end{aligned}$$

where

$$r = \frac{\mu \Delta t}{\Delta x \Delta y} \qquad (3.9)$$

Convergence of the above iterative process is guaranteed by a standard result in the theory of numerical methods (cf. [4]). Provided that b, c^1, and c^2 are bounded, (3.8) is stable whenever the Courant-Friedrichs-Lewy step-size restriction $r \leq 1/4$ is maintained. Since normally Δx, Δy, and μ are fixed, using the definition of r in (3.9) we find that the following restriction on the time-step Δt must be maintained in order to guarantee convergence of GVF:

$$\Delta t \leq \frac{\Delta x \Delta y}{4\mu} \qquad (3.10)$$

The intuition behind this condition is revealing. First, convergence can be made to be faster on coarser images — i.e., when Δx and Δy are larger. Second, when μ is large and the GVF is expected to be a smoother field, the convergence rate will be slower (since Δt must be kept small).

Our 2-D GVF computations were implemented using MATLAB [4] code. For an $N = 256 \times 256$-pixel image on an SGI Indigo-2, typical computation times are 8 seconds for the traditional potential forces (written in C), 155 seconds for the distance potential forces (Euclidean distance map, written in MATLAB), and 420 seconds for the GVF forces (written in MATLAB, using $\sqrt{N}$ iterations). The computation time of GVF can be substantially reduced by using optimized code in C or FORTRAN. For example, we have implemented 3-D GVF (see Section 5.2) in C, and computed GVF with 150 iterations on a $256 \times 256 \times 60$-voxel image in 31 minutes. Accounting for the size difference and extra dimension, we conclude that written in C, GVF computation for a 2-D 256×256-pixel image would take approximately 53 seconds. Algorithm optimization such as use of the multigrid method should yield further improvements.

3.4 GVF Fields and Deformable Contours: Demonstrations

This section shows several examples of GVF field computations on simple objects and demonstrates several key properties of GVF deformable contours. We used $\alpha = 0.6$ and $\beta = 0.0$ for all deformable contours and $\mu = 0.2$ for GVF. The deformable contours were dynamically reparameterized to maintain contour point separation to within 0.5–1.5 pixels (cf. [70]). All edge maps used in GVF computations were normalized to the range $[0, 1]$ in order to remove the dependency on absolute image intensity value.

3.4.1 Convergence to Boundary Concavity

In our first experiment, we computed the GVF field for the same U-shaped object used in Figs. 3.1 and 3.2. The results are shown in Fig. 3.3. Comparing the GVF field, shown in Fig. 3.3b, to the traditional potential force field of Fig. 3.1b, reveals several key differences. First, like the distance potential force field (Fig. 3.2b), the

[4] Mathworks, Natick MA

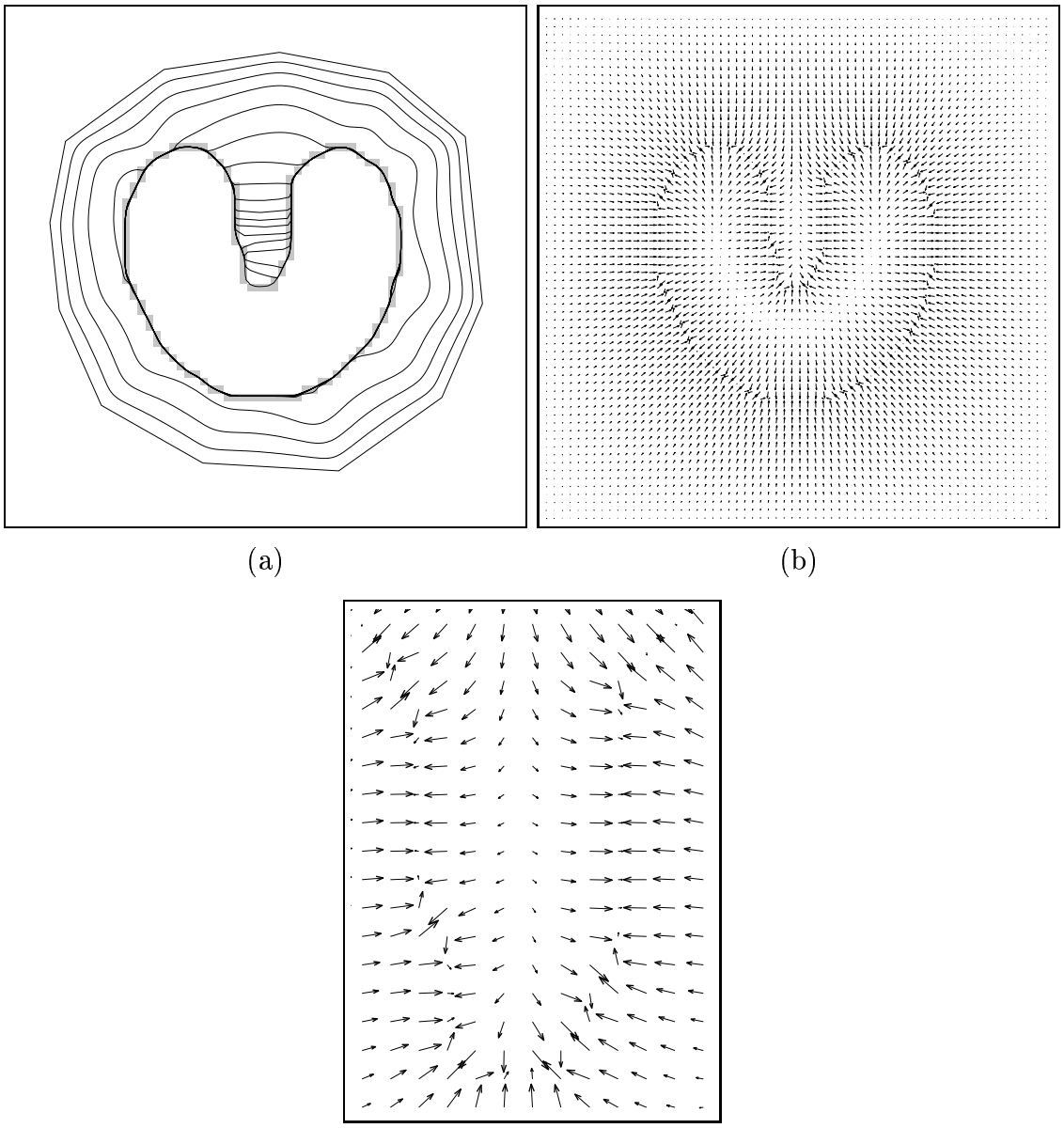

Figure 3.3: (a) The convergence of a deformable contour using (b) GVF external forces, (c) shown close-up within the boundary concavity.

GVF field has a much larger capture range than traditional potential forces. A second observation, which can be seen in the closeup of Fig. 3.3c, is that the GVF vectors within the boundary concavity at the top of the U-shape have a downward component. This stands in stark contrast to both the traditional potential forces of Fig. 3.1c and the distance potential forces of Fig. 3.2c. Finally, it can be seen from Fig. 3.3b that the GVF field behaves in an analogous fashion when viewed from the inside of the object. In particular, the GVF vectors are pointing upward into the "fingers" of the U shape, which represent concavities from this perspective.

Fig. 3.3a shows the initialization, progression, and final configuration of a GVF deformable contour. The initialization is the same as that of Fig. 3.2a, and the deformable contour parameters are the same as those in Figs. 3.1 and 3.2. Clearly, the GVF deformable contour has a broad capture range and superior convergence properties. The final deformable contour configuration closely approximates the true boundary, arriving at a sub-pixel interpolation through bilinear interpolation of the GVF force field.

3.4.2 Streamlines

Streamlines are the paths over which free particles move when placed in an external force field. By looking at their streamlines, we can examine the capture ranges and motion inducing properties for various deformable contour external forces. Fig. 3.4 shows the streamlines of points arranged on a 32×32 grid for the traditional potential forces, distance potential forces, and GVF forces used in the simulations of Figs. 3.1, 3.2, and 3.3.

Several properties can be observed from these figures. First, the capture ranges of the GVF force field and the distance potential force field are clearly much larger than that of the traditional potential force field. In fact, both distance potential forces and GVF forces will attract a deformable contour that is initialized on the image border. Second, it is clear that GVF is the only force providing both a downward force within the boundary concavity at the top of the U-shape and an upward force within the "fingers" of the U-shape. In contrast, both traditional deformable contour forces

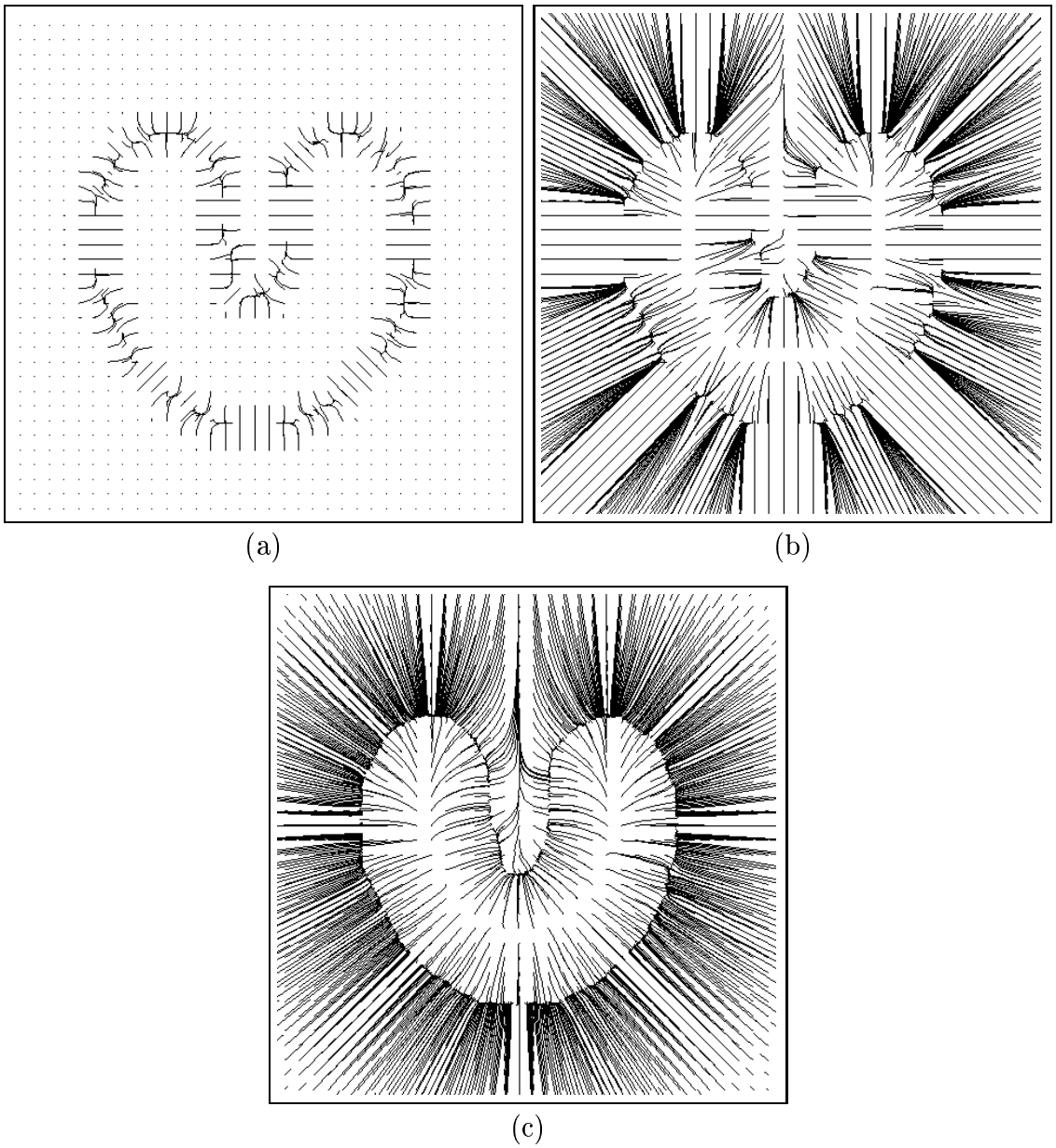

Figure 3.4: Streamlines originating from an array of 32×32 particles in (a) a traditional potential force field, (b) a distance potential force field, and (c) a GVF force field.

and distance potential forces provide only sideways forces in these regions. Third, the distance potential forces appear to have boundary points that act as regional points of attraction. In contrast, the GVF forces attract points uniformly toward the boundary.

3.4.3 Deformable Contour Initialization and Convergence

In this section we present several examples that compare different deformable contour models with the GVF deformable contour, showing various effects related to initialization, boundary concavities, and *subjective contours*. The object under study is the line drawing drawn in gray in both Figs. 3.5 and 3.6. This figure may depict, for example, the boundary of a room having two doors at the top and bottom and two alcoves at the left and right. The open doors at the top and bottom represent subjective contours that we desire to connect using the deformable contour (cf. [62]).

The deformable contour results shown in Figs. 3.5b–d all used the initialization shown in Fig. 3.5a. We first note that for this initialization, the traditional potential forces were too weak to overpower the deformable contour's internal forces, and the deformable contour shrank to a point at the center of the figure (result not shown). To try to fix this problem, a balloon model with outward pressure forces just strong enough to cause the deformable contour to expand into the boundary concavities was implemented; this result is shown in Fig. 3.5b. Clearly, the pressure forces also caused the balloon to bulge outward through the openings at the top and bottom, and therefore the subjective contours are not reconstructed well.

The deformable contour result obtained using the distance potential force model is shown in Fig. 3.5c. Clearly, the capture range is now adequate and the subjective boundaries at the top and bottom are reconstructed well. But this deformable contour fails to find the boundary concavities at the left and right, for the same reason that it could not proceed into the top of the U-shaped object of the previous sections. The GVF deformable contour result, shown in Fig. 3.5d, is clearly the best result. It has reconstructed both the subjective boundaries and the boundary concavities quite well. The slight rounding of corners, which can also be seen in Figs. 3.5b and 3.5c,

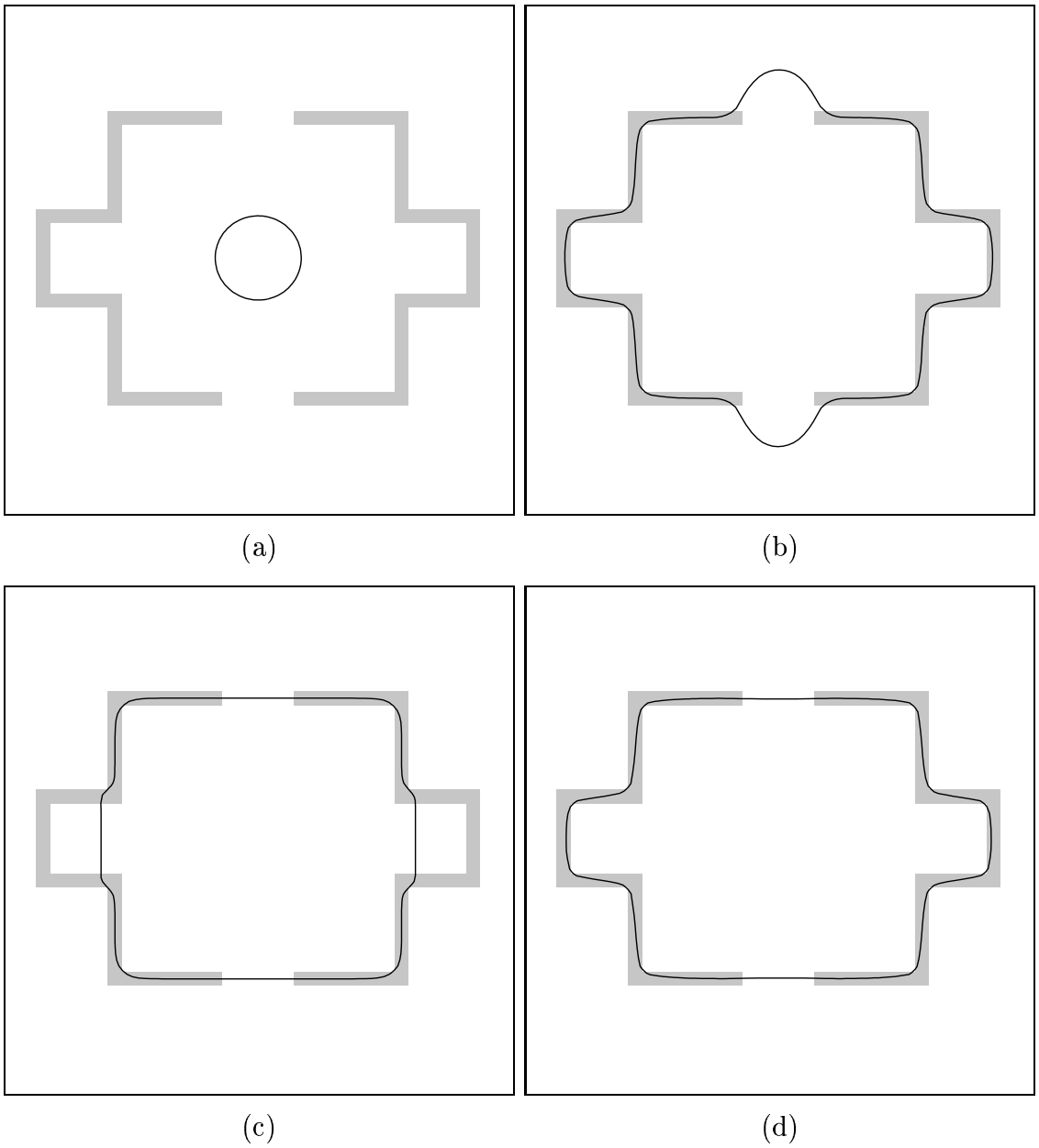

Figure 3.5: (a) An initial curve and deformable contour results from (b) a balloon with an outward pressure, (c) a distance potential force deformable contour, and (d) a GVF deformable contour.

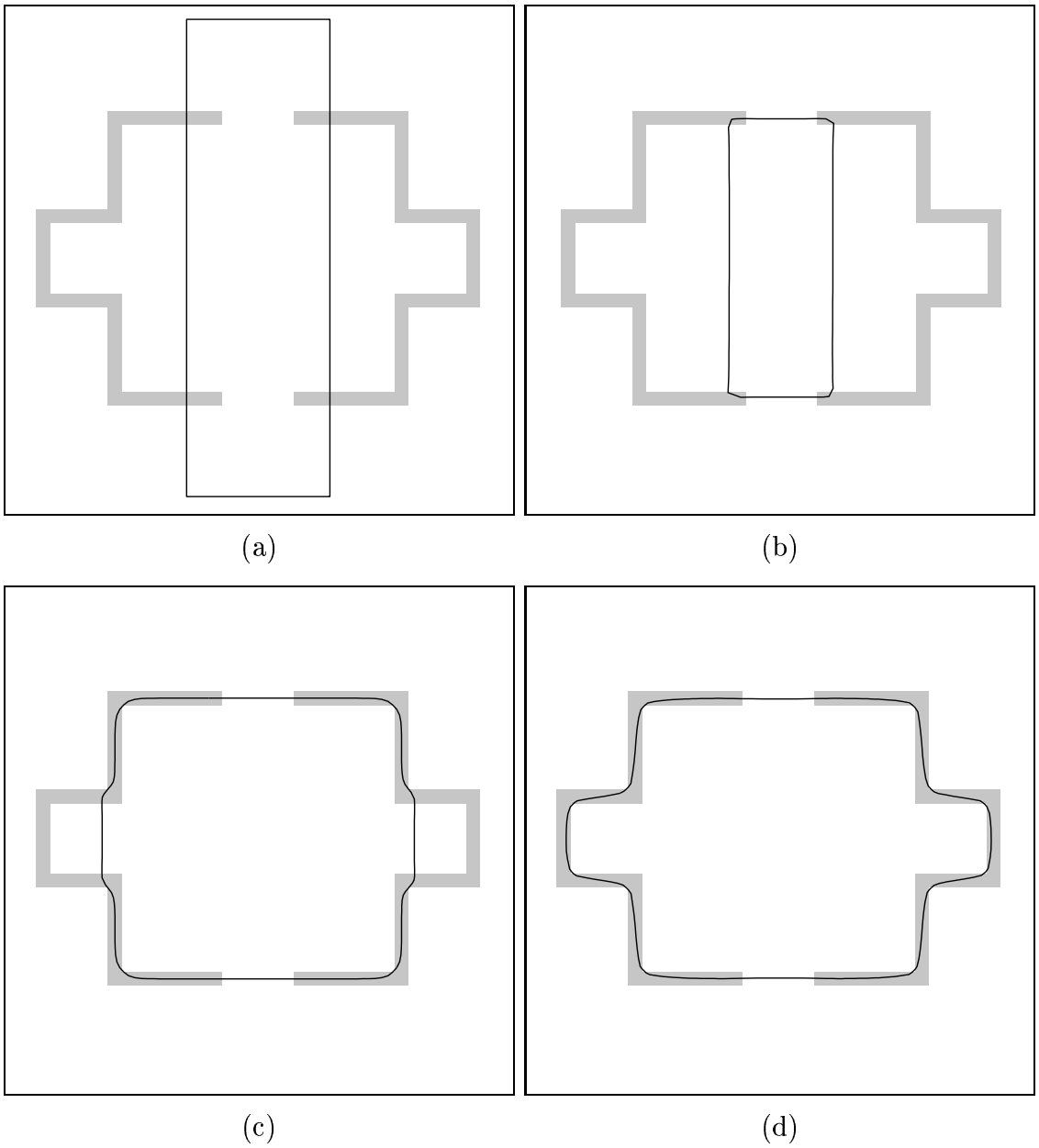

Figure 3.6: (a) An initial curve and deformable contour results from (b) a traditional deformable contour, (c) a distance potential force deformable contour, and (d) a GVF deformable contour.

is a fundamental characteristic of deformable contours caused by the regularization coefficients α and β.[5]

The deformable contour results shown in Figs. 3.6b–d all used the initialization shown in Fig. 3.6a, which is deliberately placed across the boundary. In this case, the balloon model cannot be sensibly applied because it is not clear whether to apply inward or outward pressure forces. Instead, the result of a deformable contour with traditional potential forces is shown in Fig. 3.6b. This deformable contour stops at a very undesirable configuration because its only points of contact with the boundary are normal to it and the remainder of the deformable contour is outside the capture range of the other parts of the boundary. The deformable contour resulting from distance potential forces is shown in Fig. 3.6c. This result shows that although the distance potential force deformable contour possesses an insensitivity to initialization, it is incapable of progressing into boundary concavities. The GVF deformable contour result, shown in Fig. 3.6d, is again the best result. The GVF deformable contour appears to have both an insensitivity to initialization and an ability to progress into boundary concavities.

3.5 Gray-level Images and Higher Dimensions

In this section, we describe and demonstrate how GVF can be used in gray-level imagery and in higher dimensions.

3.5.1 Gray-level Images

The underlying formulation of GVF is valid for gray-level images as well as binary images. To compute GVF for gray-level images, the edge-map function $f(x, y)$ must first be calculated. Two possibilities are $f^{(1)}(x, y) = |\nabla I(x, y)|$ or $f^{(2)}(x, y) = |\nabla(G_\sigma(x, y) * I(x, y))|$, where the latter is more robust in the presence of noise. Other more complicated noise-removal techniques such as median filtering, morphological filtering, and anisotropic diffusion could also be used to improve the underlying edge

[5]The effect is only caused by α in this example since $\beta = 0$.

map. Given an edge-map function and an approximation to its gradient, GVF is computed in the usual way using Eq. (3.8).

Fig. 3.7a shows a gray-level image of the U-shaped object corrupted by additive white Gaussian noise; the signal-to-noise ratio is 6 dB. Fig. 3.7b shows an edge-map computed using $f(x,y) = f^{(2)}(x,y)$ with $\sigma = 1.5$ pixels, and Fig. 3.7c shows the computed GVF field. It is evident that the stronger edge-map gradients are retained while the weaker gradients are smoothed out, exactly as would be predicted by the GVF energy formulation of (3.4). Superposed on the original image, Fig. 3.7d shows a sequence of GVF deformable contours (plotted in a shade of gray) and the GVF deformable contour result (plotted in white). The result shows an excellent convergence to the boundary, despite the initialization from far away, the image noise, and the boundary concavity.

Another demonstration of GVF applied to gray-scale imagery is shown in Fig. 3.8. Fig. 3.8a shows a magnetic resonance image (short-axis section) of the left ventrical of a human heart, and Fig. 3.8b shows an edge map computed using $f(x,y) = f^{(2)}(x,y)$ with $\sigma = 2.5$. Fig. 3.8c shows the computed GVF, and Fig. 3.8d shows a sequence of GVF deformable contours (plotted in a shade of gray) and the GVF deformable contour result (plotted in white), both overlaid on the original image. Clearly, many details on the endocardial border are captured by the GVF deformable contour result, including the papillary muscles (the bumps that protrude into the cavity).

3.5.2 Higher Dimensions

GVF can be easily generalized to higher dimensions. Let $f(\mathbf{x}) : \Omega \to \mathbf{R}$ be an edge map defined in $\Omega \subset \mathbf{R}^n$. The GVF field in Ω is defined as the vector field $\mathbf{v}(\mathbf{x}) : \Omega \to \mathbf{R}^n$ that minimizes the energy functional

$$\mathcal{E} = \int_\Omega \mu|\nabla \mathbf{v}|^2 + |\nabla f|^2 \, |\mathbf{v} - \nabla f|^2 d\mathbf{x} \tag{3.11}$$

where the gradient operator ∇ is applied to each component of $\mathbf{v}$ separately. Using the calculus of variations as described in Appendix 3.A, we find that the GVF field

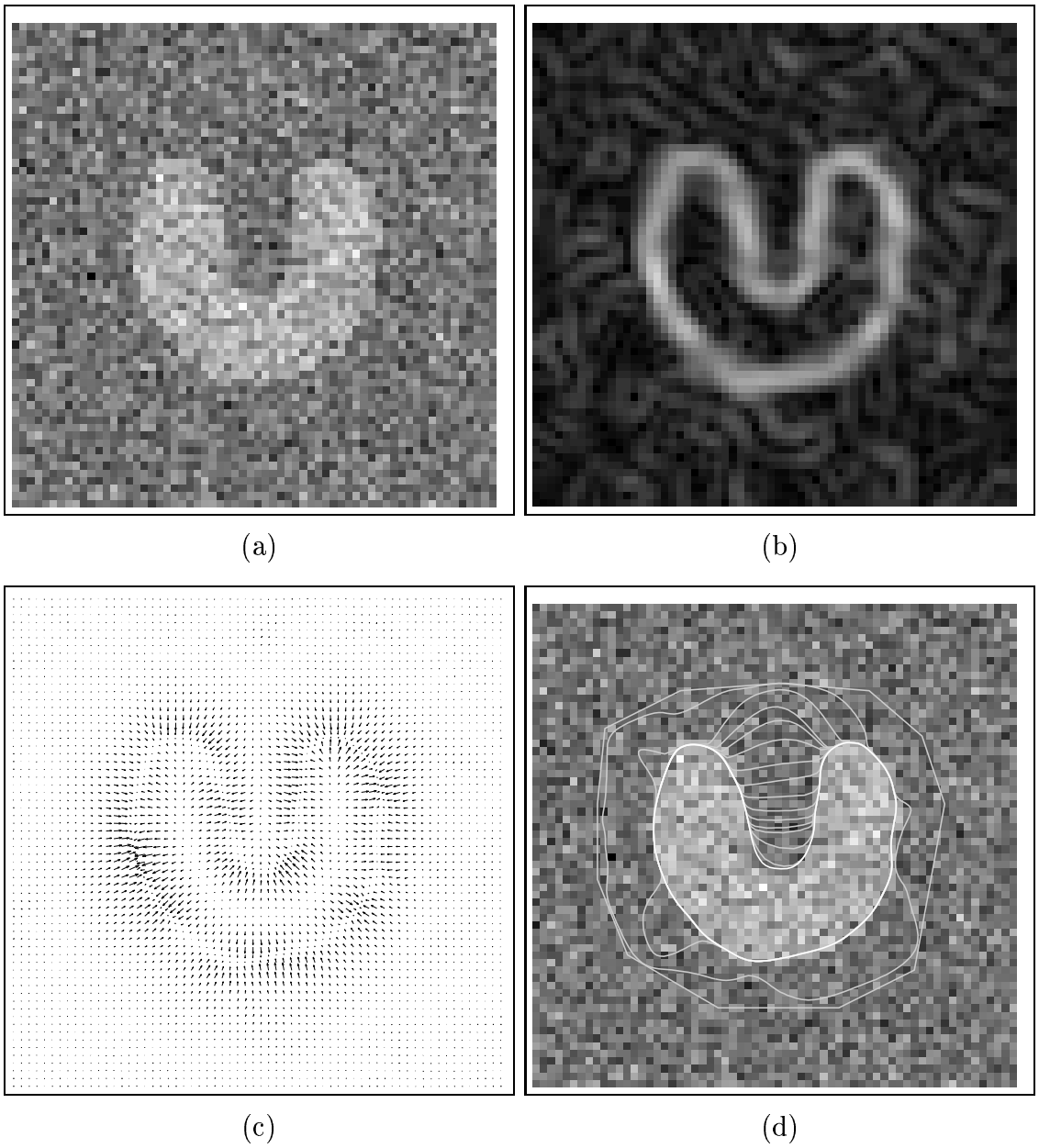

Figure 3.7: (a) A noisy 64×64-pixel image of a U-shaped object; (b) the edge map $|\nabla(G_\sigma * I)|^2$ with $\sigma = 1.5$; (c) the GVF external force field; and (d) convergence of the GVF deformable contour.

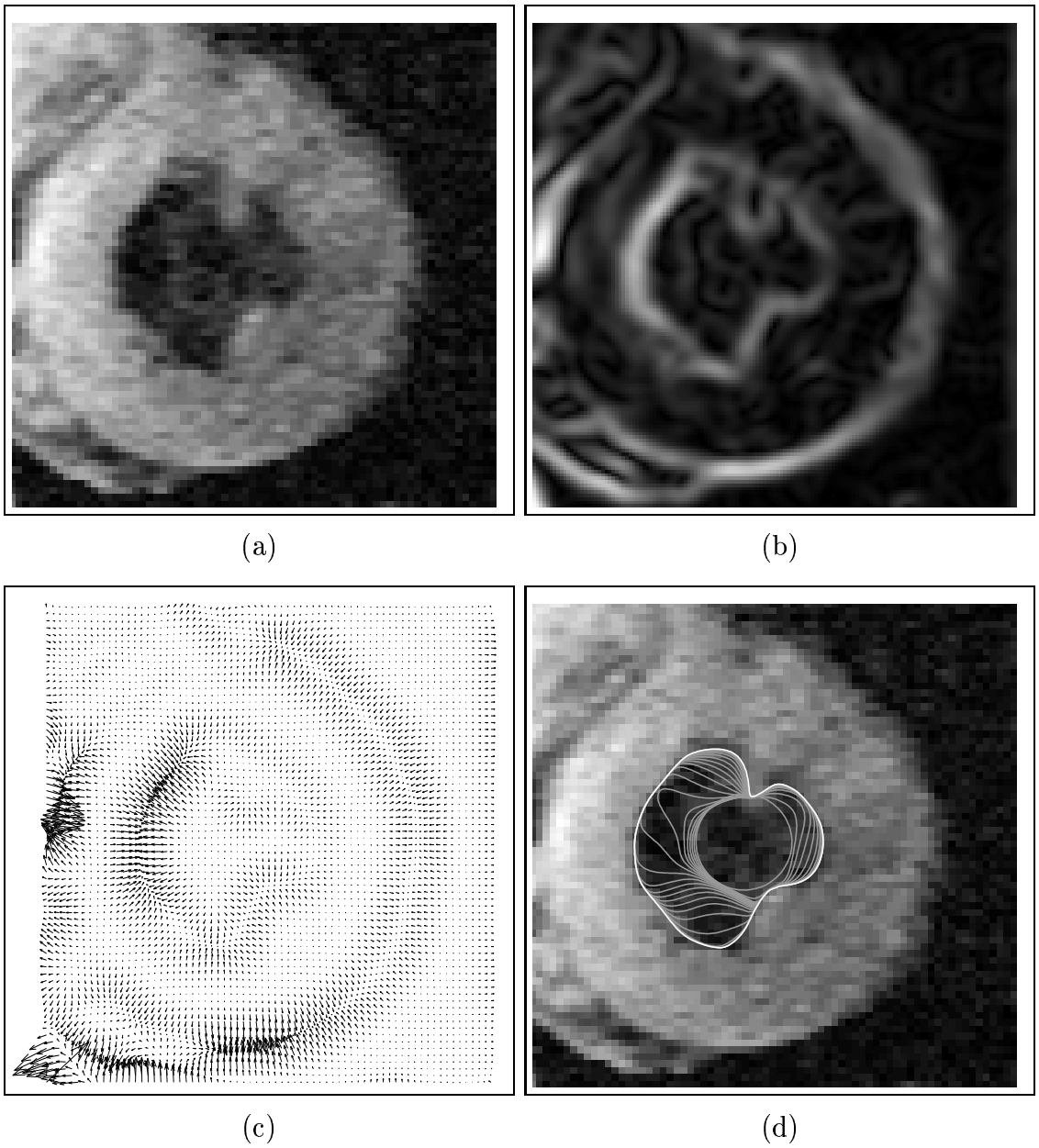

Figure 3.8: (a) A 160×160-pixel magnetic resonance image of the left ventrical of a human heart; (b) the edge map $|\nabla(G_\sigma * I)|^2$ with $\sigma = 2.5$; (c) the GVF field (shown subsampled by a factor of two); and (d) convergence of the GVF deformable contour.

must satisfy the Euler equation

$$\mu\nabla^2\mathbf{v} - (\mathbf{v} - \nabla f)|\nabla f|^2 = \mathbf{0} \tag{3.12}$$

where ∇^2 is also applied to each component of the vector field $\mathbf{v}$ separately.

A solution to these Euler equations can be found by introducing a time variable t and finding the steady-state solution of the following linear parabolic partial differential equation

$$\mathbf{v}_t = \mu\nabla^2\mathbf{v} - (\mathbf{v} - \nabla f)|\nabla f|^2 \tag{3.13}$$

where $\mathbf{v}_t$ denotes the partial derivative of $\mathbf{v}$ with respect to t. Equation (3.13) comprises n decoupled scalar linear second-order parabolic partial differential equations in each element of $\mathbf{v}$. Therefore, in principle, it can be solved in parallel. In analogous fashion to the 2-D case, finite differences can be used to approximate the required derivatives and each scalar equation can be solved iteratively.

An experiment using GVF in three dimensions was carried out using the object shown in Fig. 3.9a, which was created on a 64^3 grid, and rendered using an isosurface algorithm. This object belongs to a family of closed surfaces called *metaspheres* which is described in detail in Appendix 3.B. The 3-D GVF field was computed using a numerical approximation to (3.13) and $\mu = 0.15$. This GVF result on the two planes shown in Fig. 3.9b, is shown projected onto these planes in Figs. 3.9c and d. The same characteristics observed in 2-D GVF field are apparent here as well.

Next, a deformable surface using 3-D GVF was initialized as the sphere shown in Fig. 3.9e, which is neither entirely inside nor entirely outside the object. Intermediate results after 10 and 40 iterations of the deformable surface algorithm are shown in Figs. 3.9f and g. The final result after 100 iterations is shown in Fig. 3.9h. The resulting surface is smoother than the isosurface rendering in Fig. 3.9a because of the internal forces in the deformable surface model.

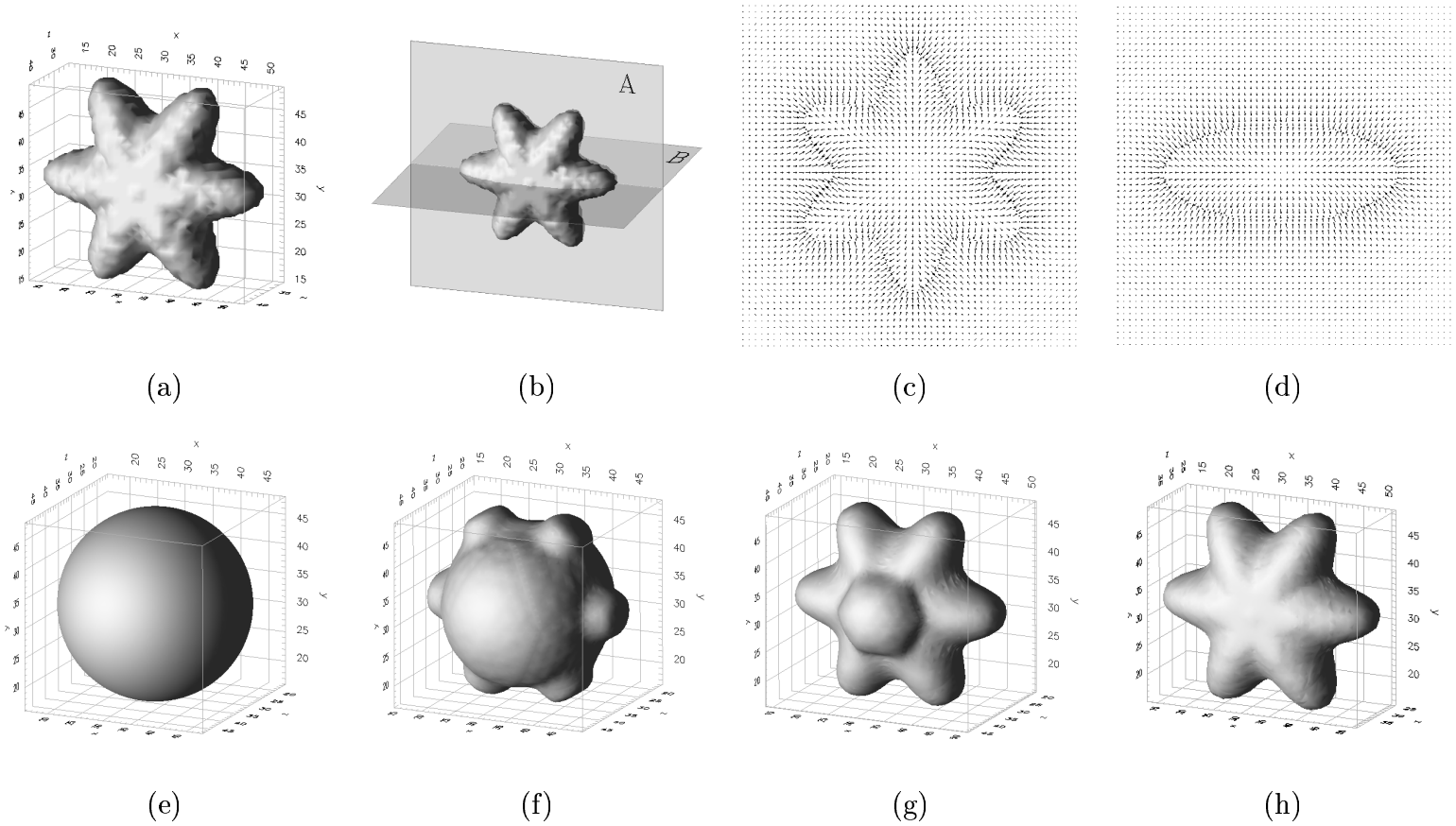

Figure 3.9: (a) Isosurface of a 3-D object defined on a 64^3 grid; (b) positions of planes A and B on which the 3-D GVF vectors are depicted in (c) and (d), respectively; (e) the initial configuration of a deformable surface using GVF and its positions after (f) 10, (g) 40, and (h) 100 iterations.

3.6 Summary

We have introduced a new external force model for deformable contours and surfaces, which we called the gradient vector flow (GVF) field. The field is calculated as a diffusion of the gradient vectors of a gray-level or binary edge map. We have shown that it allows for flexible initialization of deformable models and encourages convergence to boundary concavities, and that it is applicable in any dimension.

3.A Derivation of the GVF Euler Equation

In this appendix, we provide a detailed derivation of the GVF Euler equation (3.12) from its variational formulation in n dimensions.

Let us denote a point in n-dimensional space $\mathbf{R}^n$ by $\mathbf{x} = (x^1, \cdots, x^n)$, a scalar function at $\mathbf{x}$ by $f(\mathbf{x}) = f(x^1, \cdots, x^n)$, and a vector function at $\mathbf{x}$ by $\mathbf{v}(\mathbf{x}) = (v^1(x^1, \cdots, x^n), \cdots, v^n(x^1, \cdots, x^n))$. We further assume these functions are defined in a bounded domain $\Omega \subset \mathbf{R}^n$ with $\partial\Omega$ as its boundary.

GVF is defined as the vector function $\mathbf{v}(\mathbf{x})$ in the Sobolev space $W_2^2(\Omega)$ [52] that minimize the following functional

$$\int_\Omega \mu|\nabla\mathbf{v}|^2 + |\nabla f|^2|\mathbf{v} - \nabla f|^2 d\mathbf{x} \tag{3.14}$$

where $\nabla\mathbf{v}$ is a tensor and $|\nabla\mathbf{v}|$ is its vector norm. Note that $f(\mathbf{x})$ is a smooth function in $W_2^2(\Omega)$ since it is derived from a bounded scalar function convolving with a n-dimensional Gaussian function. Equation (3.14) can be rewritten in its component form as

$$\int_\Omega \mu \sum_{i=1}^{n}\sum_{j=1}^{n}(\frac{\partial v^i}{\partial x^j})^2 + \sum_{i=1}^{n}(v^i - \frac{\partial f}{\partial x^i})^2 \sum_{i=1}^{n}(\frac{\partial f}{\partial x^i})^2 d\mathbf{x} \tag{3.15}$$

For simplicity, we represent the above functional in a more general form

$$J = \int_\Omega F(x^1, \cdots, x^n, v^1, \cdots, v^n, \cdots, \frac{\partial v^1}{\partial x^1}, \cdots, \frac{\partial v^1}{\partial x^n}, \cdots, \frac{\partial v^n}{\partial x^1}, \cdots, \frac{\partial v^n}{\partial x^n})d\mathbf{x} \tag{3.16}$$

From calculus of variations [25], we know that

$$J = \int_\Omega F(x^1, \cdots, x^n, v^1, \cdots, v^n, \cdots, \frac{\partial v^1}{\partial x^1}, \cdots, \frac{\partial v^1}{\partial x^n}, \cdots, \frac{\partial v^n}{\partial x^1}, \cdots, \frac{\partial v^n}{\partial x^n})d\mathbf{x}$$

is stationary if and only if its first variation vanishes, i.e.,

$$\delta J = 0 \tag{3.17}$$

for every permissible variation $\delta v^i \in W_2^2(\Omega)$, $i = 1, \cdots, n$.

By applying the laws of variation [54], we can then proceed to derive the stationary solution to Eq. (3.17) as the following.

$$\begin{aligned}
\delta J &= \delta \int_\Omega F(x^1, \cdots, x^n, v^1, \cdots, v^n, \cdots, \frac{\partial v^1}{\partial x^1}, \cdots, \frac{\partial v^1}{\partial x^n}, \cdots, \frac{\partial v^n}{\partial x^1}, \cdots, \frac{\partial v^n}{\partial x^n}) d\mathbf{x} \\
&= \int_\Omega \delta F(x^1, \cdots, x^n, v^1, \cdots, v^n, \cdots, \frac{\partial v^1}{\partial x^1}, \cdots, \frac{\partial v^1}{\partial x^n}, \cdots, \frac{\partial v^n}{\partial x^1}, \cdots, \frac{\partial v^n}{\partial x^n}) d\mathbf{x} \\
&= \int_\Omega \left[\sum_{i=1}^n \frac{\partial F}{\partial v^i} \delta v^i + \sum_{i=1}^n \sum_{j=1}^n \frac{\partial F}{\partial v_j^i} \delta v_j^i d\mathbf{x} \right], \quad (v^i \equiv \frac{\partial v^i}{\partial x^j}) \\
&= \sum_{i=1}^n \left[\int_\Omega \frac{\partial F}{\partial v^i} \delta v^i d\mathbf{x} + \int_\Omega \sum_{j=1}^n \frac{\partial F}{\partial v_j^i} \delta v_j^i d\mathbf{x} \right].
\end{aligned}$$

Using integration by parts, we have

$$\delta J = \sum_{i=1}^n \left[\int_\Omega \frac{\partial F}{\partial v^i} \delta v^i d\mathbf{x} - \sum_{j=1}^n \int_\Omega \frac{\partial}{\partial x^j} \left(\frac{\partial F}{\partial v_j^i} \right) \delta v^j d\mathbf{x} + \sum_{j=1}^n \int_{\partial\Omega} \frac{\partial F}{\partial v_j^i} \delta v^i \eta^i dS \right]$$

where η^i is the projection of outward normal unit vector $\boldsymbol{\eta}$ along x^i axis at $\partial\Omega$ and dS represents the element of area on the boundary $\partial\Omega$. After rearranging the above equation, we obtain

$$\delta J = \sum_{i=1}^n \int_\Omega \left[\frac{\partial F}{\partial v^i} - \sum_{j=1}^n \frac{\partial}{\partial x^j} \left(\frac{\partial F}{\partial v_j^i} \right) \right] \delta v^j d\mathbf{x} + \sum_{i=1}^n \sum_{j=1}^n \int_{\partial\Omega} \frac{\partial F}{\partial v_j^i} \eta^i \delta v^i dS = 0.$$

Since variations of δv^i, $i = 1, \cdots, n$ are independent of each other, it follows that all the coefficients of δv^i in the integrands of all the integrals must each vanish identically in Ω, giving n scalar Euler equations

$$\frac{\partial F}{\partial v^i} - \sum_{j=1}^n \frac{\partial}{\partial x^j} \left(\frac{\partial F}{\partial v_j^i} \right) = 0 \tag{3.18}$$

and n natural boundary conditions

$$\sum_{j=1}^n \frac{\partial F}{\partial v_j^i} \eta^i = 0 \tag{3.19}$$

where $i = 1, \cdots, n$. Substituting the definition of F in Eq. (3.15) and after some algebra, we obtain the Euler equations and boundary conditions for GVF as follows:

$$\mu \sum_{j=1}^{n} \frac{\partial^2 v^i}{\partial (x^j)^2} - \left(v^i - \frac{\partial f}{\partial x^j} \right) \left(\frac{\partial f}{\partial x^j} \right)^2 = 0 \tag{3.20}$$

$$\sum_{j=1}^{n} \frac{\partial v^i}{\partial x^j} \eta^i = 0 \text{ on } \partial\Omega \tag{3.21}$$

where $i = 1, \cdots, n$. Equation (3.20) and (3.21) can be written in a compact form using the vector notation

$$\mu \nabla^2 \mathbf{v} - (\mathbf{v} - \nabla f)|\nabla f|^2 = 0 \tag{3.22}$$

$$\nabla \mathbf{v} \cdot \boldsymbol{\eta} = 0 \text{ on } \partial\Omega \tag{3.23}$$

This is a decoupled vector partial differential equation (PDE) with a Neumann boundary condition. Each of its scalar equations is a linear, second-order, variable coefficient PDE of the elliptic type. It has been shown that these scalar equations of GVF are uniquely solvable [92, 26][6].

3.B Metaspheres

In this appendix, we describe a family of closed surfaces that can be used to generate 3-D computational phantoms. These surfaces, which we call *metaspheres*, are a generalization of basic harmonic curves given in [112].

Let us define $\mathbf{x} = (x, y, z)$, $\mathbf{a} = (a_x, a_y, a_z)$, $\mathbf{b} = (b_x, b_y, b_z)$, $\mathbf{m} = (m_x, m_y, m_z)$, and $\mathbf{n} = (n_x, n_y, n_z)$. Then a metasphere $\mathbf{x}(\theta, \phi)$ is given by

$$x = (a_x + b_x \cos(m_x\theta)\cos(n_x\phi))\sin(\theta)\cos(\phi) \tag{3.24a}$$

$$y = (a_y + b_y \cos(m_y\theta)\cos(n_y\phi))\sin(\theta)\sin(\phi) \tag{3.24b}$$

$$z = (a_z + b_z \cos(m_z\theta)\cos(n_z\phi))\cos(\theta) \tag{3.24c}$$

where $0 \leq \theta < \pi$, $0 \leq \phi < 2\pi$, and (a_x, a_y, a_z) is the metasphere radius in the directions of three axes, (b_x, b_y, b_z) is the ripple amplitude of harmonics components

[6]We would like to thank Diego Socolinsky for pointing out the references to the solvability of the GVF Euler equation.

on the metasphere, and (m_x, m_y, m_z) and (n_x, n_y, n_z) are the ripple frequencies. Three examples of metasphere surfaces generated from Eq. (3.24) are shown in Figs. 3.10 a-c.

It is possible to bend the metasphere to add the variety of possible shape. A metasphere that bends in x-y plane, $\tilde{\mathbf{x}}(\theta, \phi) = (\tilde{x}, \tilde{y}, \tilde{z})$, is given by

$$\tilde{x} = x\cos(cx) + y\sin(cx) \tag{3.25a}$$

$$\tilde{y} = -x\cos(cx) + y\sin(cx) \tag{3.25b}$$

$$\tilde{z} = z \tag{3.25c}$$

where c is a parameter that adjusts the amount of bending. Bending in other planes is analogously defined. Fig. 3.10d shows a simple metasphere with bending.

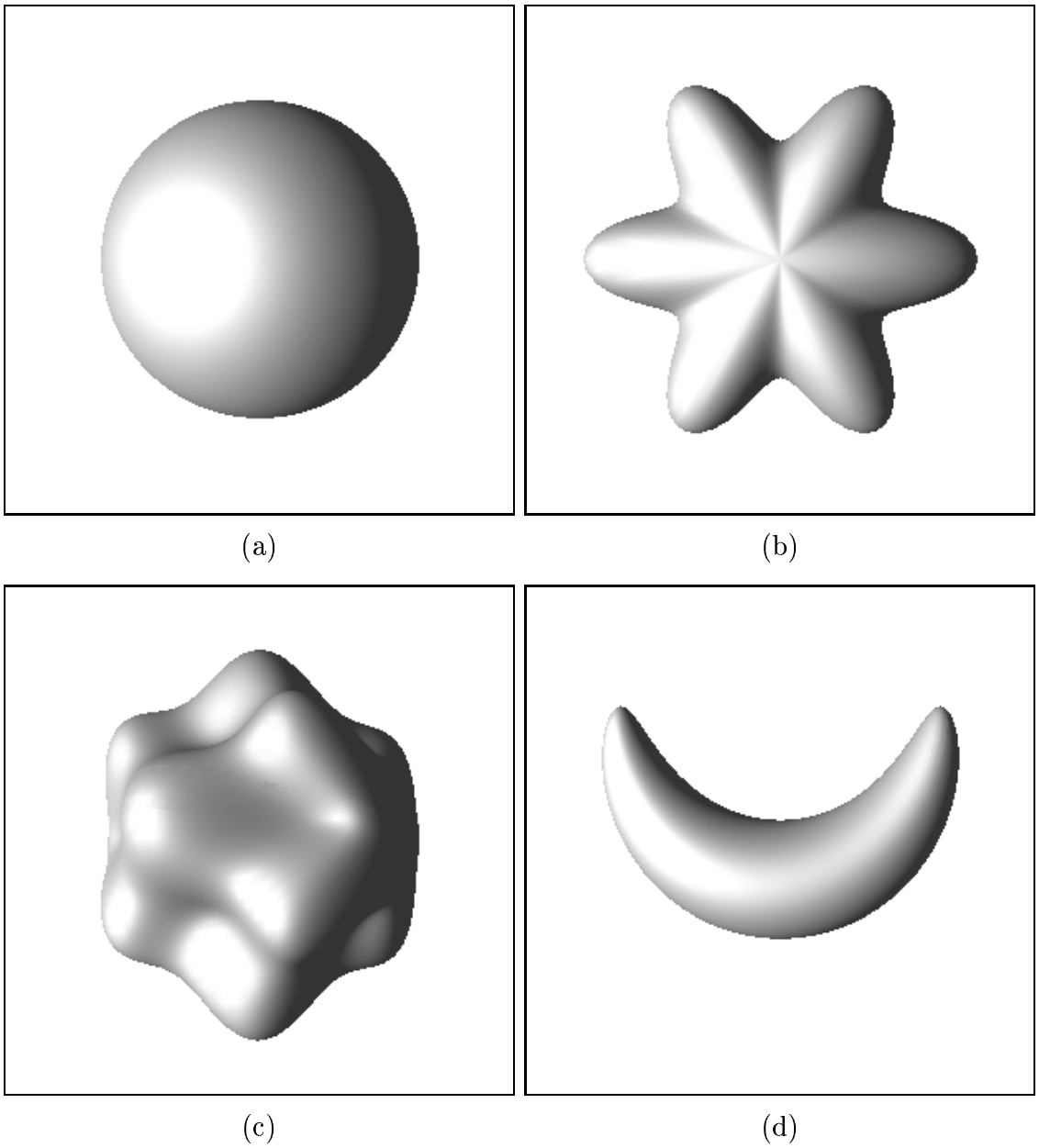

Figure 3.10: Sample metaspheres: (a) $\mathbf{a} = (2, 2, 2)$, $\mathbf{b} = \mathbf{0}$, $\mathbf{m} = \mathbf{0}$, $\mathbf{n} = \mathbf{0}$, and $c = 0$; (b) $\mathbf{a} = (2, 2, 1)$, $\mathbf{b} = (0.5, 0.5, 0)$, $\mathbf{m} = \mathbf{0}$, $\mathbf{n} = (6, 6, 6)$, and $c = 0$; (c) $\mathbf{a} = (2, 2, 2)$, $\mathbf{b} = (0.5, 0.5, 0)$, $\mathbf{m} = (4, 4, 4)$, $\mathbf{n} = (4, 4, 4)$, and $c = 0$; and (d) $\mathbf{a} = (2, 0.5, 0.5)$, $\mathbf{b} = \mathbf{0}$, $\mathbf{m} = \mathbf{0}$, $\mathbf{n} = \mathbf{0}$, and $c = -0.4$.

Chapter 4

Generalized Gradient Vector Flow Deformable Models

In the previous chapter, we developed a new external force, called gradient vector flow (GVF), The GVF field has a large capture range, which means that the deformable model can be initialized far away from the target boundary. The GVF field also tends to force the deformable model into boundary concavities, where the traditional deformable model have poor convergence. It still has difficulties, however, forcing a deformable model into long, thin boundary indentations, which is a crucial requirement in applications such as brain cortex reconstruction.

In this chapter, we generalize the GVF formulation to include two spatially-varying weighting functions. These weighting functions define a tradeoff between smoothness of the resulting GVF field and its conformity to the gradient of the underlying edge map. The external force fields derived from this new *generalized GVF* (GGVF) improve the deformable model convergence into long, thin boundary indentations, while maintaining other desirable properties of GVF, such as the extended capture range. The original GVF is a special case of GGVF. In order to compare the performance between GGVF deformable models and others, we performed a quantitative analysis on a series of simulated test images and show the corresponding results.

In addition to being used as an external force field, GGVF can also be used as a new type of image representation. In particular, it synthesizes a medial property of a

shape together with its boundary information. The medial property plays an important role in shape analysis and computer vision and we shall describe a preliminary study of medialness derived from the GGVF. An immediate application of GGVF medialness is that we can use GGVF deformable models to reconstruct the central layer of a thick boundary. Finally, we present an alternative generalization of GVF through a variational formulation. This generalization satisfies a minimum principle and results in similar performance as GGVF but requires more computations. We note that all the GGVF formulas described in this chapter are presented in a vector notation so that it can be used in any dimension, however, we give examples and results in two-dimensional for convenience.

4.1 Generalized GVF

As was described in the previous chapter, GVF has many desirable properties as an external force for deformable models. It still has difficulties, however, forcing a deformable model into long, thin boundary indentations. We hypothesized that this difficulty could be caused by excessive smoothing of the GVF field near the boundaries, governed by the coefficient μ in (3.13). We reasoned that introducing a spatially-varying weighting function, instead of the constant μ, and decreasing the smoothing effect near strong gradients, could solve this problem. In the following formulation, which we have termed *generalized GVF* (GGVF), we replace both μ and $|\nabla f|^2$ in (3.13) by more general weighting functions. An alternative generalization, which follows from a variational formulation, is given in Section 4.5.

We define GGVF as the equilibrium solution of the following vector partial differential equation

$$\mathbf{v}_t = g(|\nabla f|)\nabla^2\mathbf{v} - h(|\nabla f|)(\mathbf{v} - \nabla f) \tag{4.1}$$

The first term on the right is referred to as the *smoothing term* since this term alone will produce a smoothly varying vector field. The second term is referred as the *data term* since it encourages the vector field $\mathbf{v}$ to be close to ∇f computed from the edge map. The weighting functions $g(\cdot)$ and $h(\cdot)$ apply to the smoothing and data terms,

respectively. Since these weighting functions are dependent on the gradient of the edge map which is spatially varying, the weights themselves are spatially varying, in general. Since we want the vector field $\mathbf{v}$ to be slowly-varying (or smooth) at locations far from the edges, but to conform to ∇f near the edges, $g(\cdot)$ and $h(\cdot)$ should be monotonically non-increasing and non-decreasing functions of $|\nabla f|$, respectively.

The above equation reduces to that of GVF when

$$g(|\nabla f|) = \mu \tag{4.2}$$

$$h(|\nabla f|) = |\nabla f|^2 \tag{4.3}$$

Since $g(\cdot)$ is constant here, smoothing occurs everywhere; however, $h(\cdot)$ grows larger near strong edges, and should dominate at the boundaries. Thus, GVF should provide good edge localization. The effect of smoothing becomes apparent, however, when there are two edges in close proximity, such as when there is a long, thin indentation along the boundary. In this situation, GVF tends to smooth between opposite edges, losing the forces necessary to drive a deformable contour into this region.

To address this problem, weighting functions can be selected such that $g(\cdot)$ gets smaller as $h(\cdot)$ becomes larger. Then, in the proximity of large gradients, there will be very little smoothing, and the effective vector field will be nearly equal to the gradient of the edge map. There are many ways to specify such pairs of weighting functions. In this thesis, we use the following weighting functions for GGVF

$$g(|\nabla f|) = e^{-(\frac{|\nabla f|}{\kappa})^2} \tag{4.4}$$

$$h(|\nabla f|) = 1 - g(|\nabla f|) \tag{4.5}$$

The GGVF field computed using this pair of weighting functions will conform to the edge map gradient at strong edges, but will vary smoothly away from the boundaries. The specification of κ determines to some extent the degree of tradeoff between field smoothness and gradient conformity. Weighting functions for both GVF and GGVF are plotted in Figs. 4.1a and 4.1b respectively.

Like GVF, the partial differential equation (4.1) specifying GGVF, can be implemented using an explicit finite difference scheme, which is stable if the time step Δt

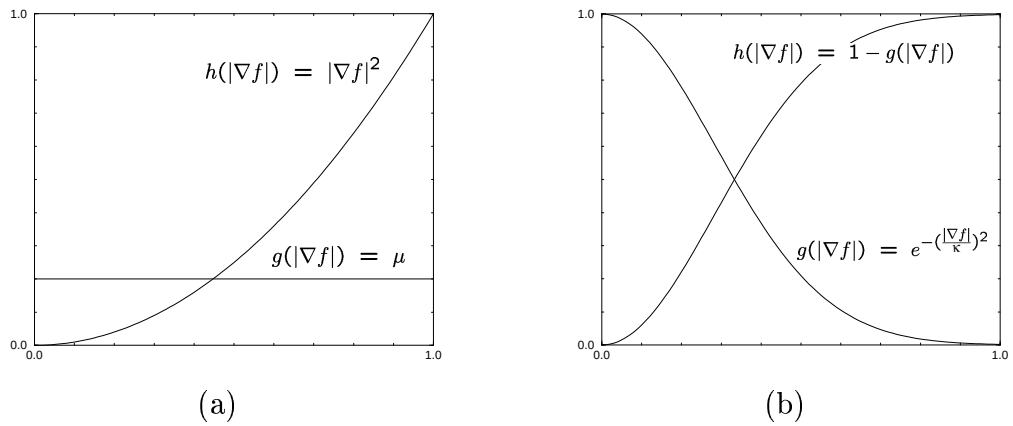

Figure 4.1: Plots of both (a) the GVF and (b) the GGVF weighting functions.

and the spatial sample intervals Δx and Δy satisfy

$$\Delta t \leq \frac{\Delta x \Delta y}{4 g_{\max}}$$

where $g_{\max}$ is the maximum value of $g(\cdot)$ over the range of gradients encountered in the edge map image. While an implicit scheme for the numerical implementation of (4.1) would be unconditionally stable and therefore not need this condition, the explicit scheme is faster. Still faster methods — for example, the multigrid method — are possible.

4.2 Experimental Results

In conducting the following experiments, all edge maps used in GVF computations were normalized to the range $[0, 1]$ in order to remove the dependency on absolute image intensity value. The deformable contours were dynamically reparameterized to maintain contour point separation to within 0.5–1.5 pixels (cf. [70]). The GVF, GGVF, and deformable contour parameters are given for each case.

A comparison between the performance of the GVF deformable contour and the GGVF deformable contour is shown in Fig. 4.2. Using an edge map obtained from the

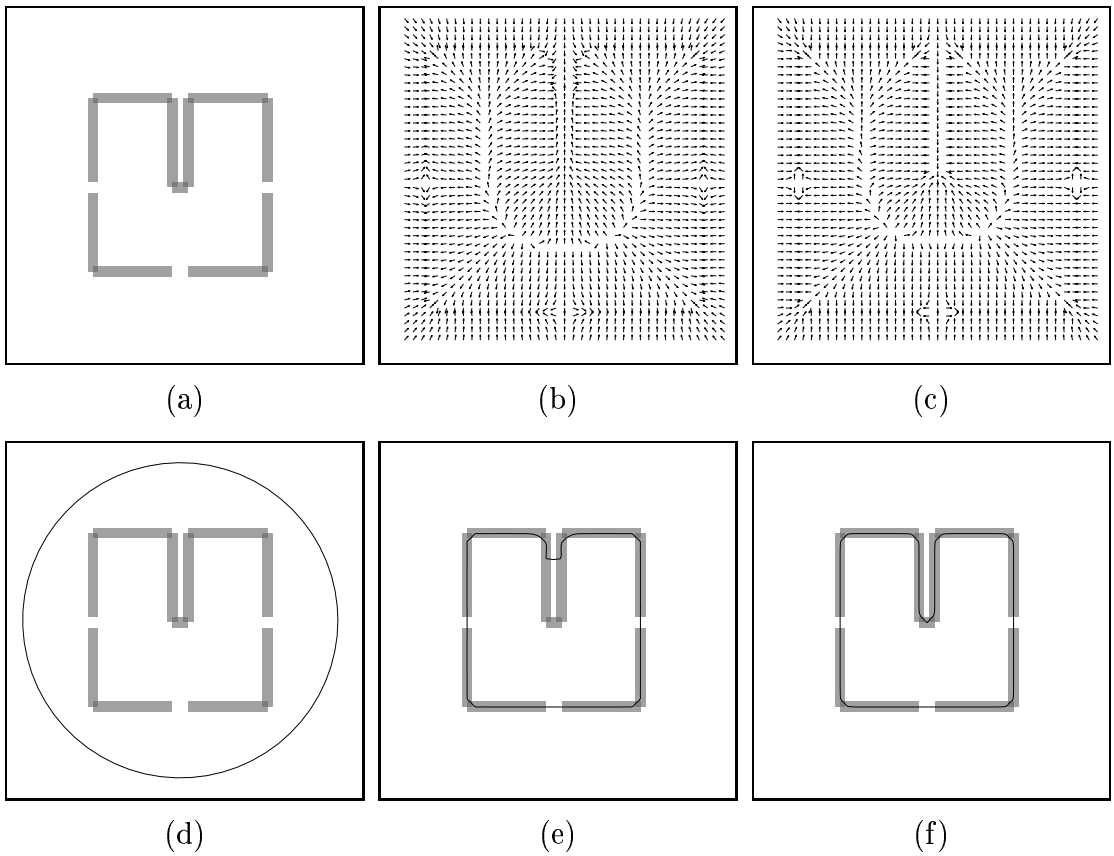

Figure 4.2: (a) A square with a long, thin indentation and broken boundary; (b) original GVF field (zoomed); (c) proposed GGVF field (zoomed); (d) initial contour position for both the GVF deformable contour and the GGVF deformable contour; (e) final result of the GVF deformable contour; and (f) final result of the GGVF deformable contour.

original image shown in Fig. 4.2a, both the GVF field ($\mu = 0.2$) and the GGVF field ($\kappa = 0.05$) were computed, as shown zoomed in Figs. 4.2b and 4.2c, respectively. We note that in this experiment both the GVF field and the GGVF field were normalized with respect to their magnitudes and used as external forces. Next, a deformable contour ($\alpha = 0.25$, $\beta = 0$) was initialized at the position shown in Fig. 4.2d and allowed to converge within each of the external force fields. The GVF result, shown in Fig. 4.2e, stops well short of convergence to the long, thin, boundary indentation. On the other hand, the GGVF result, shown in Fig. 4.2f, is able to converge completely to this same region. It should be noted that both GVF and GGVF have wide capture ranges (which is evident because the initial contour is fairly far away from the object), and they both preserve subjective contours (meaning that they cross the short boundary gaps).

It turns out that a good result similar to that of GGVF in Fig. 4.2f can be achieved using GVF with $\mu = 0.01$. Because μ is small in homogeneous regions as well as near the edges, the convergence of GVF is very slow — it takes an order of magnitude longer than GGVF or GVF with $\mu = 0.2$. If the GVF iterations are terminated early, then the result has an undesirably small capture range. This result shows that GGVF can be thought of as a faster GVF that preserves boundary detail and has a large capture range. The GGVF and GVF results will never be exactly the same, however, since the smoothing parameter of GGVF goes to zero at edges, an impossibility for GVF.

We compared the accuracy of different deformable contour formulations using the simple harmonic curves. These curves were generated according to the equation

$$r = a + b\cos(m\theta + c) \tag{4.6}$$

by setting a, b, c to suitable values and varying m. Curves corresponding to $m = 0$, 2, 4, 6, and 8 were digitized on a 201×201 grid to give the images in Fig. 4.3. In order to eliminate the problem of capture range for traditional deformable contours so that comparisons could be made, we initialized the deformable contours at the true curves, and let them deform under the different external forces. After convergence, we computed the maximum distance in the radial direction between the true boundary

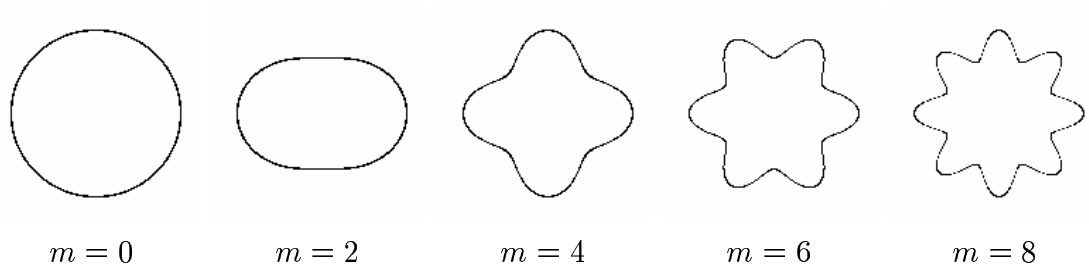

Figure 4.3: Harmonic curves: $r = a + b\cos(m\theta + c)$

and each deformable contour as in [33]. To compute the maximum radial error (MRE), all the final deformable contours were linearly interpolated to maintain a pre-specified small point separation. The maximum radial errors were measured in terms of pixels.

Our experimental results on accuracy are shown in Fig. 4.4. The first three curves shown in this figure resulted from traditional deformable contour external forces $-\nabla E_{\text{ext}} = -\nabla(G_\sigma(x,y) * I(x,y))$ for three Gaussian standard deviations ($\sigma = 1$ pixel, $\sigma = 3$ pixels, and $\sigma = 6$ pixels). The fourth curve resulted from the use of the distance potential forces of Cohen and Cohen [21]. The last two resulted from GVF ($\mu = 0.1$) and GGVF ($\kappa = 0.05$). In both cases the test intensity images were used as edge maps. We see that traditional potential forces with small σ yield small errors. Since the capture range of this type of force is very small, larger σ's are often used. As the figure shows these forces do not yield high accuracy, especially at larger m's. The distance potential forces, GVF forces, and GGVF forces, all yield high accuracy consistently. We have shown in Chapter 3 that distance potential forces, however, have poor performance on objects with boundary concavities. We note that the fluctuations of the error curves with increasing m arise due to discretization of the curves on the image grid and to the underlying performance variations of deformable contours.

Deformable contour algorithms can sometimes be extremely sensitive to noise. To test the noise sensitivity of GVF and GGVF, we added impulse noise to the $m = 8$ harmonic image in Fig. 4.3. The resulting image is shown in Fig. 4.5a with an initial deformable contour plotted as a circle. The deformable contour was then

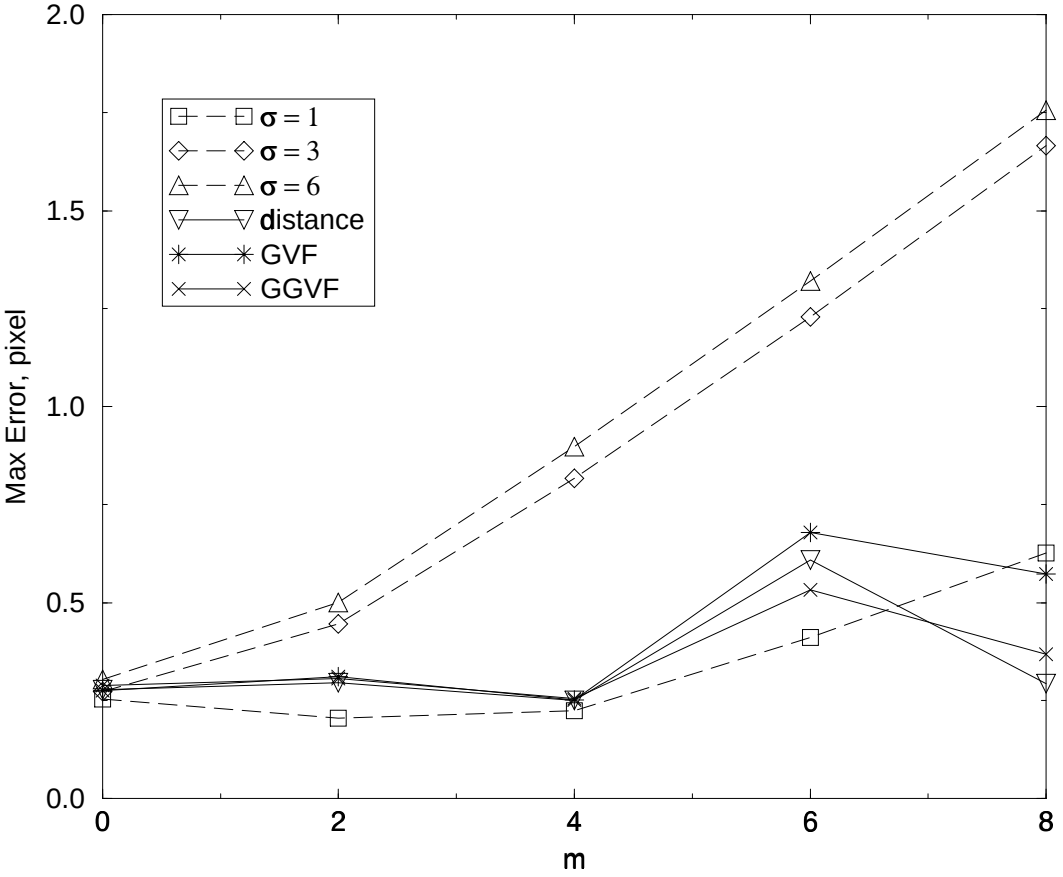

Figure 4.4: Maximum radial error (MRE).

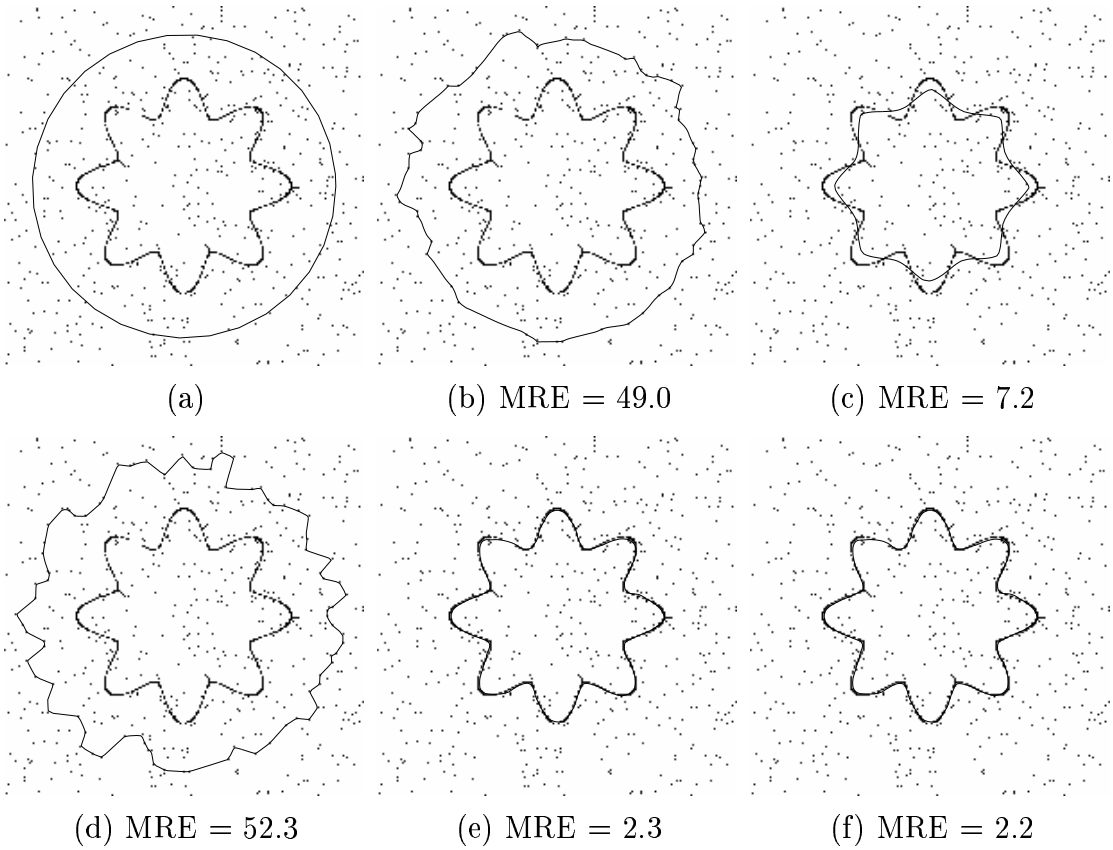

Figure 4.5: (a) Impulse noise corrupted image and the initial deformable contour; (b) and (c) deformable contour results using traditional external forces $\nabla(G_\sigma(x,y) * I(x,y))$ where $\sigma = 1$ and 9; (d) deformable contour result using distance potential force; (e) GVF deformable contour result with $\mu = 0.1$; and (f) GGVF deformable contour result with $\kappa = 0.2$. The edge map used for both GVF and GGVF is $f = G_\sigma(x,y) * I(x,y)$, where $\sigma = 1$, respectively. All deformable contour results are computed using $\alpha = 0.25$ and $\beta = 0$.

allowed to converge, being driven by external force fields calculated from the noisy image. The results for traditional deformable contours with $\sigma = 1$ and $\sigma = 9$ are shown in Figs. 4.5b and 4.5c, respectively. The problem with Fig. 4.5b is that the deformable contour is simply captured by the local impulsive spikes, rather than the dominant figure. In Fig. 4.5c, the large σ blurs the boundary too much and the deformable contour cannot latch onto the detail. The contour resulting from the distance potential forces is shown in Fig. 4.5d. Since this external force uses a binary edge map to begin with, it is attracted to the nearest detected edge points, which do not belong to the dominant figure. The results for both GVF and GGVF deformable contours are shown in Figs. 4.5e and 4.5f, respectively. These results, barely distinguishable from each other, demonstrate their abilities to be both captured from a long distance and to converge extremely well to the dominant shape.

It is natural to ask whether there might be a smoothing strategy that would improve the results of the distance potential forces. For example, it may be possible to improve the edge map by prefiltering the image before creating the edge map or by applying a nonlinear filter to the edge map itself. We have tried several approaches along these lines and have found that it is very difficult to eliminate extraneous boundary points while simultaneously preserving the boundary itself. Another approach is to filter the distance potential itself in order to smooth out the energy valleys caused by the extraneous edge points. This approach flattens the valley in which the true edge is located and does not eliminate the extraneous valleys, and the converged deformable contour has poor fidelity to the truth.

GVF and GGVF both improve over the distance potential forces by applying a very narrow filter to the edge map followed by a vector diffusion that allows the dominant edge map to obliterate the effects of the extraneous edge points scattered throughout the image. It should be noted that if GVF were run with a small μ parameter, it would not smooth out the extraneous edges. This highlights an important advantage of GGVF over GVF: that GGVF can support convergence to very thin boundary concavities while simultaneously eliminating extraneous edge points.

Finally, we compared the qualitative performance of GVF and GGVF deformable contours on a magnetic resonance image of the left ventricle of a human heart. The

original image is shown in Fig. 4.6a, and its gray-level edge map is shown in Fig. 4.6b. The goal in this experiment is to extract the boundary description of the inner wall or endocardium of the left ventricle. The initial positions of both GVF and GGVF deformable contours are shown as circles in gray overlaid on the real images (Figs. 4.6c and 4.6d). The final contours are shown in white. Many details of the endocardial border are captured by both GVF and GGVF; however, the papillary muscle protruding into the cavity at about the 1 o'clock position is represented best by GGVF.

In many cases, GGVF and GVF will perform very similarly. Our experiments have revealed certain differences, however, and these may be important in practice. GGVF will generally show better convergence to thin boundary concavities. If the μ parameter is sufficiently small, however, GVF may achieve similar convergence properties. But in this case, GVF will require significantly longer computation time, and noise in the edge map may cause erroneous convergence. In short, GGVF can be thought of as a computationally faster version of GVF, with better boundary localization, especially with respect to concave boundaries, and with better noise immunity.

4.3 GGVF and Shape Analysis

In addition to its use as an external field for deformable models, GGVF appears to have interesting connections to the medial axis analysis of shape. The *medial axis transform* (MAT) [9] has long been used to describe both an object's shape and the relationship among an object's natural parts [88]. The MAT representation is known to be extremely sensitive to small boundary perturbations, however. To address this difficulty, Pizer *et al.* [87] introduced the *multi-scale medial axis transform* or *core* which incorporates a scale space into the MAT by computing the maximum *medialness* over scale. Medialness is a measure of how close a point is to an object's skeleton. Because core analysis operates across scales, it reduces the noise sensitivity of the MAT yet maintains almost all the desirable properties of MAT. In this section, we show that by applying a simple algebraic transformation on the magnitude of a GGVF field, we get a representation strongly resembling a medialness function.

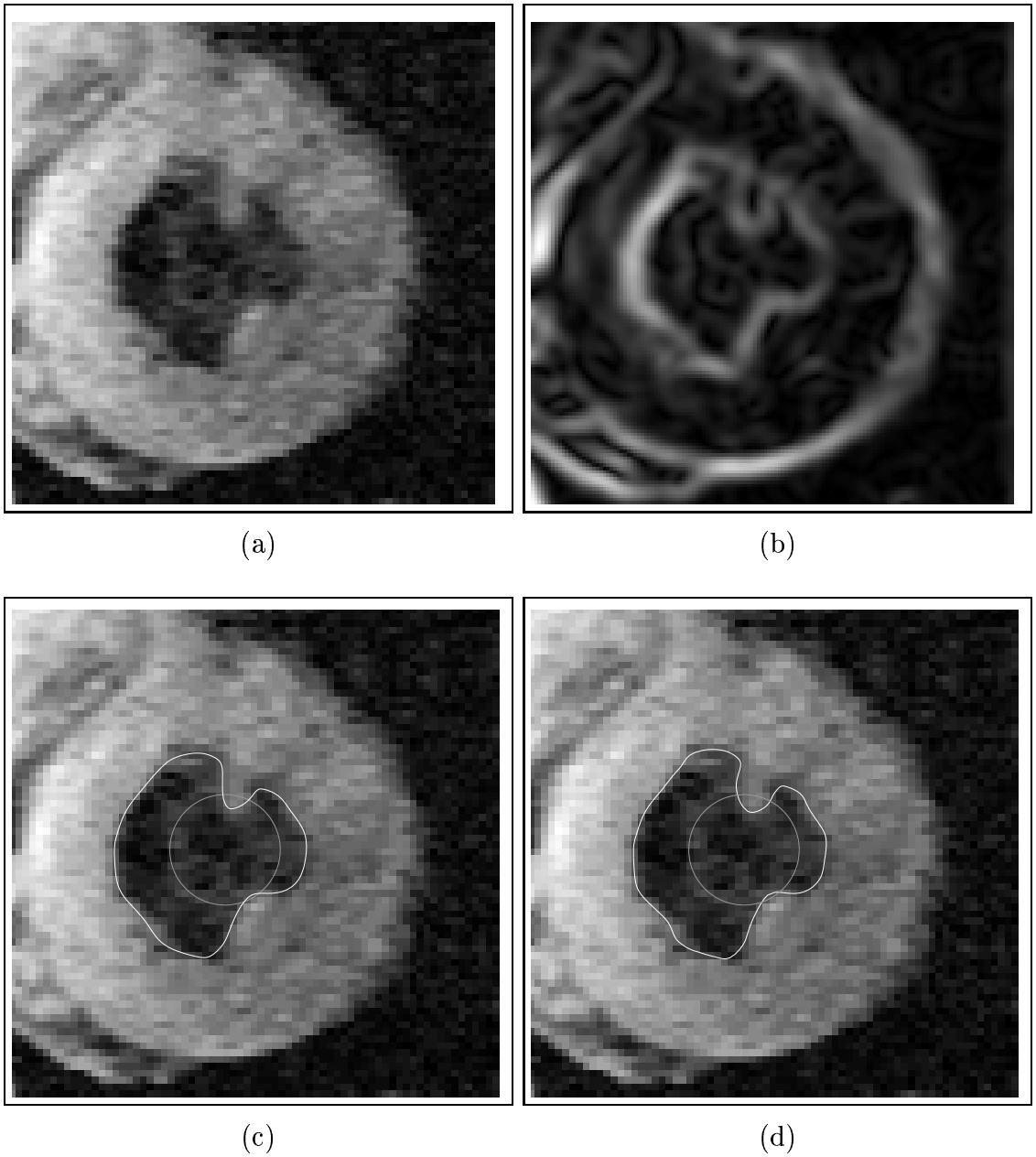

Figure 4.6: (a) A 160×160-pixel magnetic resonance image of the left ventrical of a human heart; (b) the edge map $|\nabla(G_\sigma(x,y) * I(x,y))|^2$ with $\sigma = 2.5$; (c) the result of GVF deformable contour with $\mu = 0.1$; and (d) the result of GGVF deformable contour with $\kappa = 0.15$. The parameters used for both deformable contours are $\alpha = 0.1$ and $\beta = 0$.

To see how medialness is contained in GGVF fields, we computed GGVF fields for four objects with different shapes as shown in Fig. 4.7. One can see that each GGVF field reveals a common trait at the center of each object. In particular, in each figure there is a single point or collection of points at which the GGVF vectors go to zero. This is caused by the inherent "competition" in the GGVF formulation, in which vectors that are "trying" to point toward an edge (because of the diffusion process) are balanced between edges. We further demonstrate this phenomenon by computing the GGVF for the eight shapes shown in Fig. 4.8 and displaying their magnitudes. Inside each of these shapes, the GGVF magnitude, which we denote by mag(GGVF) $= |\mathbf{v}(x, y)|$, appears to diminish along the set of points comprising the classical medial axis skeleton of the shape (cf. [9]). However, it is also apparent that mag(GGVF) does not necessary go to zero on this set. In particular, for the square shown in Fig. 4.8b, the medial axis skeleton is the set of points running diagonally between opposing corners, forming an "X". There is evidence of this "X" pattern in this figure, but mag(GVF) is clearly not zero on the arms of "X".

On the other hand, each of the simpler objects in Fig. 4.8 appears to have a single point in its interior at which mag(GVF) is minimum — a kind of *shape origin*. The more complicated shapes in Figs. 4.8f–h violate this principle because they involve multiple parts. It seems reasonable to conjecture that local minima of mag(GVF) represent shape origins of the "parts" comprising a shape.

Since mag(GGVF) is grayscale, not binary, we could think of it as giving a measure of how close a point is to the central axis of the shape. In this sense, mag(GGVF) could be used to give a measure of "medialness" in the sense of cores. Since medialness is normally larger when near the shape median rather than small, two possible measures of medialness are

$$\begin{aligned} \mathcal{M}^1(x, y) &= \frac{1}{1 + |\mathbf{v}(x, y)|^q}, \quad \text{and} \\ \mathcal{M}^2(x, y) &= e^{-\frac{|\mathbf{v}(x,y)|}{\tau}} \end{aligned}$$

Fig. 4.9 shows an example of the first medialness measure applied to the "teardrop" shape of Fig. 4.8d. One can see from this figure that the medialness is larger at two

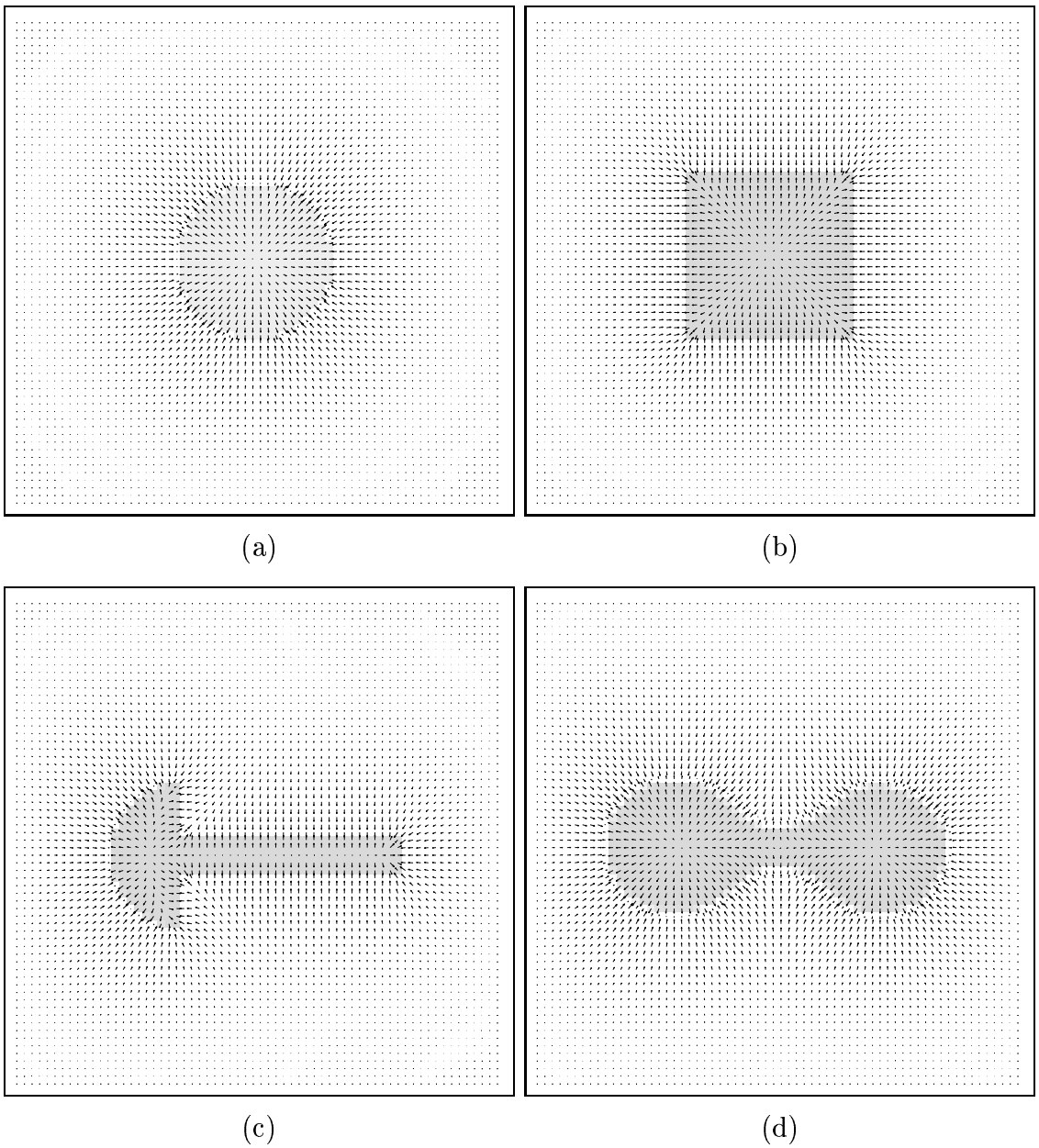

Figure 4.7: GGVF fields computed from objects with various shapes.

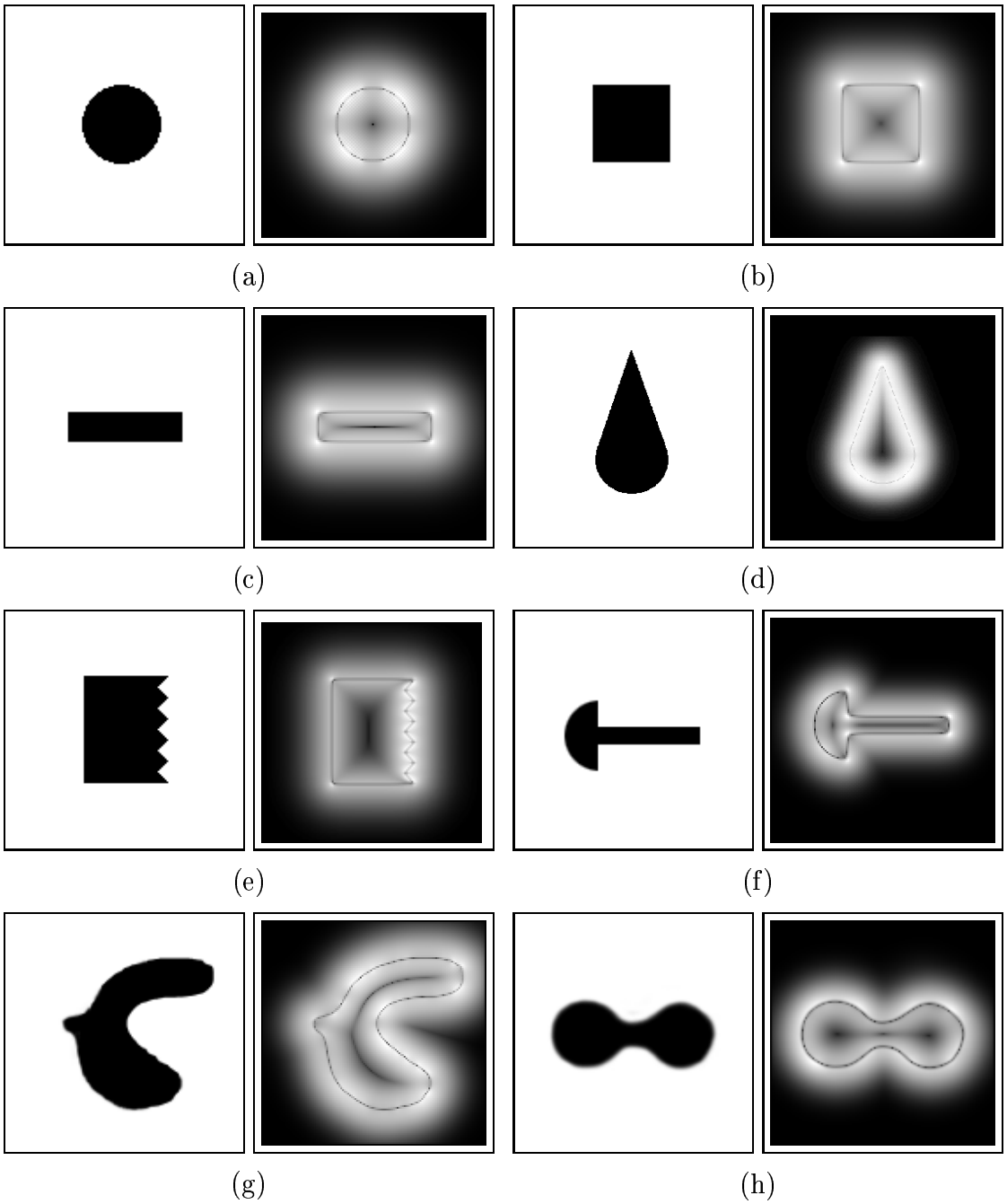

Figure 4.8: The magnitude of the GVF field gives information about the medial axis of a shape.

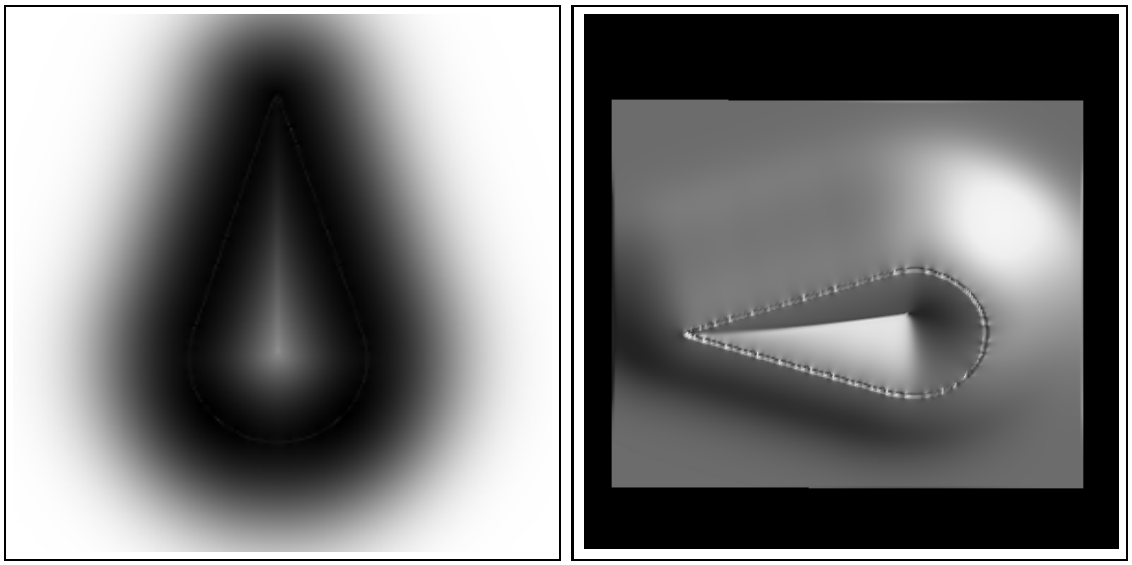

(a) (b)

Figure 4.9: The medialness map $\mathcal{M}^1(x, y)$ ($q = 0.05$) of a teardrop shape, shown as (a) a gray-level image and (b) a surface plot.

other locations besides the skeleton, namely the object boundary and far outside the object. It makes sense that medialness should be larger on the boundary since the relevant shape near the boundary is the boundary itself. This observation will prove to be useful in the next section where boundaries of certain thickness are concerned. Also, as one moves farther away from the shape, the shape itself becomes irrelevant, and every point should be medial. Therefore, it appears that the use of mag(GGVF) has very strong potential use in shape analysis using medial axis ideas and in particular to the concept of medialness in cores.

4.4 GGVF and the Central Layer of Thick Boundaries

The previous discussion on boundary mapping implicitly assumes boundaries in images have negligible thickness. Boundaries of certain thickness, however, may also occur either naturally in images such as the cortex of a brain or as a result of certain

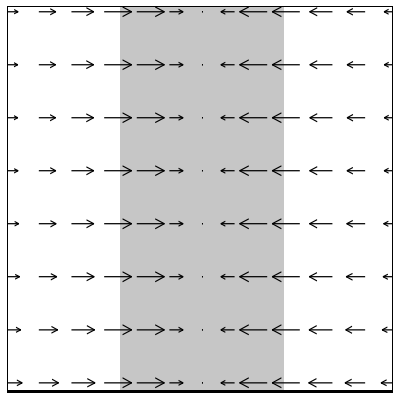

Figure 4.10: GGVF vector field converges to the center of a thick edge.

boundary detection operations [28]. A natural way to represent such a thick boundary is by reconstructing a curve or surface representation of its geometric central layer [28]. For example, Davatzikos and Prince have extracted central layers using deformable models with a novel external force defined as the displacement from a deformable model point to the center of image mass of a circular disk around this point [33]. One limitation of this method is that boundaries with different thicknesses require disks with different radii, prior knowledge that is not usually available.

Here, we show that it is possible use a GGVF deformable model to find central layers accurately without any prior knowledge of the boundary thickness. As was shown in the previous section, medialness defined through GGVF is larger on the boundary. This observation can be made more precise by considering boundaries with certain thickness. Fig. 4.10 shows an example of GGVF applied to a thick boundary. One can see from this figure that gradients at each side of the thick boundary are diffused by GGVF towards the center layer of the thick boundary. The vectors goes to zero at the center where the diffusion of gradients from both sides are balanced. The GGVF diffusion process will lead GGVF vectors to converge to the center regardless of the boundary thickness. This observation indicates that GGVF deformable models can be used to reconstruct the central layer of thick boundaries, as well as thin boundaries.

We demonstrate this property on simulated images (201×201) generated using

harmonic curves (Eq. (4.6)) corresponding to $m = 0, 4$, and 8 with thickness of 3, 6, and 9 pixels. Fig. 4.11 shows both the simulated images (in gray) and the reconstructed central layers (in black) using GGVF deformable contours ($\kappa = 0.05, \alpha = 0.1$, and $\beta = 0$). The maximum radial errors are computed for all the reconstructions. Fig. 4.12 shows the maximum radial errors for the central layer reconstruction of boundaries with different thickness as a function of harmonic curves' frequency m. We can make several observations from this plot. First, the overall maximum radial error is around $\frac{1}{2}$ pixel except when $m = 8$ and thickness is 9 pixels where the error is slightly larger than a pixel. Second, the errors increase as the boundary become more convoluted. Further study to characterize the relationship among accuracy, curvature, and thickness is warranted. Our primary interest in thick boundaries is motivated by reconstructing the brain cortex with typical thickness range from 3 to 5 voxels. In this application, GGVF deformable models are expected to work well. In Chapter 5, we have a detailed error study on GGVF application to cortex reconstruction from real MR brain images.

4.5 Variational Framework for Generalizing GVF

GVF can also be generalized by starting from its variational formulation Eq. (3.11) introduced in Chapter 3. Spatially-varying weighting functions can be used, leading to the following new variational formulation

$$\mathcal{E} = \int g(|\nabla f|)|\nabla \mathbf{v}|^2 + h(|\nabla f|)|\mathbf{v} - \nabla f|^2 d\mathbf{x}$$

where $|\cdot|$ is a vector norm and $\nabla \mathbf{v}$ is a second-order tensor. Using the calculus of variations, we obtain the following Euler equation

$$\nabla \cdot [g(|\nabla f|)\nabla \mathbf{v}] - h(|\nabla f|)(\mathbf{v} - \nabla f) = \mathbf{0}$$

The solution of this vector equation can be obtained by computing the steady state solution of the following generalized diffusion equation

$$\mathbf{v}_t = \nabla \cdot [g(|\nabla f|)\nabla \mathbf{v}] - h(|\nabla f|)(\mathbf{v} - \nabla f)$$

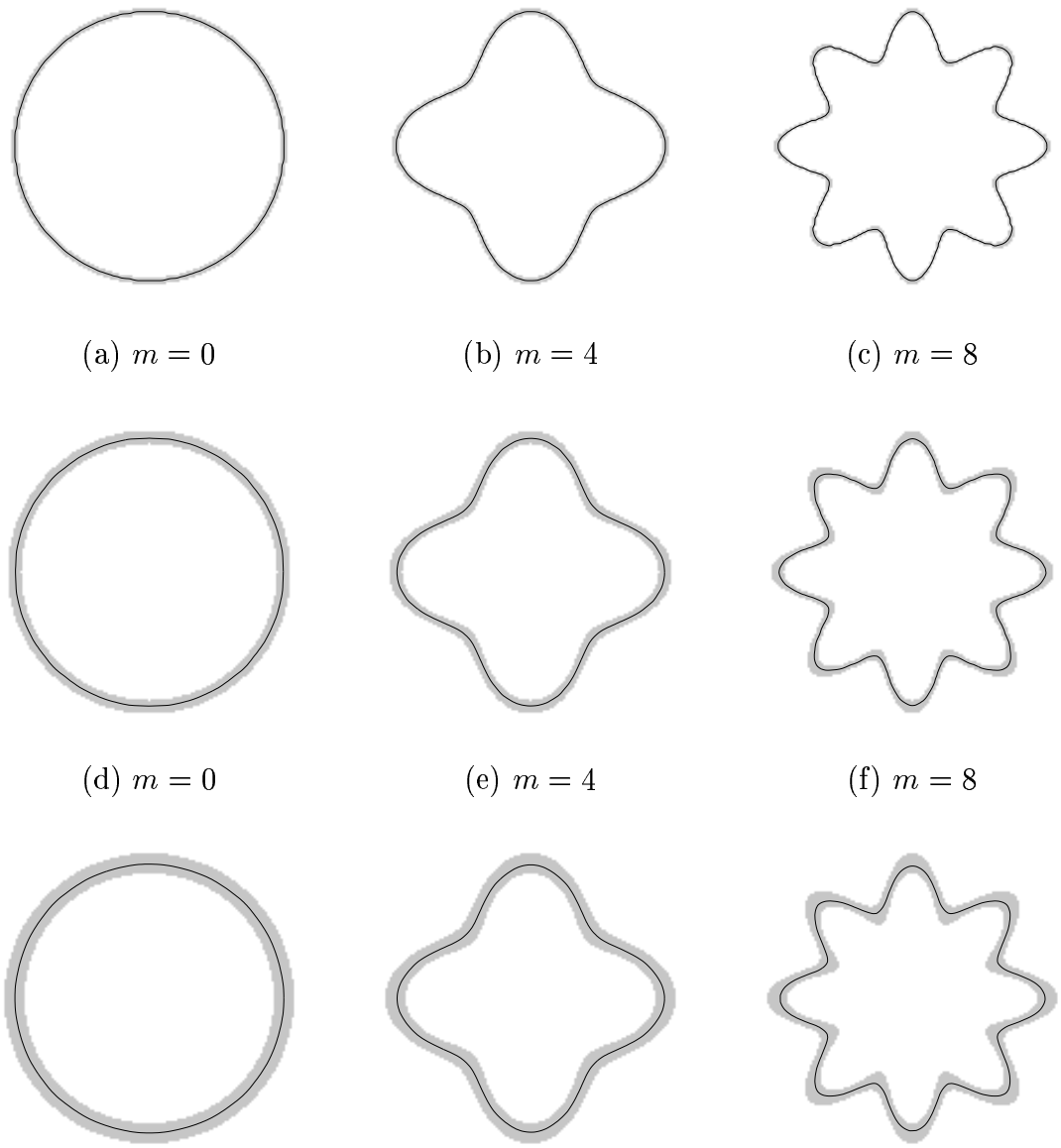

(a) $m = 0$ (b) $m = 4$ (c) $m = 8$

(d) $m = 0$ (e) $m = 4$ (f) $m = 8$

(g) $m = 0$ (h) $m = 4$ (i) $m = 8$

Figure 4.11: GGVF deformable contour results from simulated images with boundary thickness equal to 3 pixels (a)-(c), 6 pixels (d)-(f), and 9 pixels (g)-(i).

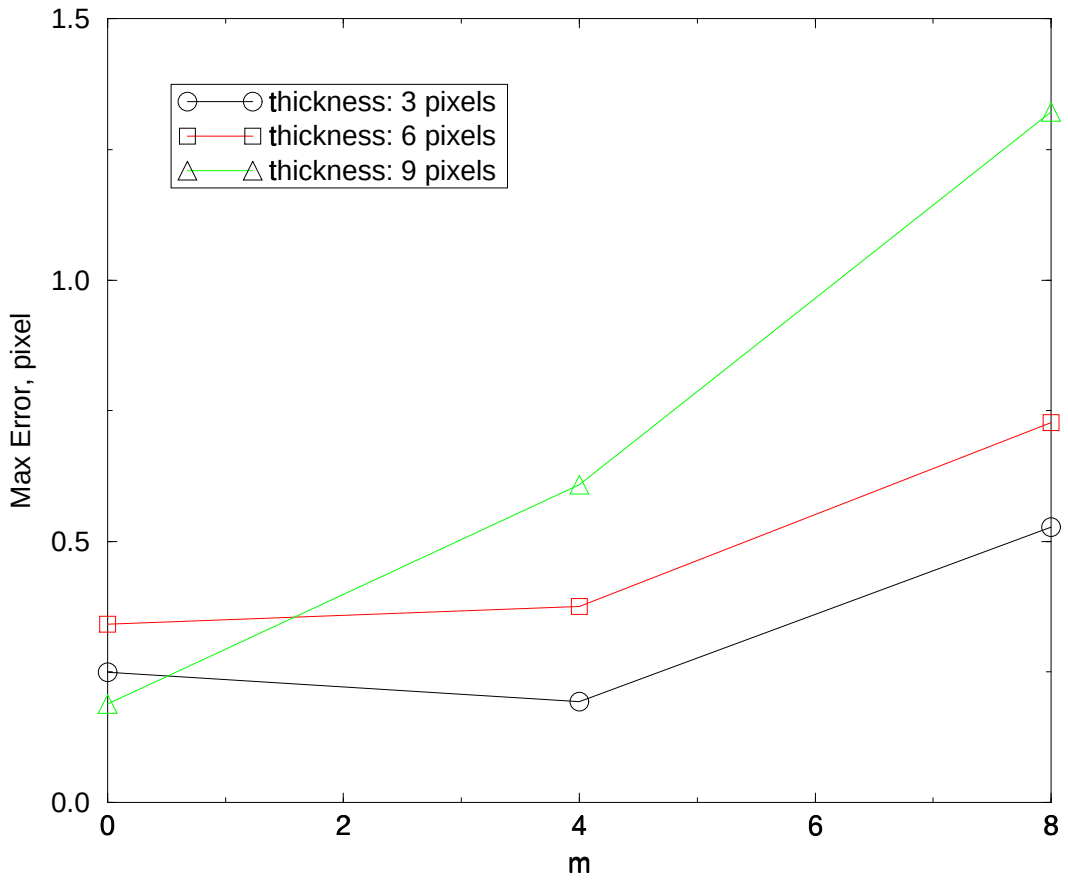

Figure 4.12: Maximum radial error for thick boundaries (MRE).

or written more explicitly

$$\mathbf{v}_t = \nabla g(|\nabla f|) \cdot \nabla \mathbf{v} + g(|\nabla f|)\nabla^2 \mathbf{v} - h(|\nabla f|)(\mathbf{v} - \nabla f)$$

This result is different than GGVF. To understand the nature of the difference, we note that if $\nabla g(|\nabla f|) \cdot \nabla \mathbf{v} = \mathbf{0}$, we get GGVF. This condition is data-dependent, however, and is satisfied in homogeneous regions, but is generally non-zero near the edges. We have implemented this generalized GVF and found that it has very similar properties as GGVF and usually yields a very similar result. This version is more computationally demanding, however. Therefore, despite the aesthetically pleasing property that it satisfies a minimum principle, we advocate GGVF when a generalization to GVF is desired.

4.6 Summary

We have presented a new class of external force models for deformable models. It is a generalization of the GVF formulation that includes two spatially-varying weighting functions. We showed that GGVF improves deformable model convergence into long, thin boundary indentations and maintains other desirable properties of GVF such as an extended capture range. We also showed that GGVF has excellent performance on noisy and real medical images. In addition, the GGVF field was shown to have potential applications in shape analysis, as well. The magnitude of the field was shown to have information related to a shape's medial axis, and to the scale space concept of medialness in the theory of cores. We have also shown that GGVF deformable models can be used to reconstruct the central layers of thick boundaries. Finally, we described an alternative approach to generalize the GVF by starting from its variational formulation.

Chapter 5

Human Cerebral Cortex Reconstruction from MR Images

In this chapter, we describe a systematic method for obtaining a parametric surface representation of the central layer of the human cerebral cortex. The core component of this method consists of an enhancement to the GGVF deformable models developed in Chapter 4 by incorporating prior knowledge about brain anatomy. This method also features a novel procedure to initialize deformable surfaces using an isosurface algorithm. The deformable surface model is applied on membership functions computed by an adaptive fuzzy segmentation rather than on image intensity volumes. The resulting method is a largely automated method that reconstructs the entire central cortical layer including deep convoluted sulci and gyri, while maintaining the correct surface topology. Because of incorporating adaptive fuzzy segmentation in the method, the method is robust to the partial volume averaging effects, image intensity inhomogeneities, and raw image intensity variation across subjects.

This chapter is organized as follows. In Section 5.1, we describe our new cortical surface reconstruction method. In Section 5.2, we present and discuss both qualitative and quantitative results of applying our method to six different subjects as well as a simulated MR brain volume. In Section 5.3, we present some preliminary results on brain geometry analysis. Finally, in Section 5.4, we summarize the results of this chapter.

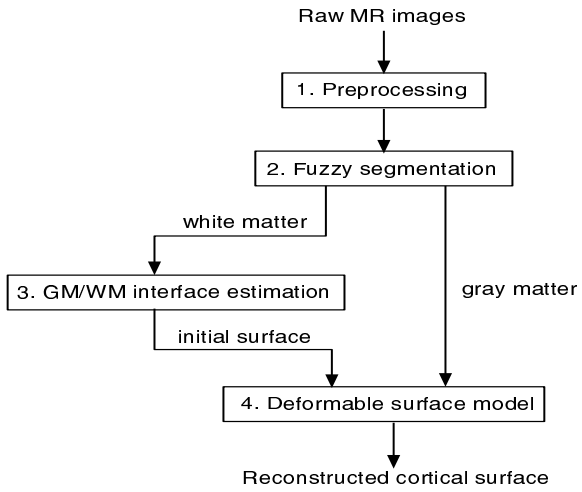

Figure 5.1: Block diagram of the overall cortical surface reconstruction system.

5.1 Methods

In this section, we present our method for reconstruction of the cortical surface from MR brain image data. This method consists of four major steps. First, the acquired data is preprocessed to extract the cerebrum and interpolated to cubic voxels. Second, the brain image volume is segmented into fuzzy membership functions of GM, WM, and CSF tissue classes using an adaptive segmentation algorithm that is robust to image intensity inhomogeneities. Third, an iterative process of median filtering and isosurface generation on the WM membership function produces an initial estimate of the cortical surface that is topologically correct. Fourth, our deformable surface algorithm moves this surface toward the central layer of the cortex yielding the final reconstructed cortical surface. Fig. 5.1 shows an overall flow diagram of our method. Throughout this section, we use results from one subject as an example to illustrate the method.

5.1.1 Data Acquisition and Preprocessing

Our algorithm uses T1-weighted volumetric MR image data with voxel size on the order of 1 mm^3. This data provides adequate contrast between gray matter, white

matter, and cerebrospinal fluid in a single intensity parameter, and has fine enough resolution to resolve the complex structure of the cortex. It has been tested on both axially acquired image data with in-plane resolution of 0.9375×0.9375 mm and out-of-plane resolution of 1.5 mm and on coronal data with comparable resolution figures. The algorithm is easily modified to use multi-spectral data, but the resolution must be the same or better.

The first step in our method is to preprocess the image volume to remove skin, bone, fat, and other non-cerebral tissue. We used a semi-automated software package developed by Christos Davatzikos and Jerry Miller at Johns Hopkins University [46]. This package features a combination of region growing algorithms and mathematical morphology operators to ease the processing of cerebral tissue extraction. It also provides some manual editing features that were used to remove the cerebellum and brain stem (since we are only interested in the cerebral cortex). We note that further automation may be possible using the methods proposed in [94, 61, 67], but in our experience some manual intervention was always required even with these approaches. Fig. 5.3 shows the three slices from Fig. 5.2 after this procedure was applied.

The final step in preprocessing is to trilinearly interpolate the segmented volume to cubic voxels having the in-plane resolution in all three directions. This reduces the directional dependency in subsequent processing.

5.1.2 Fuzzy Segmentation of GM, WM and CSF

There has been a trend in the recent literature favoring the use of fuzzy segmentations over hard segmentations in defining anatomical structures [13]. Fuzzy segmentations retain more information from the original image than hard segmentations by taking into account the possibility that more than one tissue class may be present in a single voxel. This circumstance often occurs when imaging very fine structures, resulting in partial volume averaging. Small errors in the data acquisition or segmentation will also be less of a factor in fuzzy segmentations since this will only alter the segmentation by some fractional number while in a hard segmentation, small errors might change the entire classification of a voxel.

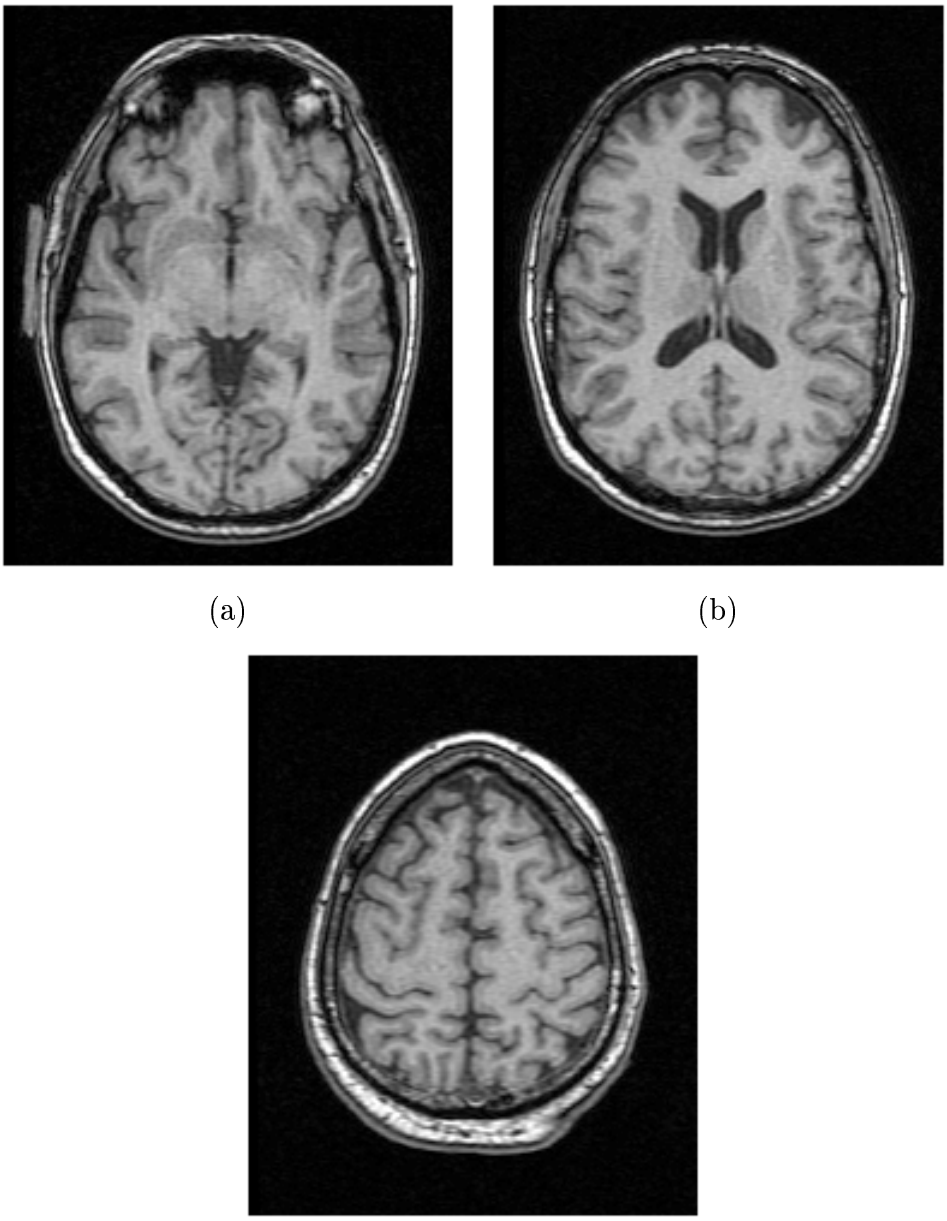

(a) (b)

(c)

Figure 5.2: Sample slices from acquired MRI data set.

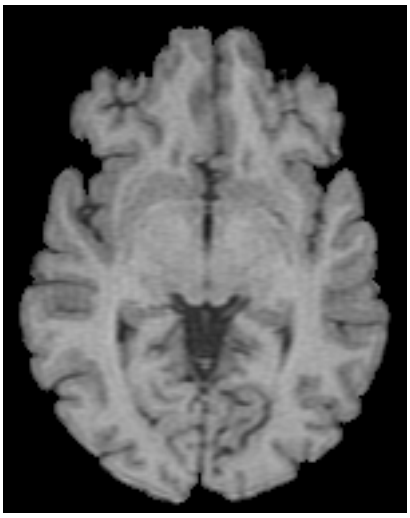

(a)

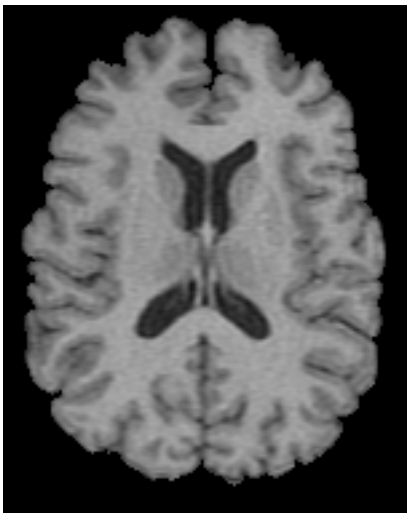

(b)

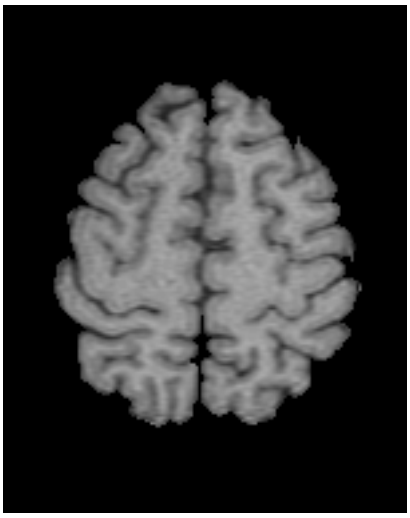

(c)

Figure 5.3: Sample slices after the cerebral tissue extraction.

MR images sometimes suffer from intensity inhomogeneities caused predominantly by nonuniformities in the RF field during acquisition [23, 35]. The result is a slowly-varying shading artifact appearing across images that can produce errors in intensity-based segmentation methods. In particular, this artifact may cause the position of the reconstructed cortex in various regions of the brain to be shifted slightly from its true position. Robustness to intensity inhomogeneities is therefore an important requirement in a cortical surface reconstruction algorithm.

Recently, Pham and Prince reported a new method called adaptive fuzzy c-means (AFCM) [84, 85, 86] to obtain fuzzy segmentations of MR images that are robust to intensity inhomogeneities. AFCM iteratively estimates the fuzzy membership functions for each tissue class, the mean intensities (called *centroids*) of each class, and the inhomogeneity of the image, modeled as a smoothly varying gain field. The fuzzy membership functions, constrained to be between zero and one, reflect the degree of similarity between the observed voxel intensity and the centroid of that tissue class. A typical result from AFCM is shown in Fig. 5.4.

5.1.3 Estimation of Initial Surface with the Correct Topology

In order to use a deformable surface model to accurately reconstruct the extremely convoluted cortical surface, a good initial surface is required. In the past, deformable surfaces have been typically initialized using simple geometric objects (e.g., a sphere or ellipsoid) outside the cortical surface or by manual interaction [72, 94, 42, 31]. When initialized from outside the cortical surface, however, deformable surfaces have difficulty progressing into the sulci [31]. As shown in Fig. 5.5, the primary difficulty with this approach is that sulci can be narrow relative to the resolution of the scanner, so the imaged sulci become connected [74]. As a result, these deformable surfaces produce cortical surface reconstructions that lack deep folds. Manual initializations yield better results but they are labor intensive and time consuming for 3-D data sets.

Because of the presence of WM, there is more space between the cortical folds on the inside of the cortex than there is on the outside (see Fig. 5.5). Therefore,

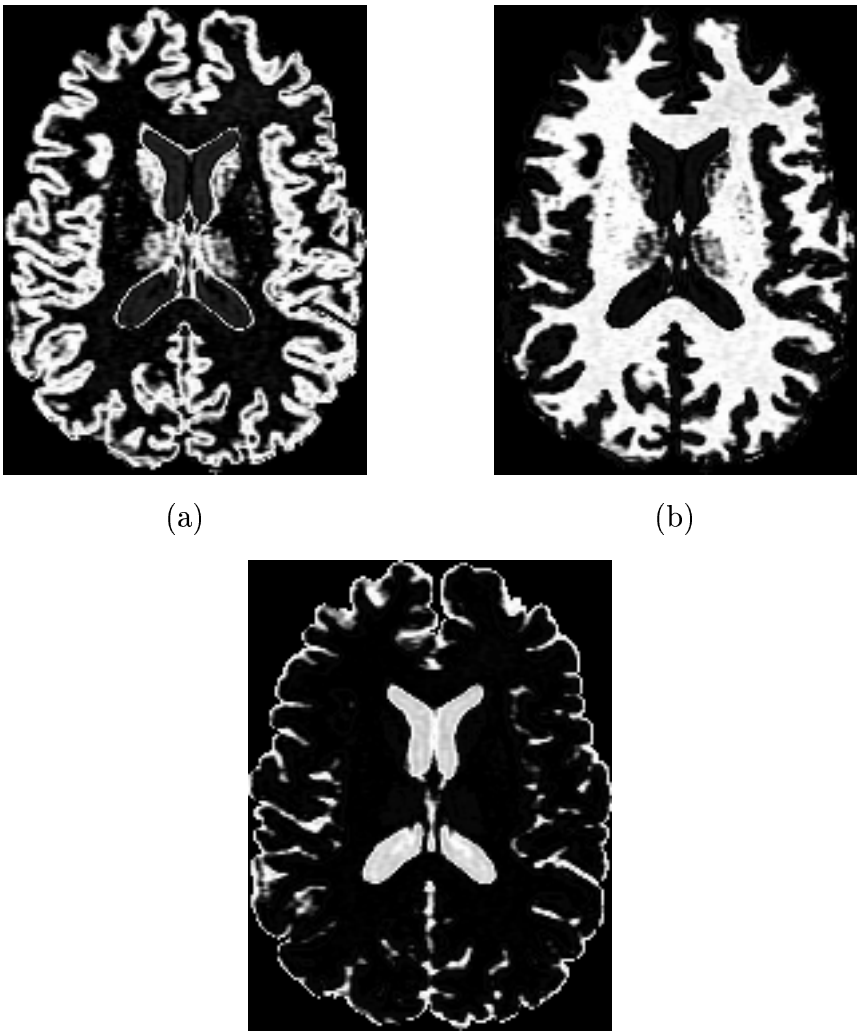

Figure 5.4: Sample slice from membership functions computed using AFCM. (a) GM, (b) WM, and (c) CSF.

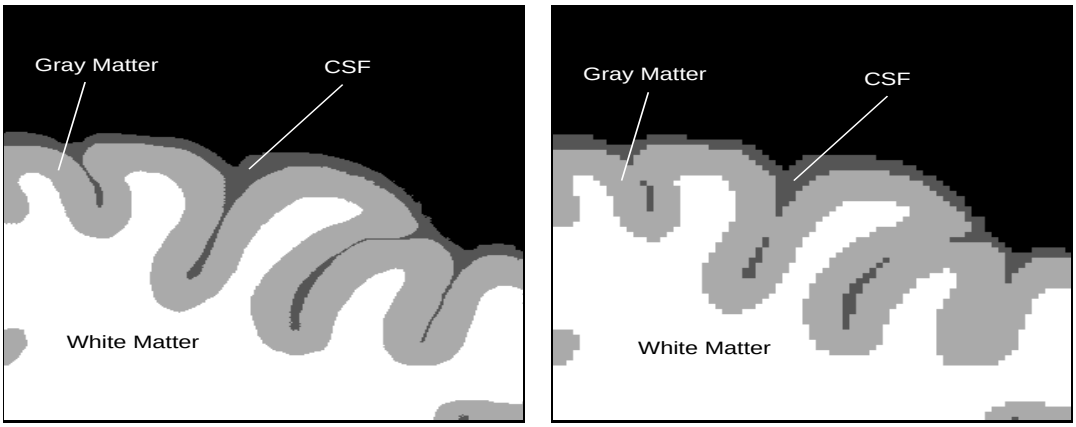

(a) (b)

Figure 5.5: Resolution problems in determining the cortical surface. (a) ideal image, and (b) sampled image.

initializing the deformable surface on the inside of the cortex is a promising strategy [27, 118, 104]. Ideally, we desire an initial surface that is on the inside of the cortex, is close to the final surface, and has the correct topology — that of a sphere. As shown in Fig. 5.5, the GM-WM interface is both inside and close to the cortex. Accordingly, our approach is to find a surface that approximates the GM-WM interface by finding an isosurface of a filtered WM membership function. Filtering is required in order to make the initial surface have the correct topology. We now describe this approach in detail.

Using an Isosurface Algorithm

An *isosurface* is a surface that passes through all locations in space where a continuous data volume is equal to a constant value. The construction of isosurfaces is a well-studied problem [71, 79, 60]. The result of a typical isosurface algorithm usually consists of a set of triangle meshes that are discrete representations of the corresponding continuous isosurfaces.

Since voxels at the GM-WM interface contain both GM and WM, an isosurface can be computed on the WM membership function obtained from AFCM to yield an estimate of the GM-WM interface. In order to use isosurfaces in the context of our

work, several issues need to be addressed:

- *Extraneous connected structures*

  The boundaries of the hippocampus, the ventricles, and the putamen are generally connected with the cortical GM-WM interface in the WM membership function. This may cause isosurfaces computed from the WM membership function to be a composite of the cortical GM-WM interface and these extraneous connected surfaces. Since we are only interested in reconstructing the cortical GM-WM interface, we manually remove the hippocampal formation and fill both the ventricles and the putamen in the WM membership function. This process is facilitated with the aid of region growing algorithms and takes only a small portion of the total processing time.

- *Mesh selection*

  The output from an isosurface algorithm on the WM membership function usually contains multiple meshes. Since these meshes are physically disconnected from each other, they can be distinguished from one another by their vertex connectivity. Among all these meshes, the one with the largest number of vertices corresponds to the GM-WM interface.

- *Topology*

  Isosurfaces are, in general, topologically unconstrained. We assume that the topology of GM-WM interface is equivalent to that of a sphere. However, imaging noise often induces the formation of small handles (like that of a coffee cup) on the computed WM isosurface. These small handles are inconsistent with the assumed anatomical topology and special care is required in order to obtain an initial surface with the correct topology.

Correcting Surface Topology

The existence of handles in a surface can be detected by computing the surface's *Euler characteristic*, χ [111]. For a closed surface, χ can only assume an integer value

less than or equal to 2. A surface is topologically equivalent to a sphere when $\chi = 2$. The existence of handles in the surface reduces the value of χ by 2 for each handle.

The Euler characteristic can be computed from a triangulation of the surface by [2]

$$\chi = V - E + F, \tag{5.1}$$

where V is the number of vertices, E is the number of the edges, and F is the number of faces. The Euler characteristic is a topological invariant of a surface and does not depend on the method of triangulation.

We found that the handles on the surface can be eliminated by successively median filtering the WM membership function and recomputing its isosurface until the largest isosurface triangle mesh has $\chi = 2$. The resulting surface is close to the GM-WM interface and has the topology of a sphere.

Summary of Surface Initialization

Based on the preceding observations, our procedure for computing an initial estimate of the cortical surface with the correct topology can be summarized as follows:

1. Manually remove the hippocampal formation and fill both the ventricles and the putamen in the WM membership function.

2. Compute an isosurface on the preprocessed WM membership function at the value 0.5.

3. Extract only the connected surface with the largest number of vertices.

4. Compute the Euler characteristic χ of the extracted surface.

5. If χ is not equal to 2, then apply a $3 \times 3 \times 3$ median filter to the preprocessed WM membership function, recompute the isosurface on the filtered data, and go to Step 3.

Isosurfaces were generated using the IBM Visualization Data Explorer software which uses the ALLIGATOR algorithm [60].[7] We note that we have recently used another

[7] This implementation of the ALLIGATOR algorithm sometimes results in isosurfaces that contain singular points where two different parts of the mesh meet at one vertex, which ALLIGATOR should

Table 5.1: Size and Euler characteristics of meshes from the original isosurface calculation.

# of vertices	χ	*# of meshes*
360,104	-1010	1
506	-6	1
250 – 499	2	1
100 – 249	2	11
50 – 99	2	28
25 – 49	2	97
6 – 24	2	1970

Table 5.2: Euler characteristic of largest resulting surface after each iteration.

# of iterations	χ
0	-1010
1	-56
2	-14
3	-4
4 – 7	-2
8	0
9	2

isosurface algorithm from Visualization Toolkit software [97] and obtained identical results. Except for Step 1, all of the steps are performed automatically.

A typical result of applying the above procedure to one of our data sets is shown in Tables 5.1 and 5.2, and Fig. 5.6. Table 5.1 shows the number of meshes and their χ values before any median filtering has taken place. The one mesh that is clearly much larger than all other meshes represents an estimate of the GM-WM interface with an incorrect topology. Table 5.2 shows how the χ of the largest resulting mesh is increasing with each iteration and eventually converges to the desired value of 2. Although there is no theoretical proof that successive median filtering will cause the Euler characteristic to converge to 2, we have found empirically that this is the case. Experimental results on the convergence of the deformable surface initialization are provided in Section 5.2.2.

Fig. 5.6a shows the result of the isosurface algorithm on the original WM membership function at a value of 0.5. Multiple meshes and topological inconsistencies are present. Fig. 5.6b shows the final, topologically correct mesh after nine iterations of our procedure. We see that although we have not yet applied the deformable surface model, many of the prominent geometrical characteristics of this cortical surface are already apparent.

prohibit. In this case, methods to remove singular points were also incorporated into the iterative procedure.

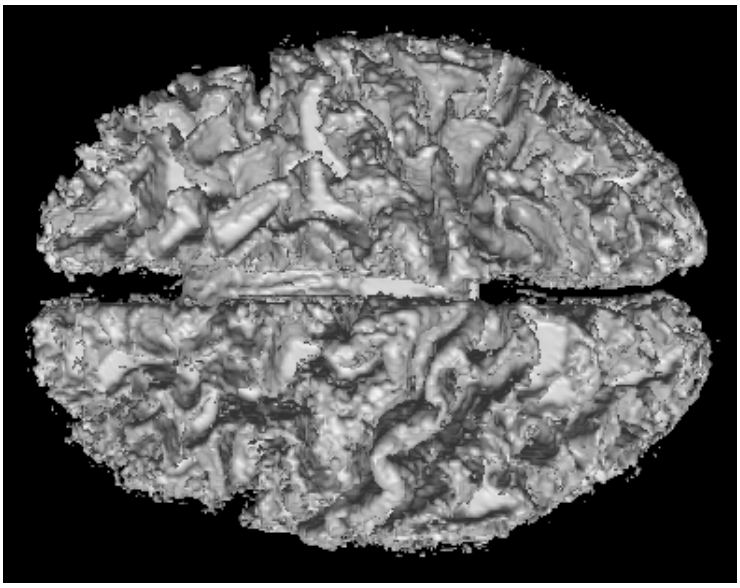

(a)

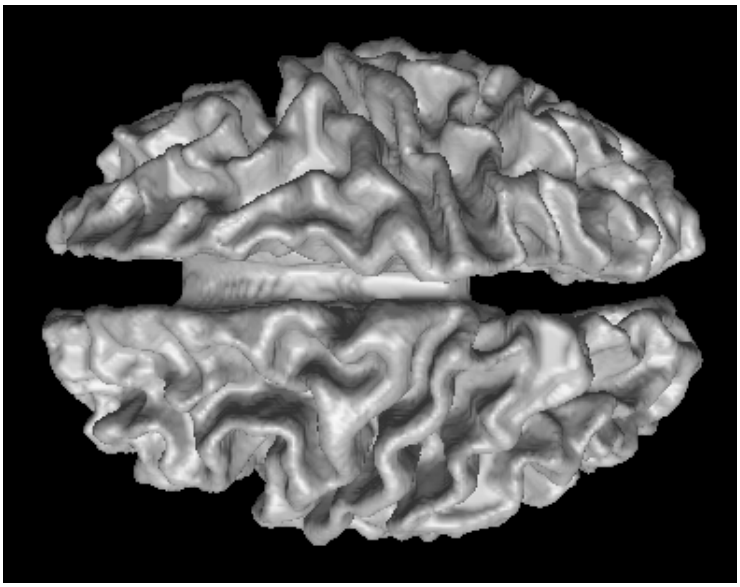

(b)

Figure 5.6: (a) Isosurface of WM membership function with the incorrect topology, (b) estimated initial surface with the correct topology.

5.1.4 Refinement of the Initial Surface Using a Deformable Surface Model

After obtaining an initial estimate of the cortical surface that is topologically correct, the surface requires refinement. Because of median filtering, the initial surface in the previous step is a smoothed version of the GM-WM interface. Using deformable surfaces, it is possible to have this initial surface move toward the central layer of the GM. The main problem here lies in defining the external forces. Below, we first give a brief discussion on external forces and then describe our specific model, which uses external forces that push the initial surface toward the central layer of the GM.

External Forces

In Chapter 4, we showed that GGVF deformable models can be used to reconstruct the central layer of thick boundaries. This property is ideally suited for our task since the cortex appears in the images as thick boundaries. However, because of the extremely convoluted and complex shape of the human brain cortex, GGVF deformable surface convergence can be slow and the surface still may not fully capture the gyri in some areas of the brain. Thus, we combine GGVF with pressure forces [20, 21] that are constrained to operate only on parts of the surface that are outside GM. This constraint, similar to that in [61], helps increase the speed of convergence of the deformable surface when it is far from the GM and improves the fidelity of the final result when it is within the GM. The resulting external force is given by

$$\mathbf{F}_{\text{ext}}(\mathbf{x}) = k_1 \langle \mathbf{v}(\mathbf{x}), \mathbf{n}(\mathbf{x}) \rangle \mathbf{n}(\mathbf{x}) + k_2 C(\mathbf{x}) \mathbf{n}(\mathbf{x}) \tag{5.2}$$

where k_1 and k_2 are weights, $\mathbf{v}(\mathbf{x})$ is the GGVF field, $\mathbf{n}(\mathbf{x})$ is the outward unit normal vector of the surface at $\mathbf{x}$, $\langle \cdot, \cdot \rangle$ is the inner product of two vectors, and $C(\mathbf{x})$ is a constraint field (defined below). Since the component of the external force in the tangent plane will affect the parameterization of the surface but not its shape, we project $\mathbf{v}(\mathbf{x})$ onto the normal direction at surface position $\mathbf{x}$. The internal force is therefore solely responsible for controlling the surface parameterization while the

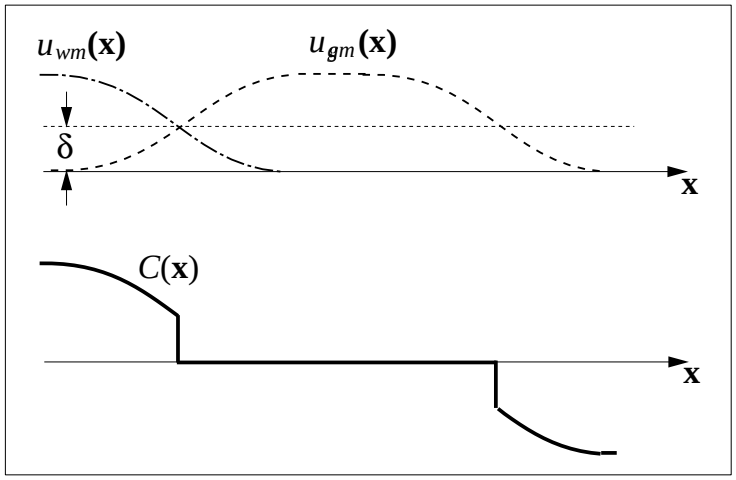

Figure 5.7: Illustration of behavior of $C(\mathbf{x})$.

external force is solely responsible for deforming the surface toward the feature of interest.

The constrained pressure force $C(\mathbf{x})\mathbf{n}(\mathbf{x})$ is designed to push the surface outward only until it enters the GM, whereupon the pressure force then turns off and GGVF completes the convergence. To accomplish this, we define the strength of the pressure force, as controlled by the constraint field $C(\mathbf{x})$, to be

$$C(\mathbf{x}) = \begin{cases} 0 & \text{if} \quad |2 * u_{wm}(\mathbf{x}) + u_{gm}(\mathbf{x}) - 1| < \delta \\ 2 * u_{wm}(\mathbf{x}) + u_{gm}(\mathbf{x}) - 1 & \text{otherwise} \end{cases}$$

where $u_{wm}(\mathbf{x})$ and $u_{gm}(\mathbf{x})$ are the WM and GM membership functions. Here, δ is a threshold that controls the width of the GM region where the pressure force is disabled, i.e. $C(\mathbf{x}) = 0$. In our experiments we used $\delta = 0.5$. The behavior of $C(\mathbf{x})$ is illustrated in Fig. 5.7 where one-dimensional profiles of GM and WM membership functions and the corresponding $C(\mathbf{x})$ are plotted. It is easy to see that when $\mathbf{x}$ is in the WM, $C(\mathbf{x})$ is positive, which causes the pressure force to push a deformable surface towards the GM. When $\mathbf{x}$ is in the GM, $C(\mathbf{x})$ is zero and the GGVF force is the only external force. When $\mathbf{x}$ is outside the GM in the CSF or background, $C(\mathbf{x})$ is negative, causing the pressure force to push the deformable surface back toward the GM.

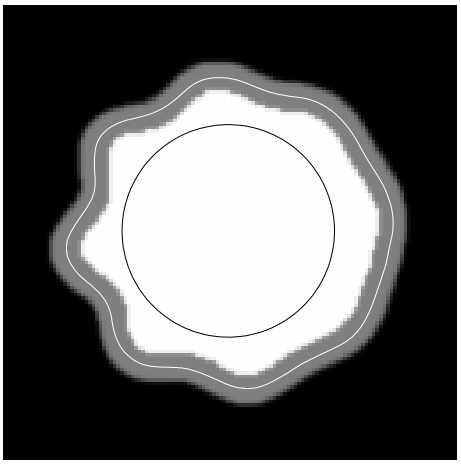

Figure 5.8: Initial deformable contour shown in black and final converged contour shown in white.

To demonstrate the behavior of these external forces, we applied a 2-D deformable contour, a 2-D analog to deformable surfaces in 3-D, using the external forces defined in Eq. (5.2) to the computer phantom shown in Fig. 5.8. Here, the gray ribbon is analogous to the cortical GM, sandwiched between the WM and the CSF. In the figure, the initial deformable contour is the circle shown in black, while the final converged contour is shown in white. We note that the final contour rests on the center of the simulated GM.

Adaptive Parameters

Because of image noise, relatively large internal forces are desirable where the deformable surface is far from the GM. Large internal forces cause the deformable surfaces to be very smooth, however, and prevent the surface from accurately conforming to the central cortical layer. Therefore, lower internal forces are desirable where the deformable surface lies within the GM. We achieve this by allowing α and β to be spatially varying parameters in Eq. (2.9) with respect to the strength of the

constraint field $C(\mathbf{x})$ as follows

$$\alpha(\mathbf{x}) = \begin{cases} \alpha & \text{if} \quad |C(\mathbf{x})| = 0 \\ \bar{\alpha} & \text{otherwise} \end{cases},$$

and

$$\beta(\mathbf{x}) = \begin{cases} \beta & \text{if} \quad |C(\mathbf{x})| = 0 \\ \bar{\beta} & \text{otherwise} \end{cases}$$

where $\bar{\alpha} \geq \alpha$ and $\bar{\beta} \geq \beta$.

5.1.5 Reconstructed Surface

As an example, we carried out the complete surface reconstruction on the sample data set appearing in Figs. 5.2, 5.3, 5.4, and 5.6. Different views of the reconstructed surface are shown in Fig. 5.9, and cross sectional views are shown in Fig. 5.10. The parameters used to achieve this result are $\lambda_1 = 2 \times 10^4$ and $\lambda_2 = 2 \times 10^5$ for AFCM; $\kappa = 0.2$ for GGVF; and $\alpha = 0.25$, $\beta = 0$, $\bar{\alpha} = 0.75$, $\bar{\beta} = 0$, $k_1 = 0.5$, and $k_2 = 0.01$ for the deformable surface. While this may appear to be a large number of parameters to tune, we have found that they are fairly robust to both changes in their values and the data. In fact, all the results presented in the following section use these same parameters.

At first glance, the sulci in the surface shown in Fig. 5.9 appear too open and do not resemble those from a normal brain. Note, however, that this reconstruction represents the *central layer* of the cortical GM, an object that we are not accustomed to viewing. The central layer is not the brain's outer surface such as what would be seen from a cadaver brain or a standard isosurface reconstruction of the cortical surface. Careful inspection reveals exquisite depiction of the major sulci including the central sulci, superior temporal sulci, calcarine sulci, parietal occipital sulci, and the Sylvian fissure. Secondary sulci such as the pre- and post- central sulci, the superior frontal sulci, and the cingulate sulci are also readily discernible. Their prominence in these pictures is to some extent because we are depicting a more open brain surface, but also because the central cortical layer is the most natural representation of the overall geometry of the cortex.

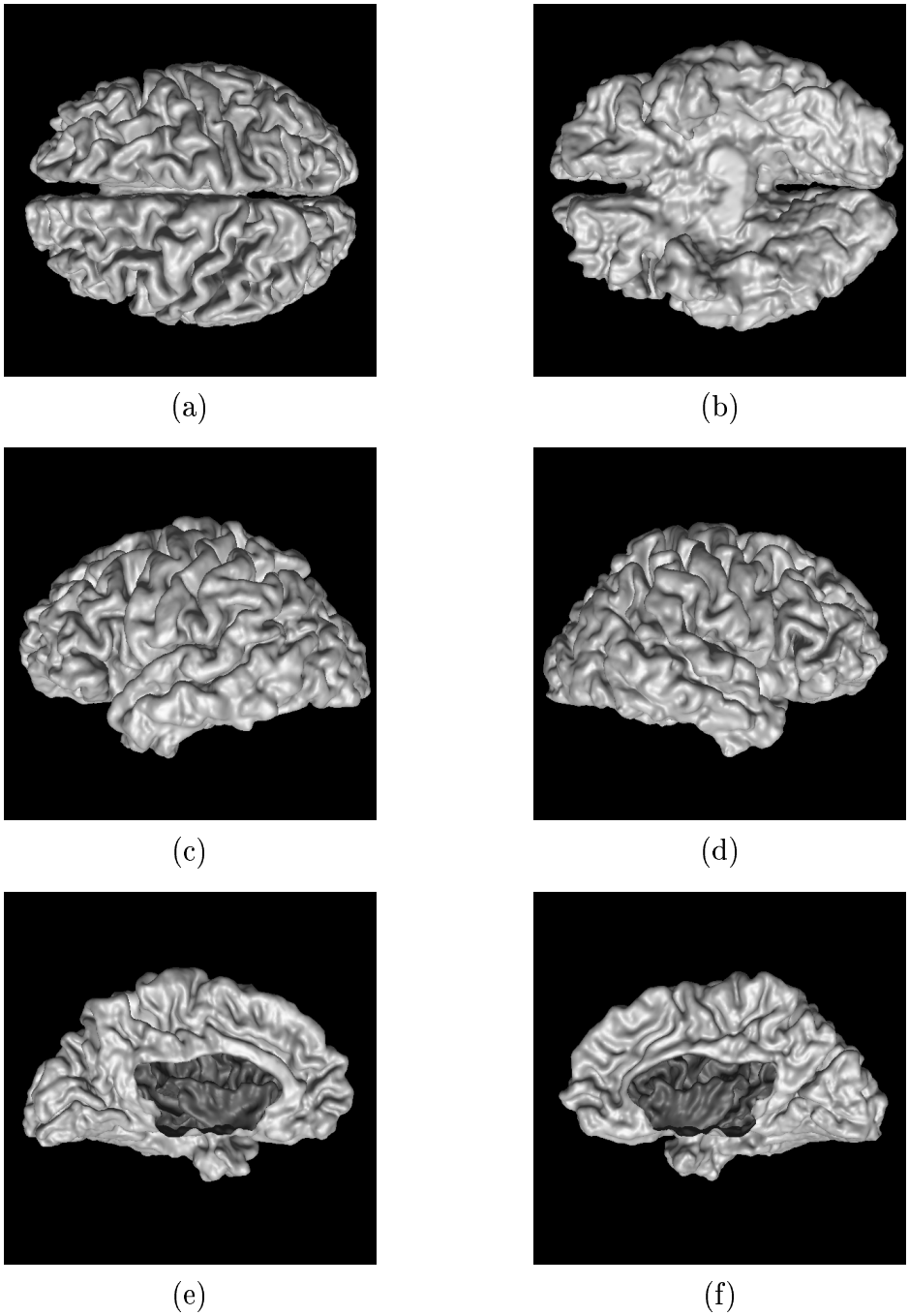

Figure 5.9: A surface rendering of reconstructed cortical surface from one subject displayed from multiple views: (a) top, (b) bottom, (c) left, (d) right, (e) left medial, and (f) right medial.

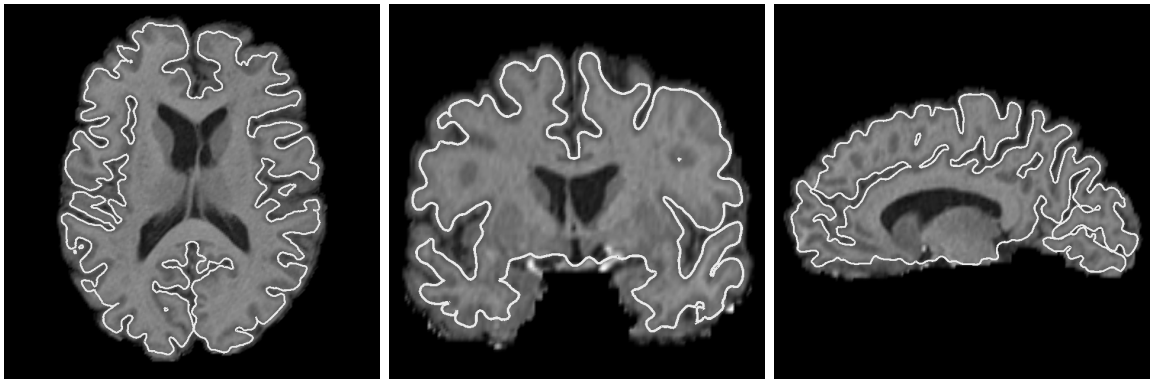

(a) (b) (c)

Figure 5.10: Cross sectional views of the reconstructed cortical surface: (a) axial, (b) coronal, and (c) sagittal.

The cross sectional pictures in Fig. 5.10 show how the reconstructed surface tracks the central cortical layer over the entire cortex, including its deepest folds. In fact, because the surface is initialized inside the cortex, the most difficult areas to reconstruct are typically the gyri, not the sulci. A typically difficult area is the superior temporal gyri, which is not particularly well-reconstructed on the left side of the picture in Fig. 5.10b. Other features of interest appearing on these cross-sections are the various "islands" of apparently disconnected surface intersections. These features are actually parts of the surface protruding through the image plane; the surface being portrayed is simply-connected with the topology of a sphere.

5.2 Results

We applied the described cortical surface reconstruction method to MR brain images from six subjects, four of which were taken from the Baltimore Longitudinal Study on Aging [99]. The same parameters used in the example from the previous section were used for these six studies. Using an SGI O2 workstation with a 174 MHz R10000 processor, the total processing time per study varied between 4.5 and 6 hours. The time required for manual interaction varied between 0.5 hours and 1 hour for a trained operator and AFCM required approximately 1 hour. The automated steps

in GM/WM interface estimation take about 0.5 hours and produce a mesh with between 200,000 and 400,000 vertices. Because of the large number of vertices in the mesh, it takes the deformable surface algorithm about 3 hours to produce the final reconstructed surface. Note that both AFCM and the deformable surface algorithm are fully automated steps.

5.2.1 Qualitative Results

Fig. 5.11 shows the right medial surface of each of the six reconstructed cortical surfaces. Prominent sulci include the calcarine fissure, the parieto-occipital sulcus, and the cingulate sulcus. Fig. 5.12 shows a coronal view of a slice taken approximately at the anterior commissure of each reconstructed cortical surface. These figures show that the surfaces reside on the central cortical layer and that buried gyri (such as the insula) are found. Although most gyri are properly depicted, certain regions, such as the superior temporal gyrus, are sometimes not found accurately. This is particularly apparent in Figs. 5.12e and 5.12f. We are considering further improvements to correct these deficiencies.

5.2.2 Quantitative Results

Several quantitative validation experiments were performed to evaluate the robustness and accuracy of our surface reconstruction approach. These are described in this section.

Initialization Algorithm Validation

Application of our method to multiple subjects allowed a preliminary validation of the convergence of the deformable surface initialization algorithm introduced in Section 5.1.3. The results are shown in Table 5.3, where we observe that the median filter used in the iterative process effectively eliminates handles on the surfaces, and that in all six cases the Euler characteristic of the surface converged to 2 in fewer than 10 iterations.

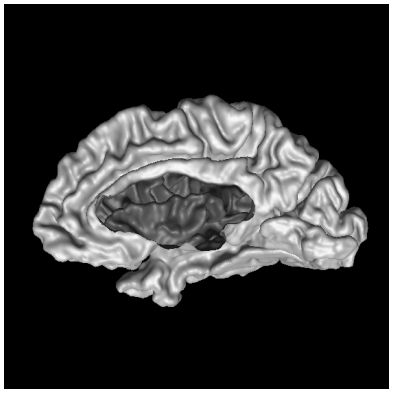

(a) Subject 1

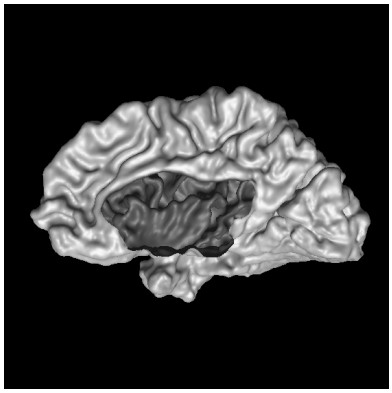

(b) Subject 2

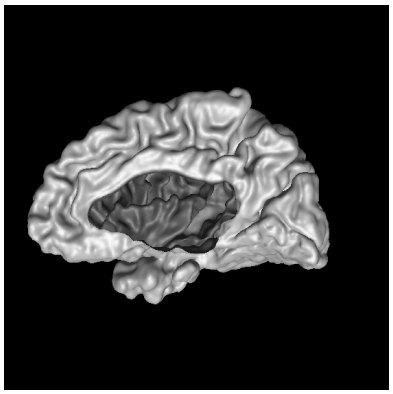

(c) Subject 3

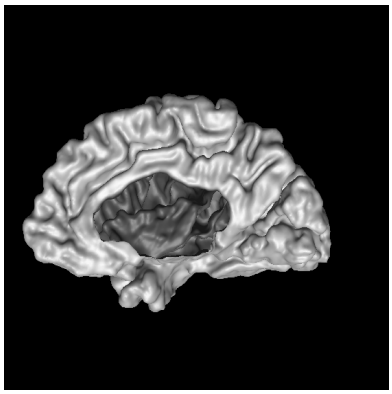

(d) Subject 4

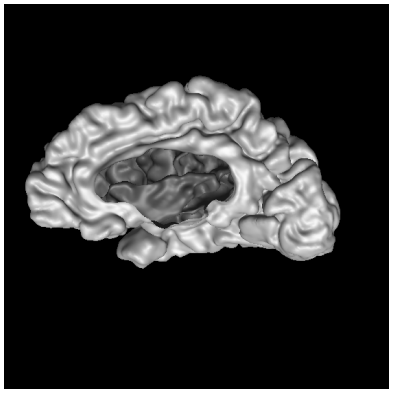

(e) Subject 5

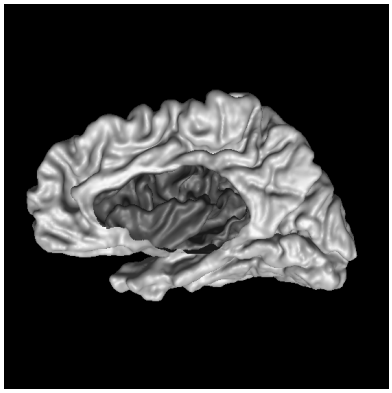

(f) Subject 6

Figure 5.11: Medial view of surface rendering of all six reconstructed cortical surface.

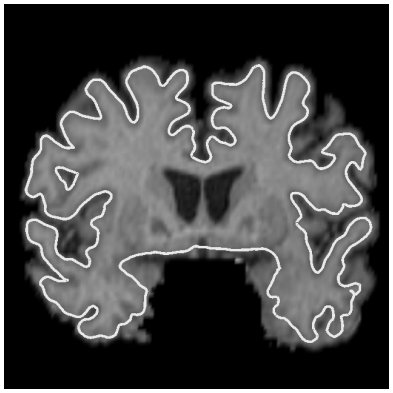

(a) Subject 1

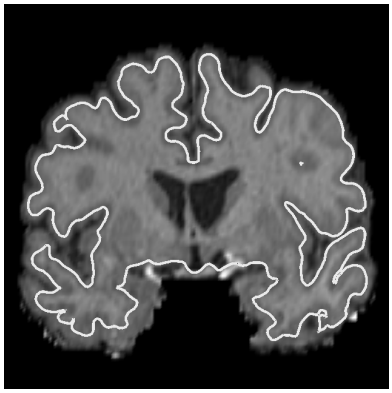

(b) Subject 2

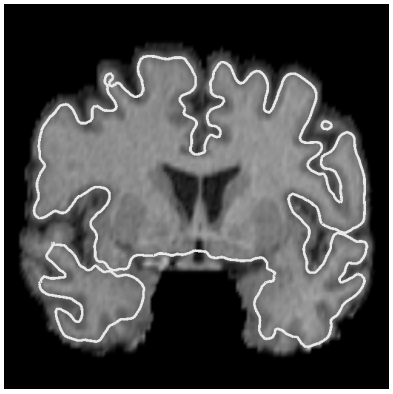

(c) Subject 3

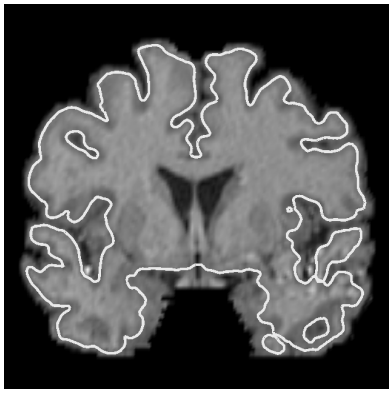

(d) Subject 4

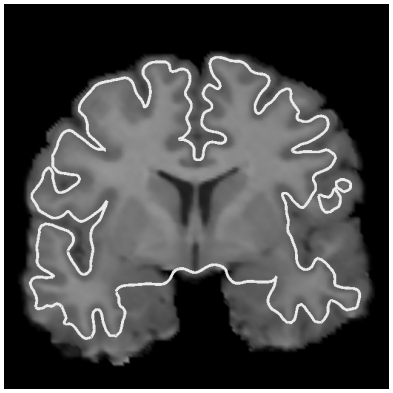

(e) Subject 5

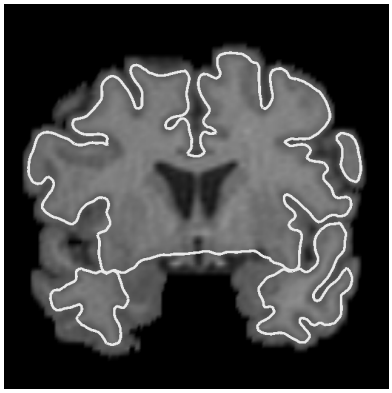

(f) Subject 6

Figure 5.12: From left to right and top to bottom, the coronal slice across the anterior commissure for subjects 1 to 6 superimposed with the cross section of the corresponding reconstructed cortical surface.

Table 5.3: Euler characteristics of surfaces generated for six subjects at different iterations.

Iteration(s)	0	1	2	3	4	5	6	7	8	9
Subject 1	-757	-49	-6	2	–	–	–	–	–	–
Subject 2	-1010	-56	-14	-4	-2	-2	-2	-2	0	2
Subject 3	-666	-50	-16	-12	-4	-2	0	0	2	–
Subject 4	-860	-66	-24	-8	-6	-2	-2	-2	2	–
Subject 5	-253	-59	-29	-19	-13	-9	-5	-2	2	–
Subject 6	-462	-26	-12	-6	0	2	–	–	–	–

Table 5.4: GM percentage measure of reconstructed surfaces for six subjects

Subject	1	2	3	4	5	6
GM%	97.97	96.92	97.31	96.74	97.64	98.45

Gray Matter Percentage

Since our deformable surface algorithm is designed to converge to the GM, as an initial evaluation for each reconstructed surface, we computed the percentage η of the surface area that was inside the GM,

$$\eta = \frac{\int_\Omega H_{gm}(\mathbf{x}) dA}{\int_\Omega dA} \times 100,$$

where Ω is the reconstructed surface with brain stem region excluded and H_{gm} is a binary segmentation of GM. H_{gm} is derived from the fuzzy membership functions as following

$$H_{gm}(\mathbf{x}) = \begin{cases} 1 & \text{if} \quad u_{gm}(\mathbf{x}) = \max(u_{csf}(\mathbf{x}), u_{gm}(\mathbf{x}), u_{wm}(\mathbf{x})) \\ 0 & \text{otherwise.} \end{cases}$$

The GM percentage for each reconstructed cortical surface is shown in Table 5.4. All the reconstructions have GM percentage over 96%. We believe that those parts of the surface not lying in the GM are mostly found in the WM crossing a gyrus that is not reconstructed well, such as the superior temporal gyrus.

Table 5.5: Landmark errors (in mm)

	Subject							
Sulcus	1	2	3	4	5	6	Mean	Std
CS_1	1.21	2.40	1.48	0.22	0.63	0.47	1.10	0.80
CS_2	1.67	1.84	0.86	1.17	1.27	2.02	1.50	0.44
PCG_1	0.77	0.66	0.34	0.64	1.27	0.67	0.73	0.30
PCG_2	0.84	0.96	0.93	0.67	0.40	0.35	0.69	0.27
TLG_1	0.34	0.60	2.90	0.93	2.80	0.47	1.30	1.20
TLG_2	3.50	2.12	0.98	1.25	5.73	1.29	2.50	1.80
$CALC_1$	0.82	0.68	1.31	0.25	0.38	0.68	0.69	0.37
$CALC_2$	1.25	5.73	2.92	0.63	2.24	0.39	2.20	2.00
MFG_1	0.32	0.75	0.66	1.38	0.34	0.45	0.65	0.40
MFG_2	1.37	1.35	0.64	0.23	1.01	1.06	0.94	0.44
Mean	1.20	1.70	1.30	0.74	1.60	0.78	–	–
Std	0.91	1.60	0.91	0.43	1.70	0.53	–	–

Landmark Errors

The GM percentage gives a global measure of how much of the reconstructed surface is in the GM, but it does not reflect whether the surface coincides with the central cortical layer. To get a sense of this accuracy and how it varies across the cortex, we computed a series of *landmark errors* for each of the six surfaces. We picked five landmarks on the central cortical layer of each hemisphere on all subjects. Details of how these landmarks were picked and how the landmarks errors were calculated are given in Section 5.A. The landmarks were located on the fundus of the central sulcus (CS), the crown of the post-central gyrus (PCG), the most anterior point of the temporal lobe (TLG), midway along the fundus of the calcarine sulcus (CALC), and on the medial frontal gyrus (MFG). The landmark error was then computed as the minimum distance between the given landmark and the reconstructed surface.

The computed landmark errors for all six subjects are shown in Table 5.5. The mean landmark error is between 1 and 2 mm for all six subjects. It is difficult to pick up a trend from these results, and perhaps not fruitful given the small sample population. However, it should be noted that the largest error is 5.73 mm, for $CALC_2$ of Subject 2. The CALC and CS landmarks are the only landmarks at sulcal fundi,

which should be close to the initial deformable surface. We have noted, however, that where the sulcal banks are very close together, our deformable surface model sometimes travels too far outward toward the outer brain surface. This is probably the cause of this largest error and other large errors associated with the CALC and CS landmarks. The other landmarks are associated with gyri, and are therefore near the outer brain surface. In this case the deformable surface may have the farthest distance to move, and may get trapped before reaching the correct destination. We have observed that this is particularly problematic for the superior temporal lobe, which is reflected in the TLG landmark errors. The best convergence accuracy can be expected in the relatively broad gyri, reflected in the PCG and MFG landmark errors.

Parameter Selection

Our method requires the selection of several parameters that affect its overall performance. We have found that the algorithm is quite robust to variations in λ_1, λ_2, and κ, and that the nominal values we have used yield the best overall results (see [84, 122]). Tradeoffs between the parameters controlling the deformable surface, however, can more significantly influence the result. Therefore, we conducted a numerical experiment in order to find the best ranges of parameters to use in our deformable surface model. These results are reported here.

We used the "BrainWeb" simulated brain data obtained from the McConnell Brain Imaging Centre at McGill University website [18], generated using the following parameters: 1mm cubic pixels, T1-weighted contrast, 3% noise, and 20% inhomogeneity level. We then varied the parameters of the deformable surface model to obtain a series of reconstructed cortical surfaces. For each reconstructed cortical surface, we computed its GM percentage and landmark errors. We found that the best performance occurs when $\beta = 0$, which implies that the deformable surface has no resistance to bending. The GM percentages computed for different α and k_2 values are summarized in Table 5.6. From the table, $\alpha = 0.5, 0.75$ and $k_2 = 0.01, 0.02$ seem to yield consistently higher GM percentages.

Table 5.6: GM percentage using AFCM GM segmentation

$\beta = 0, k_1 = 0.5$	k_2				
α	0	0.005	0.01	0.02	0.04
0.25	97.52	98.40	98.73	98.88	98.66
0.5	97.94	98.56	98.82	99.12	99.05
0.75	98.00	98.56	98.79	99.12	99.16

Table 5.7: GM percentage using true GM segmentation

$\beta = 0, k_1 = 0.5$	k_2				
α	0	0.005	0.01	0.02	0.04
0.25	97.53	98.32	98.59	98.72	98.54
0.5	97.87	98.45	98.67	98.93	98.87
0.75	97.91	98.40	98.64	98.94	98.97

The "BrainWeb" simulated brain data also comes with a true GM segmentation. This allows us to compute the true GM percentage. The results are shown in Table 5.7. By comparing two tables, one can see that GM percentages computed from the deformable surfaces using AFCM GM segmentation differs by at most 0.2% from the values computed from the deformable surfaces using true GM segmentation. This demonstrates the advantage of using AFCM and the robustness of our reconstruction method to noise and image inhomogeneities.

The landmark errors are derived from the landmarks picked on the true brain data where no noise and inhomogeneity is present. The computed landmark errors are summarized in Table 5.8. From the table, $\alpha = 0.5$ and $k_2 = 0.01, 0.02, 0.04$ seem to yield consistently lower landmark errors.

The results from both GM percentages and landmark errors suggests that we achieve the lowest errors when $\alpha = 0.5$ and $k_2 = 0.01$ or 0.02. This is consistent with our conclusion through visual inspection and the parameters match well with our empirically chosen parameters.

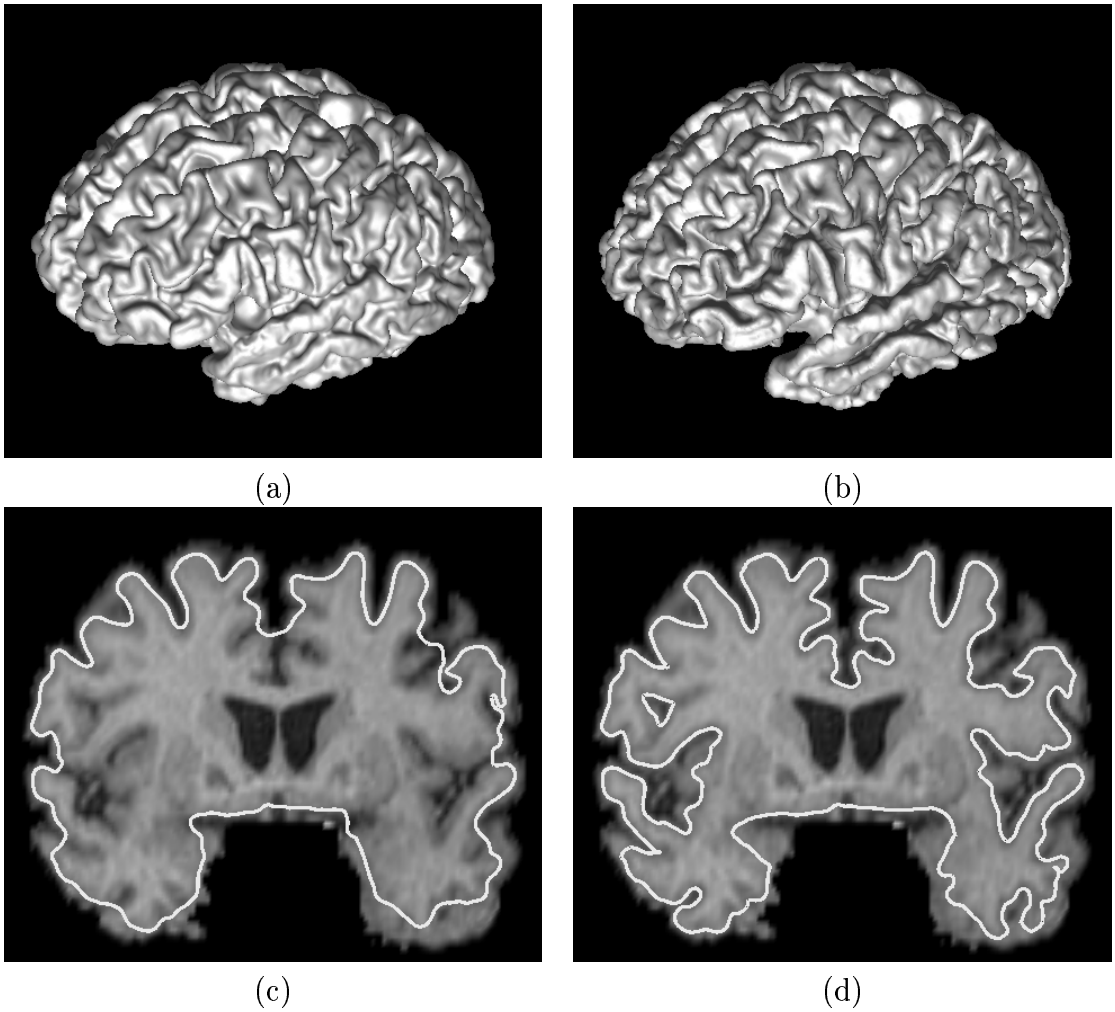

Figure 5.13: Surface renderings of (a) shrink-wrapping method versus (b) proposed method. Cross-sections of (c) shrink-wrapping method versus (d) proposed method.

Table 5.8: Landmark errors for phantom data (in mm)

$\beta = 0, k_1 = 0.5$	k_2				
α	0	0.005	0.01	0.02	0.04
0.25	0.97	0.94	0.88	0.88	0.89
0.5	1.05	0.99	0.85	0.83	0.85
0.75	1.06	1.06	0.89	0.87	0.85

Comparison with Shrink-wrapping

"Shrink-wrapping" is a well-known approach to finding a parametric representation of the brain surface [72, 94, 31, 95]. This approach uses a deformable surface that is initialized as a simple geometric object (sphere or ellipsoid) outside the cortex, and the surface is then pushed toward the cortex by the action of internal and external forces. For comparative purposes, we implemented a shrink-wrapping deformable model that started from an initial sphere outside the brain surface and deformed toward the central layer of the GM using GGVF forces. The resulting surface of Subject 1 is shown in Fig. 5.13a, while the surface found by our method is shown in Fig. 5.13b. These surfaces look very similar, and it is not apparent from these renderings that there is much difference in these approaches.

A profound difference between these two approaches is revealed, however, in the cross-sectional images shown in Figs. 5.13c and 5.13d. Clearly, the shrink-wrapping method only finds the outermost cortical layer. It is interesting to note that the GM percentage of the shrink-wrapping method is 94%, a fairly large number. However, this number merely indicates that the final surface resides overwhelmingly within the GM, but does not indicate how faithfully it tracks the entire cortex. In fact, the landmark errors computed for the shrink-wrapping result shows substantial errors (4-10 mm) in the CS, CALC, MFG landmarks, which are landmarks that either reside within sulci or within the interhemispheric fissure. This demonstrates the importance of initializing the deformable surface from inside the cortical GM.

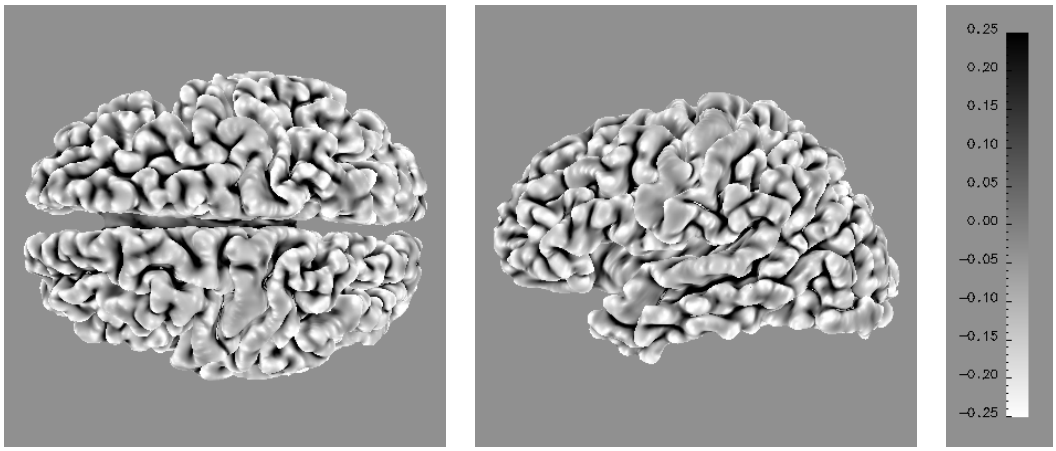

(a) (b) (c)

Figure 5.14: (a) Front and (b) lateral views of a cortical mean curvature map. (c) Colormap used for plotting the map.

5.3 Applications

5.3.1 Cortical Differential Geometry and Thickness Computation

Once the cortical surface has been extracted, differential geometry quantities may be computed. Differential geometry provides a natural mathematical framework to study the cortical surface geometry. Among many geometric quantities defined for the surface, curvature information is the most valuable since it quantifies the structure of the sulci and gyri, thus providing the basis for scientific and comparative studies. Our deformable surfaces are represented numerically using simplex meshes [37, 36] as described in Appendix A.2.1. We have developed a robust algorithm to calculate mean, Gaussian, and principal curvatures on a simplex mesh surface. Details about the algorithm can be found in Appendix B.

Fig. 5.14 shows two views of the mean curvature, plotted on the extracted cortical surface of our sample data set. In these figures, black stands for positive mean curvature values, gray stands for zero, and white stands for negative mean curvature values. From the figures, we see that sulci are described by black central "skeletons"

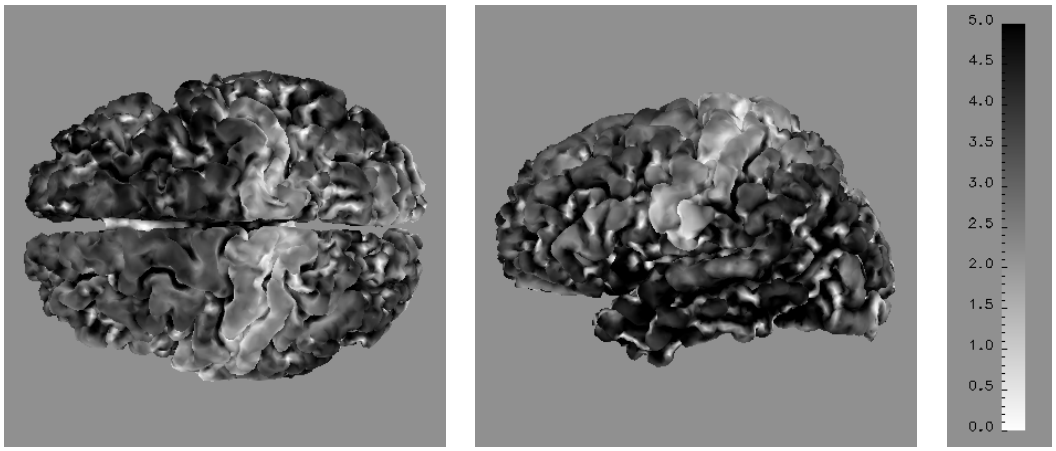

(a) (b) (c)

Figure 5.15: (a) Front and (b) lateral views of a cortical thickness map. (c) Colormap used for plotting the map.

surrounded by white regions. These skeletons, which are in the interior of the brain, correspond to the "roots" of the sulci, while the white regions are the "lips" of the sulci on the surface of the brain. This correspondence between the structure of sulci/gyri and mean curvature provides the basis for brain geometry analysis.

We have recently implemented a preliminary algorithm to compute *cortical thickness* in the vicinity of the central cortical layer estimate. For every point on the surface, we search in the direction of the simplex mesh normal vector until the closest peak in the gray matter membership function is located. If this peak is not above 0.7, then we are unable to calculate a legitimate thickness value. If this peak is above 0.7, then the thickness is calculated as the distance between the two points along the unit normal at which the gray matter membership function falls below 0.2. A thickness map resulting from this calculation is shown in Fig. 5.15, where black represents 5.0mm, gray represents 2.5mm, and white represents points at which the thickness could not be reliably estimated. We note that this result is very preliminary, and requires substantial improvements and validation, as is planned in the future work summarized in Chapter 6.

5.3.2 A Spherical Map for Cortical Geometry

Characterizing normal versus abnormal cortical geometry is an important goal of human brain mapping. This task proves difficult because of the convoluted nature of the cortical surface. Difficulties arise in both identifying topological landmarks and obtaining reliable quantitative measurements. A standard measurement method is to trace sulcal fundi or other regions of interest across 2-D slices in MRI scans. Accurate measurements are difficult to obtain using this method because structures must be identified across slices and a true 3-D geometric analysis is not possible.

Here, we present a preliminary method for representing the cortical surface that facilitates visualization and delineation of regions on the cortical surface. We generate a spherical map for each cortical hemisphere so that the full extent of sulcal fundi and the buried cortex within the sulcal folds can be visualized. The spherical map has a one-to-one mapping with the reconstructed cortical surface. This allows regions of interest to be identified on the spherical map and accurate measurement analysis to be made on the 3-D geometry of the cortical surface.

Six hemispheres from three MR brain images were analyzed. On each brain, the topologically correct, central cortical layer was reconstructed. To create the spherical map, the hemispheres were separated using a cut through the corpus callosum. This caused an opening to be created around the cut path. Then, focusing on one hemisphere, the opening was mapped to a circle. Next, an elastic relaxation process was applied to the surface until it reached a convex shape. Then, a fast projection method was used to transform the relaxed surface to a sphere. The mean curvature of the cortex was plotted on the sphere using a gray-scale colormap. The resulting spherical map of a typical hemisphere is shown in Fig. 5.16a. Large mean curvatures appear dark so sulcal fundi are readily identified as thin dark streaks. In Fig. 5.16a, the region of cortex buried within the central sulcus (outlined in black) shows the characteristic precentral knob of this sulcus. Fig. 5.16b shows this region of buried cortex as it appears in the brain.

Using the techniques described, we have manually delineated the buried cortex surrounding primary sulci on the spherical map. These regions are displayed on the

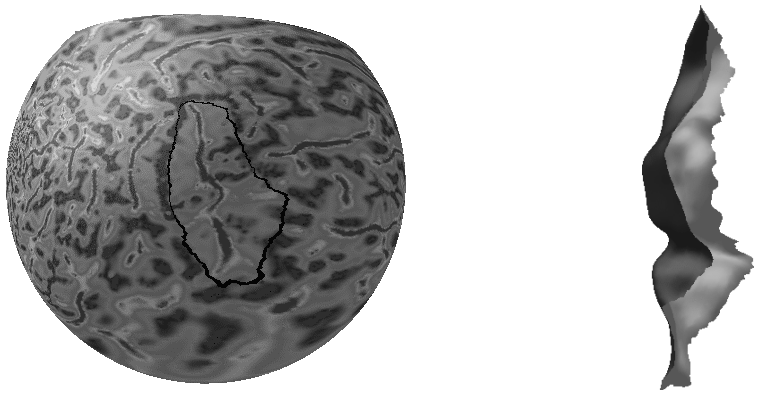

(a) (b)

Figure 5.16: (a) A spherical map depicting mean curvature. The central sulcus is outlined in black. (b) Manually identified central sulcus.

spherical map in Fig. 5.17a. These regions are also displayed on the reconstructed cortical surface in Fig. 5.17b.

5.4 Summary

We presented a method for reconstructing cortical surfaces from MR brain images. This method combines a fuzzy segmentation method, an isosurface algorithm, and a new deformable surface model to reconstruct a surface representation of the cortical central layer. The reconstructed surfaces include deep gyri and sulci and possess the correct surface topology of the cortex. The process is mostly automated and produces surfaces that are typically within 1-2 mm of the correct location throughout the cortex. We described some preliminary work on the application of cortical surface reconstruction. We developed a method for computing differential geometry quantities on cortical surfaces and demonstrated the feasibility of calculating cortical thickness map. Finally, we showed that spherical maps that have a one-to-one mapping with reconstructed cortical surfaces can be constructed. This allows delineation of regions of interest such as sulci on the spherical map and analysis of the segmented regions on the convoluted surface.

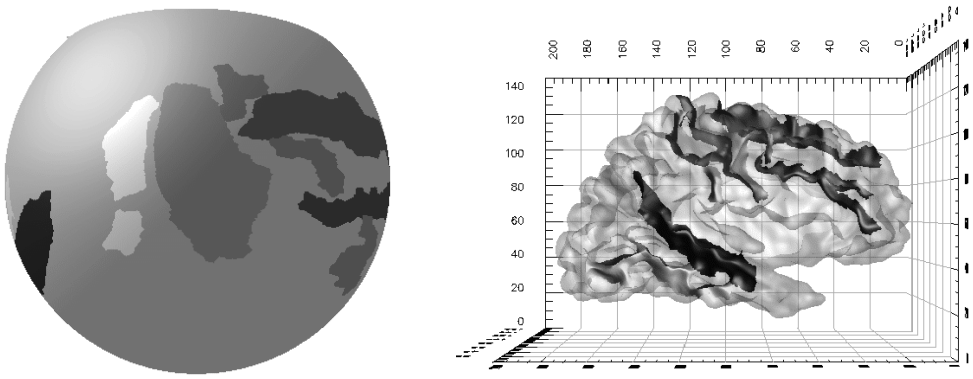

(a) (b)

Figure 5.17: Manually identified sulci on (a) the spherical map, and (b) the cortical surface.

5.A Landmark Picking and Landmark Errors

To pick landmarks, an IBM Data Explorer [8] visual program was written to display three 2-D orthogonal views of the raw MR brain volume. Within each view, the positions of the other two slices were superimposed forming a cross. An operator then selected three views such that the center of the cross in each view lay on the central layer of the GM within a designated volume of interest (VOI). The landmark coordinates were recorded as the physical positions of these three views.

Landmarks determined in this way were treated as the truth in the calculation of landmark errors in Section 3. It is important to understand the effect of operator error, however, on the reported errors. Referring to Fig. 5.18, we see that the picked landmark P^* will, in general, be some distance Δ from a point P on the true central layer, and the reported error $e = |QP^*|$ will be different from the true error $\varepsilon = |QP|$. It is straightforward to show that $\varepsilon \in [e - \Delta, e + \Delta]$, which leads to the conclusion that e is a good measure of error provided that Δ is small relative to e. It remains to determine what is the operator error Δ.

We found that an operator can pick a point on the central layer of the cortex very accurately using the described procedure. The main reason for this accuracy is that

[8] IBM Almaden Research Center, San Jose, CA.

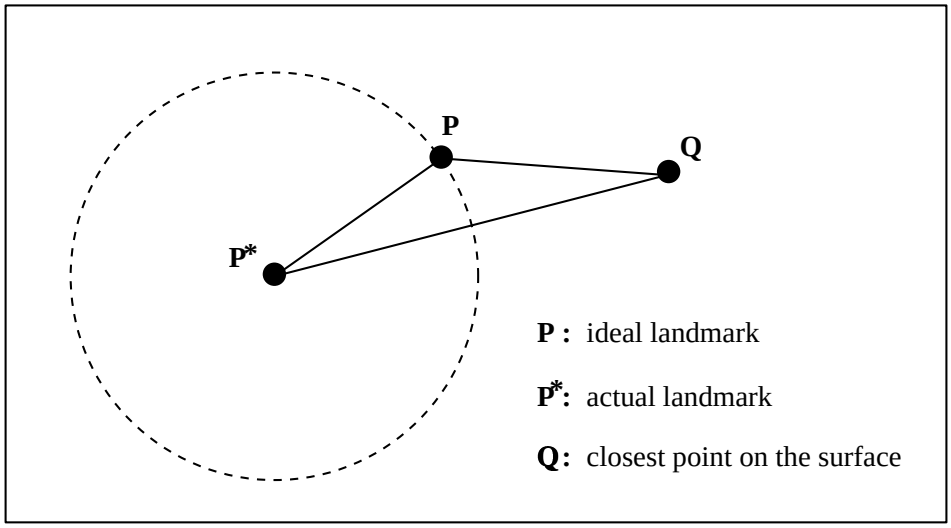

Figure 5.18: Illustration of the configuration of ideal landmark, actual landmark, and closest point on the surface.

the operator does not need to pick a specific point, but only a point within a VOI that is on the central cortex in all three views. To get an approximate measure of this accuracy, we designed a Monte-Carlo simulation to approximate the landmark picking error introduced by the operator. We assume that our VOI is 10x10x10 voxels, each voxel is $1mm^3$, and that the central cortical surface in the VOI is a plane. For a plane passing through the VOI with arbitrary location and orientation, we assumed that the operator could pick the grid point closest to the plane, and the distance between this grid point and the plane is the operator error for this particular experiment. By varying the plane position and orientation randomly, we can measure the mean operator error and use it as our estimation of the landmark picking error introduced by the operator. We uniformly sampled 10^9 random planes from all possible planes passing the VOI, yielding a mean operator error of 0.04 mm. Even if the true operator error were 2–5 times this error, it would still be relatively small in comparison to the typical errors reported in Section 5.2.

Chapter 6

Conclusions and Future Work

This thesis considered the problem of mapping boundaries in digital images. We developed two new deformable models and validated their performance both qualitatively and quantitatively on numerous examples. Based on the proposed deformable models, we also developed a new method for cortical surface reconstruction and validated this method using both simulated and real MR images. In this chapter we summarize the main results and propose new directions for future research.

6.1 Gradient Vector Flow Deformable Models

In Chapter 3, we first generalized the force balance equations to allow use of a general vector field rather than an irrotational (conservative) vector field. This generalization led us to develop a general vector field called gradient vector flow (GVF) computed through a vector diffusion process of the gradient of an edge map. The GVF vector field can be used as an external force field for a deformable model to reconstruct the parametric description of a target boundary.

The main results of this work and ideas for future work are summarized below.

6.1.1 Main Results

1. Both traditional external forces and distance potential forces are conservative

force fields and do not point into boundary concavities, while GVF, which is a general type of force field, does.

2. Unlike traditional external force fields, the GVF field has a large capture range without distorting the boundary.

3. Unlike balloon models, the GVF deformable model preserves perceptual boundaries.

4. Balloon models must be initialized completely inside or outside target boundaries because balloon forces can only push out or push in. The GVF deformable model, however, can be initialized across boundaries as well.

5. Simulation results show that GVF can smooth out weak gradients while maintaining strong gradients, which makes the deformable models using GVF perform robustly against image noise.

6.1.2 Future Work

Further investigations into the nature and uses of GVF are warranted. In particular, a complete characterization of the capture range of the GVF field would help in deformable model initialization procedures. It would also help to more fully understand the GVF parameter μ, perhaps finding a way to choose it optimally for a particular image, and to understand the interplay between μ and the internal force weighting parameters α and β. Finally, the GVF framework might be useful in defining new connections between parametric and geometric deformable models, and might form the basis for a new geometric rather than parametric deformable model.

6.2 Generalized Gradient Vector Flow Deformable Models

In Chapter 4, we developed a generalization of the GVF formulation called generalized gradient vector flow (GGVF, which incorporates two spatially-varying weighting

functions. This new formulation can produce a numerically faster diffusion process in homogeneous regions while maintaining excellent boundary localization capabilities. We also noted that GGVF can be used as new way to represent images by encoding both boundary information and medialness information in one representation. Finally, we exploited the medialness property of the GGVF and developed a method to reconstruct the central layer of thick boundaries.

6.2.1 Main Results

1. Simulation results show that GGVF improves deformable model convergence into long, thin boundary indentations, and maintains other desirable properties of GVF, such as an extended capture range.

2. On a series of simulated images, we compared the boundary localizing accuracy of deformable models using GGVF, GVF, distance potential forces, and traditional external forces, which are initialized at the true location of target boundaries to study the ideal best performance of each model. Our results show that deformable models using GGVF, GVF, distance potential forces, and traditional external forces ($\sigma = 1$) all yield high accuracy consistently with maximum radial errors less than 0.75 pixels, while the performance of deformable models using external forces with larger smoothing parameter ($\sigma = 3$ and $\sigma = 6$) degenerates almost linearly with respect to the increase of boundary undulation. This indicates that traditional forces with larger smoothing parameter is not suitable for reconstructing objects with convoluted boundaries even though the deformable model starts at the desired boundary.

3. Simulation results show that the performance of both the GGVF deformable model (MRE = 2.2) and the GVF deformable model (MRE = 2.3) is not sensitive to impulsive noise present in the images while the performance of other methods degenerated significantly.

4. Simulation results show that GGVF deformable models can accurately reconstruct the central layer of boundaries with thickness less than 6 pixels wide

with MREs less than 0.7 pixels, while the reconstruction is less accurate with MREs almost doubled when the boundary thickness is 9 pixels wide. This result demonstrates the applicability of GGVF deformable models in the human brain cortex reconstruction since the cortex usually has thickness between 3 to 5 voxels.

6.2.2 Future Work

In future research, we would like to study other choices of weighting functions and their implications in the behavior of deformable models. Also, further investigation of the GGVF medialness properties and possible finding of its mathematical relationship to classical medialness such as skeleton and cores may shed new light on the research of shape representation. The current formulation of GGVF is in Euclidean spaces. It would be interesting to investigate the possibility of extending its formulation onto manifolds, especially surfaces. Finally, making connections between GGVF with other applications in image processing and computer vision might provide some new insights or even new solutions to existing problems.

6.3 Brain Cortex Reconstruction

In Chapter 5, we developed a method for reconstructing cortical surfaces from MR brain images. This new method is largely automated. The method uses a novel approach to initialize deformable models using isosurface algorithms. It reconstructs the cortical surfaces including deep gyri and sulci and possessing the correct surface topology. We developed two performance measures: gray matter percentage and landmark error, which allows us to quantify the performance of our methods on real brain MR images. We developed a method to compute differential geometry quantities for the cortical surface reconstructed. We carried out a preliminary investigation on generating a spherical map from reconstructed cortical surface.

6.3.1 Main Results

1. Experimental results show that the topology of isosurfaces can be corrected by median filtering the WM membership function iteratively.

2. Experimental results show that reliable and robust cortical surface reconstruction results can be achieved by applying deformable models on the fuzzy membership functions instead of on the raw intensity images.

3. Experimental results show that for six volumetric brain MR images with voxels size on the order of $1mm^3$, our reconstruction method can produce surfaces that are typically within 1-2 mm of the correct location throughout the cortex.

4. Experimental results show that the gray matter percentages of the reconstructed cortical surfaces are consistently above 96.5%.

5. The proposed method produces significantly better results than does a conventional shrink-wrapping method. In an experiment, the proposed method produced a gray matter percentage of 98% and landmark errors between 0.32 mm and 3.50 mm (with an average of 1.2 mm) whereas the shrink-wrapping method yielded a gray matter percentage of 94% and substantial landmark errors between 4 mm and 10 mm.

6.3.2 Future Work

Future work includes reduction of the required manual intervention and improved convergence to narrow, extended gyri. Since the initial surface is already very dense, we cannot use usual subdivision technique to decrease the running time of the model. However, implementing the deformable models in a multiresolution fashion can significantly reduce the running time. Due to imaging resolution, the intensities of certain GM/GM interface in the sulci may appear to be completely flat in the GM membership function, which can lead to a location shift in the reconstructed central cortical surface in these regions. We would like to incorporate anatomical constraints to address this problem. Accurate thickness estimation is an important area of future

research. We believe that improved results will be obtained by incorporating more prior knowledge about thickness variability. Our current approach to spherical mapping is time consuming (usually 12 hours), and generates a spherical map without using any distortion minimization criteria. Further research in this area is expected to focus on reducing running time and minimizing length, angle, or area distortion.

Furthermore, since our work on cortical surface reconstruction generates a mapping of entire cortical surface, study of various brain structures can now be done in a more precise way. Also functional data can be mapped onto the reconstructed cortical surface to study the relationship between structure and function hence to further enhance our understand about the brain.

6.4 Overall Perspective

The main goal of the work presented in this thesis has been to contribute to boundary mapping through the development of new deformable models, and to investigate their application to brain cortex reconstruction from MR images. It is hoped that the research herein can deepen the understanding of deformable models and point out new directions for designing better deformable models and extending their applications into other areas in medical imaging, image analysis and computer vision.

Appendix A

Deformable Model Implementation

In this appendix, the implementation of both deformable contours and surfaces is described.

A.1 Deformable Contours

Both the traditional deformable contour model and the GGVF(GVF) deformable contour model can be characterized by the following dynamic equation

$$\begin{cases} \mathbf{x}_t(s;t) &= (\alpha(s)\mathbf{x}'(s;t))' - (\beta(s)\mathbf{x}''(s;t))'' + \mathbf{F}_{\text{ext}}(\mathbf{x}) \\ \mathbf{x}(s;0) &= \mathbf{x}_0(s) \end{cases} \tag{A.1}$$

where $\mathbf{F}_{\text{ext}}$ is the external force and $\mathbf{x}'$ denotes the partial derivative of $\mathbf{x}$ with respect to s. The equation reduces to Eq. (3.2) when the values of α and β are chosen to be constants.

Approximating the derivatives with finite differences, and converting to the vector notation $\mathbf{x}_i = (x_i, y_i) = (x(ih), y(ih))$, we can rewrite Eq. (A.1) as

$$\begin{aligned} \frac{\mathbf{x_i}^t - \mathbf{x_i}^{t-1}}{\tau} &= -\alpha_i(\mathbf{x}_i^t - \mathbf{x}_{i-1}^t) + \alpha_{i+1}(\mathbf{x}_{i+1}^t - \mathbf{x}_i^t) \\ &\quad -\beta_{i-1}(\mathbf{x}_{i-2}^t - 2\mathbf{x}_{i-1}^t + \mathbf{x}_i^t) \\ &\quad +2\beta_i(\mathbf{x}_{i-1}^t - 2\mathbf{x}_i^t + \mathbf{x}_{i+1}^t) \\ &\quad -\beta_{i+1}(\mathbf{x}_i^t - 2\mathbf{x}_{i+1}^t + \mathbf{x}_{i+2}^t) + \mathbf{F}_{\text{ext}}(\mathbf{x}_i^{t-1}) \end{aligned} \tag{A.2}$$

where $\mathbf{x}_i = \mathbf{x}(ih)$, $\alpha_i = \alpha(ih)$, $\beta_i = \beta(ih)$, h the step size in space, and τ the step size in time. In general, the external force $\mathbf{F}_{\text{ext}}$ is stored as a discrete vector field, i.e., a finite set of vectors defined on an image grid. The value of $\mathbf{F}_{\text{ext}}$ at any location $\mathbf{x}_i$ can be obtained through a bilinear interpolation of the external force values at the grid points near $\mathbf{x}_i$.

Eq. (A.2) can be written in a compact matrix form as

$$\frac{\mathbf{x}^t - \mathbf{x}^{t-1}}{\tau} = \mathbf{A}\mathbf{x}^t + \mathbf{F}_{\text{ext}}(\mathbf{x}^{t-1}) \tag{A.3}$$

where $\mathbf{A}$ is a pentadiagonal banded matrix.

Eq. (A.3) can then be solved iteratively by matrix inversion:

$$\mathbf{x}^t = (\mathbf{I} - \tau\mathbf{A})^{-1}(\mathbf{x}^{t-1} + \tau\mathbf{F}_{\text{ext}}(\mathbf{x}^{t-1})). \tag{A.4}$$

We note that since the above finite difference scheme is implicit with respect to the internal forces, it can solve very rigid deformable contours with large step sizes [62, 4].

A.2 Deformable Surfaces

A typical dynamic deformable surface model is described in Eq. (2.10). It can be expanded and written as the following:

$$\begin{cases} \mathbf{x}_t(\mathbf{u};t) &= \alpha\nabla^2_{\mathbf{u}}\mathbf{x}(\mathbf{u};t) - \beta\nabla^2_{\mathbf{u}}(\nabla^2_{\mathbf{u}}\mathbf{x}(\mathbf{u};t)) + \mathbf{F}_{\text{ext}}(\mathbf{x}) \\ \mathbf{x}(\mathbf{u};0) &= \mathbf{x}_0(\mathbf{u}). \end{cases} \tag{A.5}$$

In order to find a solution to this dynamic partial differential equation, it is necessary to represent the continuous deformable surface $\mathbf{x}$ with a discrete mesh. It is possible to use either finite-element methods (cf. [19, 21, 76]) or Fourier basis methods (cf. [100, 101]) to solve Eq. (A.5). These methods, however, are slow for meshes with a large number of nodes. On the other hand, finite difference methods (cf. [36, 42, 27]) based on polygon mesh models requires only simple arithmetic operations at each node of the mesh and therefore are more suitable for implementing meshes with a large number of nodes, such as those used in cortical surface reconstruction. In our

work, we implemented the deformable surfaces using the finite difference method on a polygon mesh model called the *simplex mesh* [37, 36, 38].

In this section, we first introduce the definition of simplex meshes. We then describe how to generate simplex meshes. Finally, we describe how to implement deformable surfaces represented by the simplex mesh. We note that all surfaces and their corresponding meshes described in the rest of the appendix are assumed to be closed although we expect our discussions are applicable to open surfaces with minor modification.

A.2.1 Simplex Meshes: a Surface Representation for Deformable Surfaces

A simplex mesh is a polygon mesh where each node or vertex on the mesh has a constant number of connections to its neighbors. A simplex mesh can be defined in any dimension. A k-simplex mesh is defined as a $(k+1)$-connected mesh where each vertex has exactly $(k+1)$ neighbors. Formally, a $k-$Simplex Mesh $\mathcal{M}$ of $\mathbf{R}^d$ is defined as a pair $(V(\mathcal{M}), N(\mathcal{M}))$ where $V(\mathcal{M})$ is the set of vertices of $\mathcal{M}$ given by

$$V(\mathcal{M}) = \{P_i\}, i \in \{1, \ldots, n\}, P_i \in \mathbf{R}^d \tag{A.6}$$

and $N(\mathcal{M})$ is the associated connectivity function defined by

$$N(\mathcal{M}) : \{1, \ldots, n\} \longrightarrow \{1, \ldots, n\}^{k+1}$$

such that

$$\forall i \in \{1, \ldots, n\},\ i \longmapsto (N_1(i), N_2(i), \ldots, N_{k+1}(i)) \tag{A.7}$$

and

$$\forall i \in \{1, \ldots, n\}, \forall j \in \{1, \ldots, k+1\}, \forall l \in \{1, \ldots, k+1\}, l \neq j$$

$$(1)\ N_j(i) \neq i \tag{A.8}$$

$$(2)\ N_l(i) \neq N_j(i), \tag{A.9}$$

Conditions Eq. (A.8) and (A.9) prevent a mesh from exhibiting loops or double edges as shown in Fig. A.1. We further restrict a k-simplex mesh to be connected in such a

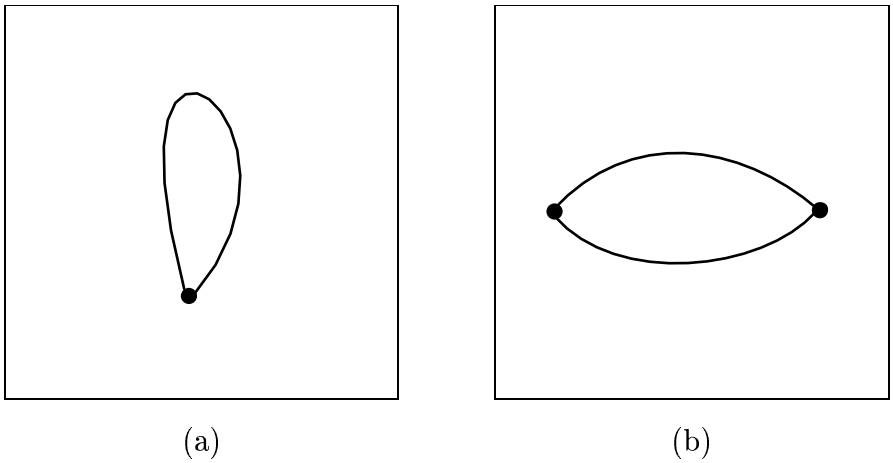

Figure A.1: (a) a loop; (b) double edges.

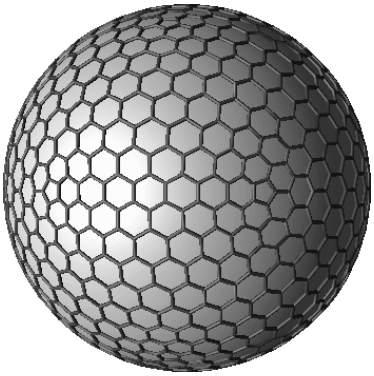

Figure A.2: A simplex mesh.

way that for any two vertices there exists a path joining them. In our work, we will only consider 2-simplex meshes in $\mathbf{R}^3$.

From the definition of a k-simplex mesh, we know that a 2-simplex mesh must be a 3-connected mesh. This is an important property that is used to simplify and speed up the deformable surface implementation in Section A.2.4. An example of a 2-simplex mesh is shown in Fig. A.2. A 2-simplex mesh can represent any type of 3-D surface and will be simply referred from now on as a simplex mesh.

Another type of polygon mesh representation used frequently in computer graphics is a mesh consisting of only triangles (triangle meshes). Triangle meshes in general are

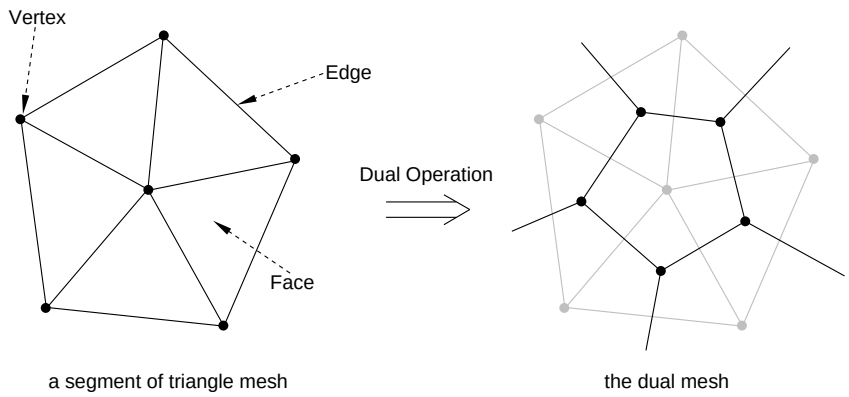

Figure A.3: Illustration of a dual operation.

easier to construct. They have been studied extensively for many years and techniques for constructing them are readily available (cf. [44, 97]). It can be shown that triangle meshes can be used to generate simplex meshes through a dual operation [37]. By definition, a dual operation on a polygon mesh constructs a new mesh where each vertex in the new mesh corresponds to a face in the original mesh and each face in the new mesh corresponds to a vertex in the original mesh as shown in Fig. A.3.

The duality between triangle meshes and simplex meshes gives rise to a convenient way to construct simplex meshes by computing the dual mesh of the triangle meshes. In next two sections, we first review two triangle mesh generation methods used frequently in computer graphics. We then describe in details about how to implement the dual operation.

A.2.2 Triangle Mesh Generation

Here we describe two well-known methods for generating triangle meshes. The first method starts with a sparse triangle mesh and subdivides each triangle into four smaller triangles recursively to generate a denser triangle mesh. The second method starts from an image volume and computes isosurfaces to generate triangle meshes.

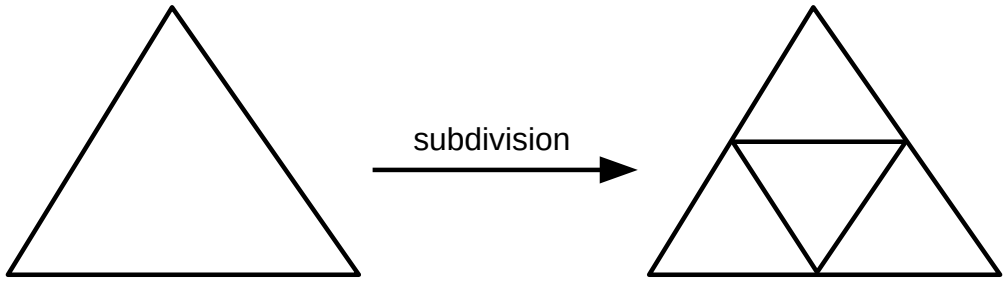

Figure A.4: A triangle and its subdivided triangles.

Subdivision method

A subdivision operation on a single triangle is shown in Fig. A.4. When a subdivision is applied on a triangle mesh, each triangle is replaced by four smaller triangles. This operation can be repeated recursively to achieve arbitrary resolution.

Subdivision can be tailored and used in a variety of applications [40, 55, 126]. One application of subdivision is to generate a triangle mesh that approximates a sphere as accurately as possible. This mesh can then be used to initialize a deformable surface. To create such a mesh, one can start by constructing an icosahedron directly, and then subdivide and project the subdivided vertices onto a sphere recursively to generate a more accurate approximation of a sphere [82]. Fig. A.5 illustrates this process. Note that the three objects shown in Fig. A.5 use 20, 80, and 320 approximating triangles, respectively.

Isosurface method

An *isosurface* is a surface that passes through all locations in space where a continuous data volume is equal to a constant value, called the isosurface threshold. The result of most isosurface algorithms is a surface tessellated, in particular, into a triangle mesh. The construction of an isosurface is a well-studied problem [71, 79]. The *marching cubes* algorithm proposed by Lorensen and Cline [71] has received a great amount of attention in recent years. It and its variants have become the standard for generating isosurfaces and are used in many commercial visualization software

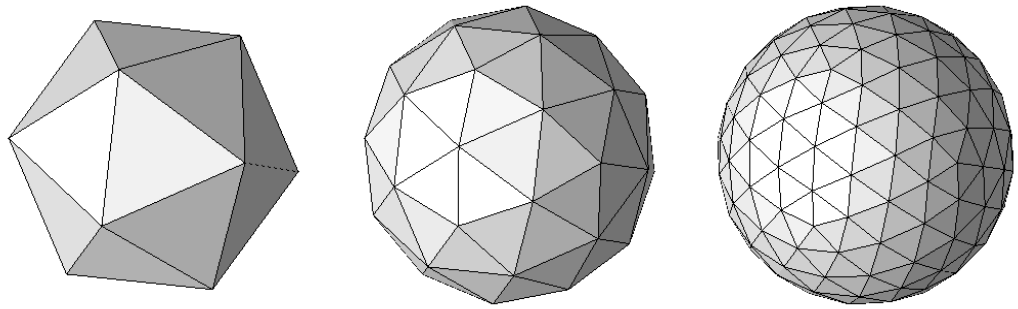

(a) (b) (c)

Figure A.5: Subdividing to improve a triangular approximation to a sphere.

packages. Below, we give a concise description of the marching cubes algorithm.

Marching cubes works directly with the volume data by breaking the volume into voxels. Each voxel is a cube with 8 vertices. Depending on whether the intensity value at a cube vertex is bigger or smaller than the isosurface threshold, a boolean value of 1 or 0 is assigned to that vertex. It can then be shown that there are 256 total possible ways a surface can pass through the cube. If one takes into account complementary and rotational symmetry, this number reduces to 14 unique configurations. From those configurations, one or more triangles are constructed for that cube using interpolation. This process is repeated throughout the volume by linear scanning.

Although marching cubes is an effective algorithm, it has been shown that it can create surface holes in certain cases. Kalvin et al. [60] proposed a variation of marching cubes called *Alligator* which solves the ambiguity problem by constraining the triangle partition of each cube using connectivity information. In Fig. A.6, we show a brain triangle mesh obtained by computing an isosurface from a 3-D MR brain image using the Alligator algorithm.

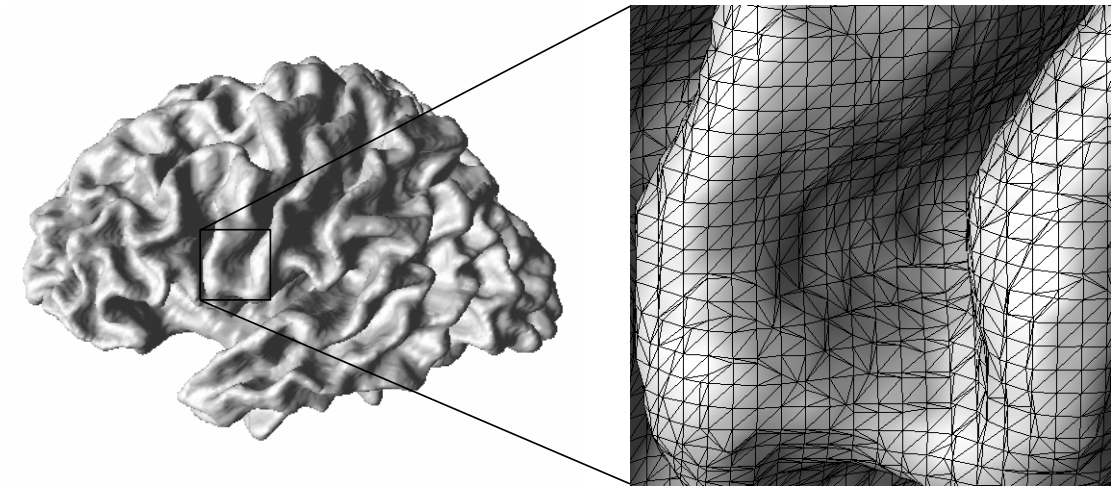

Figure A.6: Surface rendering of a brain triangle mesh obtained by computing the isosurface from a brain image volume and its zoom view with edges superimposed on the mesh.

A.2.3 Simplex Mesh Generation through Dual Operation on Triangle Meshes

The definition of a dual operation introduced in Section A.2.1 is straightforward. Its implementation, however, is not trivial. If the polygon mesh is not in a suitable representation, the dual operation can be difficult to implement and time consuming. Moreover, the mesh representation must be general enough to describe both triangle meshes and simplex meshes. A particular mesh representation in computer graphics called *winged-edge* representation has been developed to address these problems [7]. In this section, we give a brief description of winged-edge representation in the context of our work. We also outline the algorithm for implementing the dual operation based on winged-edge representation. Finally, we show several results obtained using the implemented dual operation.

Let us denote a mesh $\mathcal{M} = \{V, E, F\}$ where V is the set of vertices, E is the set of edges, and F is the set of faces. We also denote the number of vertices, the number of edges, and the number of faces as K_V, K_E, and K_F respectively. A winged-edge

representation of a mesh $\mathcal{M}$ can be described by the following collection of lists

$$\begin{aligned}
\text{Vertex list: } \{V_i\} &= \{(x_i, y_i, z_i)\}, & i = 1, 2, \ldots, K_V \\
\text{Edge list: } \{E_i\} &= \{(v_{i_1}, v_{i_2})\}, & i = 1, 2, \ldots, K_E \\
\text{Face list: } \{F_i\} &= \{(n_i, e_{i_1}, e_{i_2}, \ldots, e_{i_{n_i}})\}, & i = 1, 2, \ldots, K_F \\
\text{Edge neighbor list: } N(E_i) &= \{(f_{i_1}, f_{i_2})\}, & i = 1, 2, \ldots, K_E \\
\text{Vertex neighbor list: } N(V_i) &= \{(m_i, e_{i_1}, e_{i_2}, \ldots, e_{i_{m_i}})\}, & i = 1, 2, \ldots, K_V.
\end{aligned}$$

where V_i, E_i, and F_i are the ith vertex, edge, and face respectively. (x_i, y_i, z_i) is the coordinate of V_i. v_i, e_i, and f_i are the indices of V_i, E_i, and F_i in their respective lists. $N(E_i)$ lists a pair of neighboring faces to an edge. $N(V_i)$ lists a set of neighboring vertices to a vertex, and n_i and m_i are the number of elements in F_i and $N(V_i)$. Finally, a counter clockwise order with respect to the outward unit face (vertex) normal is imposed to the face (vertex neighbor) list.

Winged-edge representation allows fast implementation of various mesh operations. Here we define a set of operations that are necessary to implement the dual mesh.

Given an arbitrary index i, query operators for the ith vertex, edge, or face can be defined as

$$\begin{aligned}
V(i) &= V_i \\
E(i) &= E_i \\
F(i) &= F_i.
\end{aligned}$$

The operator that computes the next index to i in a n-element list is defined as

$$\text{next}(i, n) = \text{mod}(i, n) + 1$$

where $\text{mod}(i, n)$ is the modulus function. The operator that queries the jth vertex on the face F_i is defined as

$$V_j(F_i) = V(E_{i_j} \cap E_{i_{\text{next}(j,n_i)}}) = V(E(e_{i_j}) \cap E(e_{i_{\text{next}(j,n_i)}})).$$

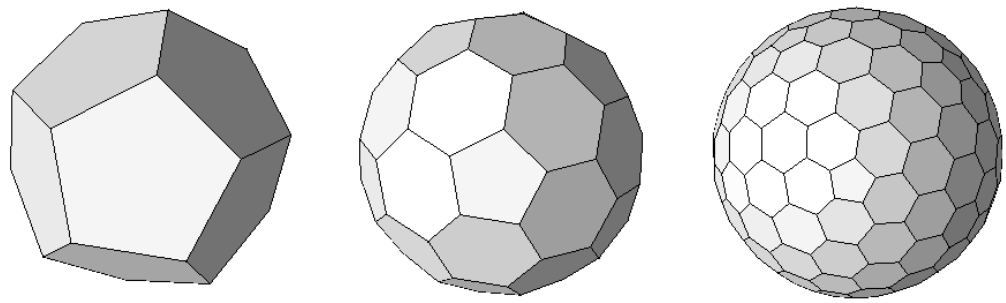

(a) (b) (c)

Figure A.7: The dual meshes of meshes shown in Fig. A.5.

The operator that computes the center of a face F_i is defined as

$$\text{center}(F_i) = \frac{1}{n_i} \sum_{j=1}^{n_i} V_j(F_i).$$

Using these operators defined, we can compute the dual mesh $\hat{\mathcal{M}} = \{\hat{V}, \hat{E}, \hat{F}\}$ of the mesh $\mathcal{M}$ using the following steps:

1. Vertex: $\hat{V}_i = \text{center}(F_i)$
2. Edge: $\hat{E}_i = N(E_i)$
3. Face: $\hat{F}_i = N(V_i)$
4. Edge neighbor: $N(\hat{E}_i) = E_i$
5. Vertex neighbor: $N(\hat{V}_i) = F_i$

The results of applying the dual operation on the meshes shown in Fig. A.5 and Fig. A.6 are shown in Fig. A.7 and Fig. A.8, respectively.

A.2.4 Deformable Surface Implementation

By discretizing the dynamic equation Eq. (A.5) on the simplex mesh using the finite difference method [53], we have the following difference equation for an arbitrary

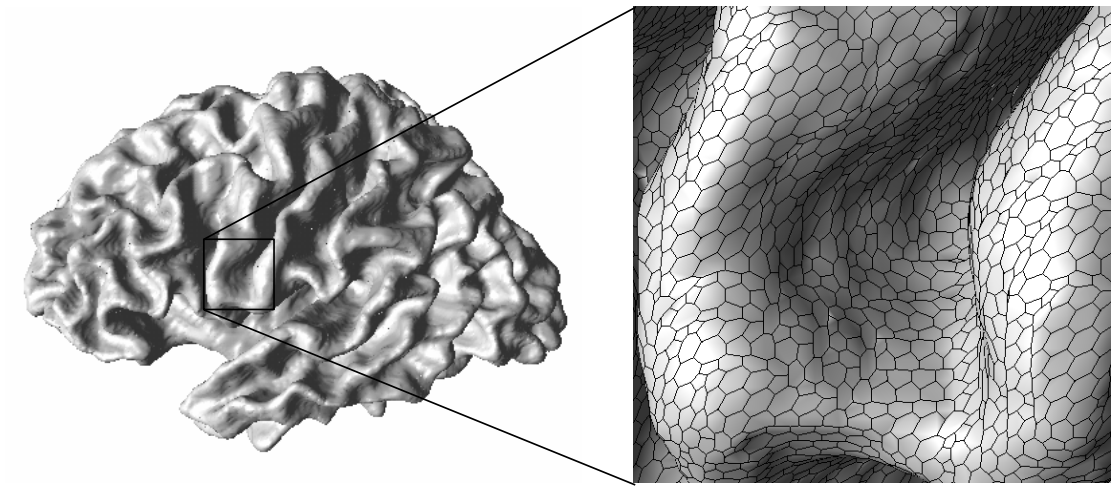

Figure A.8: The dual mesh of the mesh shown in Fig. A.6.

vertex $\mathbf{x}$

$$\mathbf{x}^t = \mathbf{x}^{t-1} + \tau(\alpha\tilde{\triangle}\mathbf{x}^{t-1} - \beta\tilde{\triangle}^2\mathbf{x}^{t-1} + \mathbf{F}_{\text{ext}}(\mathbf{x}^{t-1})) \tag{A.10}$$

where $\tilde{\triangle}\mathbf{x}$ and $\tilde{\triangle}^2\mathbf{x}$ are the discrete Laplace operator and the discrete biharmonic operator implemented on a simplex mesh. Their definitions are

$$\begin{aligned}
\tilde{\triangle}\mathbf{x} &= \frac{1}{3}(\mathbf{x}^1 + \mathbf{x}^2 + \mathbf{x}^3) - \mathbf{x} \\
\tilde{\triangle}^2\mathbf{x} &= \tilde{\triangle}(\tilde{\triangle}\mathbf{x}) \\
&= \frac{1}{9}(\sum_{i=4}^{9}\mathbf{x}^i - 6\sum_{i=1}^{3}\mathbf{x}^i + 12\mathbf{x})
\end{aligned}$$

where $\mathbf{x}^i$, $i = 1, 2, \ldots, 9$ are neighbors of the vertex $\mathbf{x}$ (Fig. A.9). Like deformable contours, $\mathbf{F}_{\text{ext}}$ can be obtained at any location $\mathbf{x}$ through a trilinear interpolation of the external force values at the image grid points near $\mathbf{x}$. It is apparent that the regularity and simplicity of the vertex structure of a simplex mesh yields efficient implementation of the deformable surface.

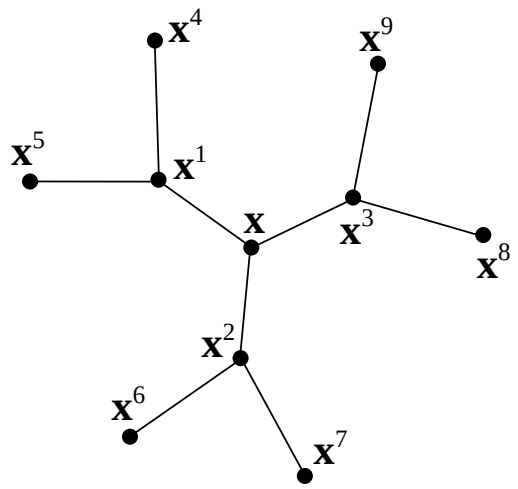

Figure A.9: Vertex structure on a simplex mesh.

Appendix B

Differential Geometry Quantities on Simplex Meshes

In this appendix, we describe how the differential geometry quantities such as Gaussian, mean, and principal curvatures can be computed from discrete surfaces represented by simplex meshes. Since these differential geometry quantities require derivatives up to the second order, the basic idea is to fit a paraboloid at each node on a simplex mesh. After the coefficients of the paraboloid are estimated using a local least square quadratic fit, all the differential geometry quantities can be computed on the paraboloid through formulas found in differential geometry textbooks (cf. [39, 78]).

In order to fit a paraboloid at a given node on the simplex mesh, we need to construct a local coordinate system at this node. To construct such a local coordinate system, we first compute the unit normal, then translate the origin of the coordinate system to the location of the given node, and rotate the coordinate system so that the normal vector points upward in the new coordinate system. These steps are now described in detail.

The unit normal at a given node $\mathbf{P}(0)$ on the simplex mesh can be approximated using the following formula

$$\mathbf{N} = \frac{\mathbf{P}(1)\times\mathbf{P}(2) + \mathbf{P}(2)\times\mathbf{P}(3) + \mathbf{P}(3)\times\mathbf{P}(1)}{||\mathbf{P}(1)\times\mathbf{P}(2) + \mathbf{P}(2)\times\mathbf{P}(3) + \mathbf{P}(3)\times\mathbf{P}(1)||} \tag{B.1}$$

where $\mathbf{P}(1), \mathbf{P}(2), \mathbf{P}(3)$ are $\mathbf{P}(0)$'s three immediate neighbors and $\times$ is the vector cross

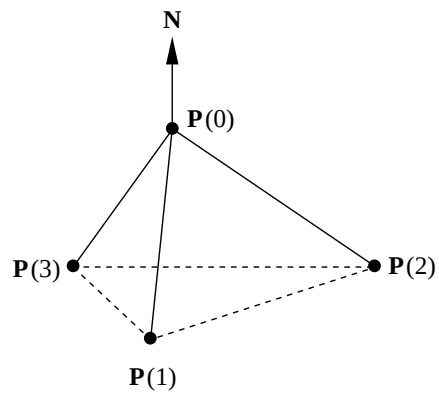

Figure B.1: Unit normal estimation using three neighboring nodes.

product (see Fig. B.1).

Let (x, y, z) be the original coordinates, (u, v, w) be the coordinates after the coordinate transformation, and (x_0, y_0, z_0) be the original coordinates of $\mathbf{P}(0)$. We also define $\mathbf{N} = (\alpha, \beta, \gamma)$ where $\sqrt{\alpha^2 + \beta^2 + \gamma^2} = 1$, and $D = \sqrt{\beta^2 + \gamma^2}$. Then the desired coordinate transformation between (x, y, z) and (u, v, w) is given by (for detail, see [44])

$$\begin{bmatrix} u \\ v \\ w \end{bmatrix} = \mathbf{R} \begin{bmatrix} x \\ y \\ z \end{bmatrix} - \begin{bmatrix} x_0 \\ y_0 \\ z_0 \end{bmatrix} \tag{B.2}$$

where

$$\mathbf{R} = \begin{bmatrix} D & -\frac{\alpha\beta}{D} & -\frac{\alpha\gamma}{D} \\ 0 & \frac{\gamma}{D} & -\frac{\beta}{D} \\ \alpha & \beta & \gamma \end{bmatrix} \text{ if } D \neq 0,$$

and

$$\mathbf{R} = \begin{bmatrix} 0 & 0 & -1 \\ 0 & 1 & 0 \\ 1 & 0 & 0 \end{bmatrix} \text{ if } D = 0.$$

We assume that the paraboloid to be fitted is expressed in the following form in

the new coordinate system:

$$\mathbf{x}(u,v) = (u,v,w) = (u,v,f(u,v)) = (u,v,h_1u + h_2v + \frac{1}{2}h_{11}u^2 + h_{12}uv + \frac{1}{2}h_{22}v^2)). \tag{B.3}$$

Let $(u_i, v_i, f(u_i, v_i)), i = 1, 2, \ldots, q$ be the coordinates of $\mathbf{P}(0)$'s neighbors and q be the number of neighbors. The coordinates of the neighbors must satisfy the following linear equations

$$\begin{bmatrix} u_1 & v_1 & \frac{1}{2}u_1^2 & u_1v_1 & \frac{1}{2}v_1^2 \\ u_2 & v_2 & \frac{1}{2}u_2^2 & u_2v_2 & \frac{1}{2}v_2^2 \\ \vdots & \vdots & \vdots & \vdots & \vdots \\ u_q & v_q & \frac{1}{2}u_q^2 & u_qv_q & \frac{1}{2}v_q^2 \end{bmatrix} \begin{bmatrix} h_1 \\ h_2 \\ h_{11} \\ h_{12} \\ h_{22} \end{bmatrix} = \begin{bmatrix} w_1 \\ w_2 \\ \vdots \\ w_q \end{bmatrix} \tag{B.4}$$

We now estimate $[h_1, h_2, h_{11}, h_{12}, h_{22}]^T$ using singular value decomposition [89].

Now we are ready to compute differential geometry quantities derived from the fitted paraboloid $\mathbf{x}(u,v) = (u,v,f(u,v))$. The first and second derivatives of $\mathbf{x}$ are computed as follows

$$\mathbf{x}_u|_{(0,0)} = (1,0,f_u)|_{(0,0)} = (1,0,h_1) \tag{B.5}$$

$$\mathbf{x}_v|_{(0,0)} = (0,1,f_v)|_{(0,0)} = (0,1,h_2) \tag{B.6}$$

$$\mathbf{x}_{uu}|_{(0,0)} = (0,0,f_{uu})|_{(0,0)} = (0,0,h_{11}) \tag{B.7}$$

$$\mathbf{x}_{uv}|_{(0,0)} = (0,0,f_{uv})|_{(0,0)} = (0,0,h_{12}) \tag{B.8}$$

$$\mathbf{x}_{vu}|_{(0,0)} = (0,0,f_{uu})|_{(0,0)} = (0,0,h_{12}) \tag{B.9}$$

$$\mathbf{x}_{vv}|_{(0,0)} = (0,0,f_{vv})|_{(0,0)} = (0,0,h_{22}). \tag{B.10}$$

The unit normal vector at $\mathbf{x}(0,0)$ is given by

$$\mathbf{n} = \frac{\mathbf{x}_u \times \mathbf{x}_v}{||\mathbf{x}_u \times \mathbf{x}_v||}|_{(0,0)} = \frac{(-h_1, -h_2, 1)}{\sqrt{1 + {h_1}^2 + {h_2}^2}}. \tag{B.11}$$

The coefficients of the first fundamental form or the elements of metric tensor $\mathbf{g}$ at $\mathbf{x}(0,0)$ are given by [78]

$$g_{11} = < \mathbf{x}_u, \mathbf{x}_u > \;=\; 1 + {h_1}^2 \tag{B.12}$$

$$g_{12} =< \mathbf{x}_u, \mathbf{x}_v > \;=\; h_1 h_2 \tag{B.13}$$

$$g_{21} =< \mathbf{x}_v, \mathbf{x}_u > \;=\; h_1 h_2 \tag{B.14}$$

$$g_{22} =< \mathbf{x}_v, \mathbf{x}_v > \;=\; 1 + {h_2}^2. \tag{B.15}$$

The coefficients of second fundamental form are given by

$$L_{11} =< \mathbf{x}_{uu}, \mathbf{n} > \;=\; \frac{h_{11}}{\sqrt{1 + {h_1}^2 + {h_2}^2}} \tag{B.16}$$

$$L_{12} =< \mathbf{x}_{uv}, \mathbf{n} > \;=\; \frac{h_{12}}{\sqrt{1 + {h_1}^2 + {h_2}^2}} \tag{B.17}$$

$$L_{21} =< \mathbf{x}_{vu}, \mathbf{n} > \;=\; \frac{h_{12}}{\sqrt{1 + {h_1}^2 + {h_2}^2}} \tag{B.18}$$

$$L_{22} =< \mathbf{x}_{vv}, \mathbf{n} > \;=\; \frac{h_{22}}{\sqrt{1 + {h_1}^2 + {h_2}^2}} \tag{B.19}$$

Hence, the Weingarten map $\mathbf{W}$ is computed by

$$\mathbf{W} = \mathbf{g}^{-1}\mathbf{L} = \begin{bmatrix} \frac{a}{\beta} & \frac{b}{\beta} \\ \frac{c}{\beta} & \frac{d}{\beta} \end{bmatrix} \tag{B.20}$$

where $\mathbf{g}$ is the metric tensor, and

$$\mathbf{L} \;=\; \begin{bmatrix} L_{11} & L_{12} \\ L_{21} & L_{22} \end{bmatrix} \tag{B.21}$$

$$\beta \;=\; \det(\mathbf{g})^{\frac{3}{2}} = (1 + {h_1}^2 + {h_2}^2)^{\frac{3}{2}} \tag{B.22}$$

$$a \;=\; h_{11} + h_{11}{h_2}^2 - h_{12}h_1h_2 \tag{B.23}$$

$$b \;=\; h_{12} + h_{12}{h_2}^2 - h_{22}h_1h_2 \tag{B.24}$$

$$c \;=\; h_{12} + h_{12}{h_1}^2 - h_{11}h_1h_2 \tag{B.25}$$

$$d \;=\; h_{22} + h_{22}{h_1}^2 - h_{12}h_1h_2. \tag{B.26}$$

Therefore the characteristic polynomial of $\mathbf{W}$ is given by

$$\lambda^2 - \frac{a+d}{\beta}\lambda + \frac{ad - bc}{\beta^2} = 0 \tag{B.27}$$

The mean curvature H and Gaussian curvature K can now be computed as

$$H = \frac{a+d}{2\beta} \;=\; \frac{(1 + {h_1}^2)h_{22} + (1 + {h_2}^2)h_{11} - 2h_1h_2h_{12}}{2(1 + {h_1}^2 + {h_2}^2)^{\frac{3}{2}}} \tag{B.28}$$

$$K = \frac{ad - bc}{\beta^2} = \frac{(h_{11}h_{22} - {h_{12}}^2)}{(1 + {h_1}^2 + {h_2}^2)^2}. \tag{B.29}$$

The principal curvatures are derived from mean curvature and Gaussian curvature as

$$k_1 = H + \sqrt{H^2 - K} \tag{B.30}$$

$$k_2 = H - \sqrt{H^2 - K} \tag{B.31}$$

where k_1 and k_2 are the maximum and minimum principal curvatures respectively.

At a nonumbilic point (where the principal curvatures are distinct), the corresponding principal directions are given by

$$\mathbf{p}_1 = \frac{(b, a - k_1\beta, 0)}{\sqrt{b^2 + (a - k_1\beta)^2}} \tag{B.32}$$

$$\mathbf{p}_2 = \frac{(b, a - k_2\beta, 0)}{\sqrt{b^2 + (a - k_2\beta)^2}}. \tag{B.33}$$

Bibliography

[1] A. J. Abrantes and J. S. Marques, "A class of constrained clustering algorithms for object boundary extraction," *IEEE Trans. on Image Processing*, vol. 5, pp. 1507–1521, Nov. 1996.

[2] M. K. Agoston, *Algebraic Topology — A first course*. New York: Marcel Dekker, Inc., 1976.

[3] L. Alvarez, F. Guichard, P. L. Lions, and J. M. Morel, "Axioms and fundamental equations of image processing," *Archive for Rational Mechanics and Analysis*, vol. 123, no. 3, pp. 199–257, 1993.

[4] W. F. Ames, *Numerical Methods for Partial Differential Equations*. Boston: Academic Press, 3rd ed., 1992.

[5] A. A. Amini, T. E. Weymouth, and R. C. Jain, "Using dynamic programming for solving variational problems in vision," *IEEE Trans. on Pattern Anal. Machine Intell.*, vol. 12, no. 9, pp. 855–867, 1990.

[6] W. A. Barrett and E. N. Mortensen, "Interactive live-wire boundary extraction," *Medical Image Analysis*, vol. 1, no. 4, pp. 331–341, 1997.

[7] B. G. Baumgart, "A polyhedron representation for computer vision," *Proc. of the National Computer Conference*, pp. 589–596, 1975.

[8] A. Blake and A. Zisserman, *Visual Reconstruction*. Boston: MIT Press, 1987.

[9] H. Blum and R. N. Nagel, "Shape description using weighted symmetric axis features," *Pattern Recognition*, vol. 10, pp. 167–180, 1978.

[10] F. L. Bookstein, "Principal warps: Thin-plate splines and the decomposition of deformations," *IEEE Trans. on Pattern Anal. Machine Intell.*, vol. 11, no. 6, pp. 567–585, 1989.

[11] V. Caselles, F. Catte, T. Coll, and F. Dibos, "A geometric model for active contours," *Numerische Mathematik*, vol. 66, pp. 1–31, 1993.

[12] V. Caselles, R. Kimmel, and G. Sapiro, "Geodesic active contours," in *Proc. Fifth Int. Conf. on Comp. Vis.*, pp. 694–699, 1995.

[13] E. L. Chaney and S. M. Pizer, "Defining anatomical structures from medical images," *Seminar in Radiation Oncology*, vol. 2, pp. 215–225, Oct. 1992.

[14] A. H. Charles and T. A. Porsching, *Numerical Analysis of Partial Differential Equations.* Englewood Cliffs, New Jersey: Prentice Hall, 1990.

[15] G. E. Christensen, S. C. Joshi, and M. I. Miller, "Volumetric transformation of brain anatomy," *IEEE Trans. Med. Imag.*, vol. 16, no. 6, pp. 864–877, 1997.

[16] G. E. Christensen, R. D. Rabbit, M. Miller, S. C. Joshi, U. Grenander, T. Coogan, and D. V. Essen, "Topological properties of smooth anatomic maps," in *Information Processing in Medical Imaging*, pp. 101–112, 1995.

[17] G. E. Christensen, R. D. Rabbitt, and M. I. Miller, "Deformable templates using large deformation kinematics," *IEEE Trans. on Image Processing*, vol. 5, pp. 1435–1447, Oct. 1996.

[18] C. A. Cocosco, V. Kollokian, R. K. S. Kwan, and A. C. Evans, "BrainWeb: Online interface to a 3D MRI simulated brain database," *Neuroimage*, vol. 5, no. 4, 1997. http://www.bic.mni.mcgill.ca/brainweb.

[19] I. Cohen, L. D. Cohen, and N. Ayache, "Using deformable surfaces to segment 3-D images and infer differential structures," *CVGIP: Image Understanding*, vol. 56, pp. 242–263, Sept. 1992.

[20] L. D. Cohen, "On active contour models and balloons," *CVGIP: Image Understanding*, vol. 53, pp. 211–218, Mar. 1991.

[21] L. D. Cohen and I. Cohen, "Finite-element methods for active contour models and balloons for 2-D and 3-D images," *IEEE Trans. on Pattern Anal. Machine Intell.*, vol. 15, pp. 1131–1147, Nov. 1993.

[22] D. Collins, C. Holmes, T. Peters, and A. Evans, "Automatic 3-D model-based neuroanatomical segmentation," *Human Brain Mapping*, vol. 3, pp. 190–208, 1995.

[23] B. R. Condon, J. Patterson, *et al.*, "Image non-uniformity in magnetic resonance imaging: its magnitude and methods for its correction," *The British Journal of Radiology*, vol. 60, pp. 83–87, 1989.

[24] T. F. Cootes, C. J. Taylor, D. H. Cooper, and J. Graham, "Active shape models – their training and application," *Computer Vision and Image Understanding*, vol. 61, no. 1, pp. 38–59, 1995.

[25] R. Courant and D. Hilbert, *Methods of Mathematical Physics*, vol. 1. New York: Interscience, 1953.

[26] R. Courant and D. Hilbert, *Methods of Mathematical Physics*, vol. 2. New York: Interscience, 1989.

[27] A. M. Dale and M. I. Sereno, "Improved localization of cortical activity combining EEG and MEG with MRI cortical surface reconstruction: A linear approach," *J. Cogn. Neuroscience*, vol. 5, no. 2, pp. 162–176, 1993.

[28] C. Davatzikos, *Model-Based Boundary Mapping with Applications to Medical Imaging.* PhD thesis, The Johns Hopkins University, Baltimore, Maryland, 1994.

[29] C. Davatzikos, "Spatial normalization of 3D images using deformable models," *Journal of Computer Assisted Tomography*, vol. 20, no. 4, pp. 656–665, 1996.

[30] C. Davatzikos, "Spatial transformation and registration of brain images using elastically deformable models," *Computer Vision and Image Understanding*, vol. 66, pp. 207–222, May 1997.

[31] C. Davatzikos and R. N. Bryan, "Using a deformable surface model to obtain a shape representation of the cortex," *IEEE Trans. Med. Imag.*, vol. 15, pp. 785–795, Dec. 1996.

[32] C. Davatzikos and J. L. Prince, "Convexity analysis of active contour models," in *Proc. Conf. on Info. Sci. and Sys.*, pp. 581–587, 1994.

[33] C. Davatzikos and J. L. Prince, "An active contour model for mapping the cortex," *IEEE Trans. on Medical Imaging*, vol. 14, pp. 65–80, Mar. 1995.

[34] L. Davis, *Genetic Algorithms and Simulated Annealing.* London: Pitman, 1987.

[35] B. M. Dawant, A. P. Zijidenbos, and R. A. Margolin, "Correction of intensity variations in MR images for computer-aided tissue classification," *IEEE Trans. Med. Imag.*, vol. 12, pp. 770–781, 1993.

[36] H. Delingette, "Adaptive and deformable models based on simplex meshes," in *Proceedings of the 1994 IEEE Workshop on Motion of Non-Rigid and Articulated Objects*, pp. 152–157, 1994.

[37] H. Delingette, "Simplex meshes: a general representation for 3D shape reconstruction," Tech. Rep. TR2214, I.N.R.I.A., Sophia-Antipolis, France, Mar. 1994.

[38] H. Delingette, "Simplex meshes: a general representation for 3D shape reconstruction," in *Proc. IEEE Conf. Computer Vision and Pattern Recognition*, pp. 856–859, June 1994.

[39] M. P. do Carmo, *Differential Geometry of Curves and Surfaces.* Englewood Cliffs, NJ: Prentice-Hall, 1976.

[40] D. Doo and M. Sabin, "Behaviour of recursive division surfaces near extraordinary points," *Computer-Aided Design*, vol. 10, no. 6, pp. 356–360, 1978.

[41] H. A. Drury and D. C. V. Essen, "Functional specializations in human cerebral cortex analyzed using the visible man surface-based atlas," *Human Brain Mapping*, vol. 5, pp. 233–237, 1997.

[42] H. A. Drury, D. C. V. Essen, C. H. Anderson, C. W. Lee, T. A. Coogan, and J. W. Lewis, "Computerized mappings of the cerebral cortex: A multiresolution flattening method and a surface-based coordinate system," *J. Cogn. Neuroscience*, pp. 1–28, 1996.

[43] M. A. Fischler and R. A. Elschlager, "The representation and matching of pictorial structures," *IEEE Trans. on Computers*, vol. 22, no. 1, pp. 67–92, 1973.

[44] J. D. Foley, A. van Dam, S. K. Feiner, and J. F. Hughes, *Computer Graphics: Principles and Practice.* Reading, MA: Addison-Wesley, 2nd ed. ed., 1990.

[45] S. Geman and D. Geman, "Stochastic relaxation, Gibbs distrutions, and the Bayesian restoration of images," *IEEE Trans. on Pattern Anal. Machine Intell.*, vol. 6, pp. 721–741, 1984.

[46] A. F. Goldszal, C. Davatzikos, D. L. Pham, M. X. H. Yan, R. N. Bryan, and S. M. Resnick, "An image processing system for qualitative and quantitative volumetric analysis of brain images," *Journal of Computer Assisted Tomography*, to appear.

[47] R. C. Gonzalez and R. E. Woods, *Digital Image Processing.* Reading, MA: Addison-Wesley, 1993.

[48] L. D. Griffin, "The intrinsic geometry of the cerebral cortex," *Journal of Theoretical Biology*, vol. 166, no. 3, pp. 261–273, 1994.

[49] W. E. L. Grimson, *Ojbect Recognition by Computer: The Role of Geometric Constraints.* Cambridge, MA: MIT Press, 1990.

[50] W. E. L. Grimson, G. J. Ettinger, T. Kapur, M. E. Leventon, W. M. W. III, and R. Kikinis, "Utilizing segmented mri data in image-guided surgery," *Int. J. Pattern Recog. Artif. Intell.*, vol. 11, no. 8, pp. 1367–1397, 1996.

[51] S. N. Gupta and J. L. Prince, "Stochastic models for DIV-CURL optical flow methods," *IEEE Signal Processing Letters*, vol. 3, no. 2, pp. 32–35, 1996.

[52] K. E. Gustafson, *Partial Differential Equations.* New York: John Wiley & Sons, 2 ed., 1987.

[53] B. Heinrich, *Finite Difference Methods on Irregular Networks. A Generalized Approach to Second Order Elliptic Problems.* Basel, Switzerland: Birkhäuser Verlag, 1987.

[54] F. B. Hilderbrand, *Methods of Applied Mathematics.* Englewood Cliffs, NJ: Prentice-Hall, 2 ed., 1965.

[55] H. Hoppe, *Surface Reconstruction from Unorganized Points.* PhD thesis, Department of Computer Science and Engineering, University of Washington, June 1994.

[56] B. K. P. Horn, *Robot Vision.* Cambridge, MA: MIT Press, 1986.

[57] B. K. P. Horn and B. G. Schunck, "Determining optical flow," *Artificial Intelligence*, vol. 17, pp. 185–203, 1981.

[58] A. K. Jain, *Fundamentals of Digital Image Processing.* Englewood Cliffs, NJ: Prentice-Hall, 1989.

[59] S. Joshi, J. Wang, M. I. Miller, D. C. V. Essen, and U. Grenander, "On the differential geometry of the cortical surface," in *Proc. of the SPIE: Vision Geometry IV*, vol. 2573, pp. 304–311, Aug. 1995.

[60] A. D. Kalvin, C. B. Cutting, B. Haddad, and M. Noz, "Constructing topologically connected surfaces for the comprehensive analysis of 3D medical struc-

tures," in *SPIE Proc. Medical Imaging V: Image Processing*, vol. 1445, pp. 247–258, Feb. 1991.

[61] T. Kapur, E. Grimson, W. Wells, and R. Kikinis, "Segmentation of brain tissue from magnetic resonance images," *Medical Image Analysis*, vol. 1, no. 2, pp. 109–127, 1996.

[62] M. Kass, A. Witkin, and D. Terzopoulos, "Snakes: Active contour models," *Int. J. Computer Vision*, vol. 1, no. 4, pp. 321–331, 1987.

[63] B. B. Kimia, A. R. Tannenbaum, and S. W. Zucker, "Shapes, shocks, and deformations I: The components of two-dimensional shape and the reaction-diffusion space," *Int. J. Computer Vision*, pp. 189–224, 1995.

[64] R. Kimmel, A. Amir, and A. M. Bruckstein, "Finding shortest paths on surfaces using level sets propagation," *IEEE Trans. on Pattern Anal. Machine Intell.*, vol. 17, no. 6, pp. 635–640, 1995.

[65] G. J. Klein, P. T. S. X. Teng, and T. F. Budinger, "A sensitivity analysis of brain morphometry based on MRI-derived surface models," in *Proc. SPIE Medical Imaging '98*, vol. 3337, p. 31, 1998. abstract.

[66] A. C. W. Kotcheff and C. J. Taylor, "Automatic construction of eigenshape models by genetic algorithm," in *the XVth Int. Conf. Inf. Proc. Med. Imag. (IPMI)*, pp. 1–14, Springer-Verlag, 1997.

[67] F. Kruggel and G. Lohmann, "Automatical adaption of the stereotactical coordinate system in brain MRI datasets," in *the XVth Int. Conf. Inf. Proc. Med. Imag. (IPMI)*, pp. 471–476, Springer-Verlag, 1997.

[68] B. Leroy, I. Herlin, and L. D. Cohen, "Multi-resolution algorithms for active contour models," in *12th International Conference on Analysis and Optimization of Systems*, pp. 58–65, 1996.

[69] F. Leymarie and M. D. Levine, "Tracking deformable objects in the plane using an active contour model," *IEEE Trans. on Pattern Anal. Machine Intell.*, vol. 15, no. 6, pp. 617–634, 1993.

[70] S. Lobregt and M. A. Viergever, "A discrete dynamic contour model," *IEEE Trans. on Medical Imaging*, vol. 14, pp. 12–24, Mar. 1995.

[71] W. E. Lorensen and H. E. Cline, "Marching cubes: A high-resolution 3D surface construction algorithm," *ACM Comp. Graph.*, vol. 21, no. 4, pp. 163–170, 1987.

[72] D. MacDonald, D. Avis, and A. C. Evans, "Multiple surface identification and matching in magnetic resonance images," in *SPIE Proc. VBC '94*, vol. 2359, pp. 160–169, 1994.

[73] R. Malladi, J. A. Sethian, and B. C. Vemuri, "Shape modeling with front propagation: A level set approach," *IEEE Trans. on Pattern Anal. Machine Intell.*, vol. 17, no. 2, pp. 158–175, 1995.

[74] J. F. Mangin, V. Frouin, I. Bloch, J. Regis, and J. Lopez-Krahe, "From 3D magnetic resonance images to structural representations of the cortex topography using topology preserving deformations," *Mathematical Imaging and Vision*, vol. 5, pp. 297–318, 1995.

[75] D. Marr, *Vision. A computational investigation into the human representation and processing of visual information.* Freeman, 1982.

[76] T. McInerney and D. Terzopoulos, "A dynamic finite element surface model for segmentation and tracking in multidimensional medical images with application to cardiac 4D image analysis," *Computerized Medical Imaging and Graphics*, vol. 19, no. 1, pp. 69–83, 1995.

[77] T. McInerney and D. Terzopoulos, "Deformable models in medical image analysis: a survey," *Medical Image Analysis*, vol. 1, no. 2, pp. 91–108, 1996.

[78] R. S. Millman and G. D. Parker, *Elements of Differential Geometry.* Englewood Cliffs, NJ: Prentice-Hall, 1977.

[79] C. Montani, R. Scateni, and R. Scopigno, "Discretized marching cubes," in *IEEE Proc. Visualization'94*, pp. 281–287, 1994.

[80] P. M. Morse and H. Feshbach, *Methods of Theoretical Physics.* New York: McGraw-Hill Book Company, 1953.

[81] D. Mumford and J. Shah, "Boundary detection by minimizing functionals," in *Proc. IEEE Conf. Computer Vision and Pattern Recognition*, pp. 22–26, 1985.

[82] J. Neider, T. Davis, and M. Woo, *OpengGL Programming Guide.* Reading, MA: Addison-Wesley, 1993.

[83] W. Neuenschwander, P. Fua, G. Szekely, and O. Kubler, "Making snakes converge from minimal initialization," in *ARPA Image Understanding Workshop*, pp. 1627–1636, 1994.

[84] D. L. Pham and J. L. Prince, "An adaptive fuzzy c-means algorithm for image segmentation in the presence of intensity inhomogeneities," in *SPIE Medical Imaging '98: Image Processing*, SPIE, Feb. 21-27, 1998.

[85] D. Pham and J. Prince, "An adaptive fuzzy c-means algorithm for image segmentation in the presence of intensity inhomogeneities," to appear in *Pattern Recognition Letters*, 1998.

[86] D. Pham and J. Prince, "Adaptive fuzzy segmentation of magnetic resonance images," submitted to *IEEE Trans. on Medical Imaging*, 1998.

[87] S. M. Pizer, C. A. Burbeck, J. M. Coggins, D. S. Fritsch, and B. S. Morse, "Object shape before boundary shape: Scale-space medial axes," *Journal of Mathematical Imaging and Vision*, vol. 4, pp. 303–313, 1994.

[88] S. M. Pizer, W. R. Oliver, and S. H. Bloomberg, "Hierarchical shape description via the multiresolution symmetric axis transform," *IEEE Trans. on Pattern Anal. Machine Intell.*, vol. 9, pp. 505–511, July 1987.

[89] W. H. Press, B. P. Flannery, S. A. Teukolsky, and W. T. Vetterling, *Numerical Recipes.* Cambridge: Cambridge University Press, 1986.

[90] J. L. Prince and C. Xu, "A new external force model for snakes," in *1996 Image and Multidimensional Signal Processing Workshop*, pp. 30–31, 1996.

[91] J. Rademacher, A. M. Galaburda, D. N. Kennedy, P. A. Filipek, and J. V. S. Caviness, "Human cerebral cortex: Localization, parcellation, and morphometry with magnetic resonance imaging," *Journal of Cognitive Neuroscience*, vol. 4, pp. 352–374, 1992.

[92] J. Rauch, *Partial Differential Equation.* New York: Springer-Verlag, 1991.

[93] R. Ronfard, "Region-based strategies for active contour models," *Int. J. Computer Vision*, vol. 13, no. 2, pp. 229–251, 1994.

[94] S. Sandor and R. Leahy, "Towards automated labelling of the cerebral cortex using a deformable atlas," in *Information Processing in Medical Imaging*, pp. 127–138, 1995.

[95] S. Sandor and R. Leahy, "Surface-based labeling of cortical anatomy using a deformable atlas," *IEEE Trans. Med. Imag.*, vol. 16, no. 1, pp. 41–54, 1997.

[96] G. Sapiro and A. Tannenbaum, "Affine invariant scale-space," *Int. J. Computer Vision*, vol. 11, no. 1, pp. 25–44, 1993.

[97] W. Schroeder, K. Martin, and B. Lorensen, *The Visualization Toolkit.* Englewood Cliffs, NJ: Prentice-Hall, 2nd ed. ed., 1997.

[98] S. Sclaroff and A. Pentland, "On model modeling for medical images: Underconstrained shape description and data compression," in *Proc. of IEEE Workshop on Biomedical Image Analysis*, pp. 70–79, 1994.

[99] N. W. Shock, R. C. Greulich, R. Andres, D. Arenberg, P. T. Costa Jr., E. Lakatta, and J. D. Tobin, "Normal human aging: The Baltimore longi-

tudinal study of aging." U.S. Governement Printing Office, Washington, D.C., 1984.

[100] L. H. Staib and J. S. Duncan, "Boundary finding with parametrically deformable models," *IEEE Trans. on Pattern Anal. Machine Intell.*, vol. 14, no. 11, pp. 1061–1075, 1992.

[101] L. H. Staib and J. S. Duncan, "Deformable Fourier models for surface finding in 3D images," in *Proc. Second Conf. on Visualization in Biomedical Computing*, vol. SPIE Proc., Vol. 1808, pp. 90–104, 1992.

[102] J. Talairach and P. Tournoux, *Co-Planar Stereotaxic Atlas of the Human Brain. 3-Dimensional Proportional System: An Approach to Cerebral Imaging.* Stuttgart, NY: Thieme Medical Publisher, Inc., 1988.

[103] H. Tek and B. B. Kimia, "Image segmentation by reaction-diffusion bubbles," in *Proc. Fifth Int. Conf. on Comp. Vis.*, pp. 156–162, 1995.

[104] P. C. Teo, G. Sapiro, and B. A. Wandell, "Creating connected representations of cortical gray matter for functional MRI visualization," *IEEE Trans. Med. Imag.*, vol. 16, no. 6, pp. 852–863, 1997.

[105] D. Terzopoulos, "On matching deformable models to images." Tech. Rept. 60. Schlumberger Palo Alto research. 1986. Reprinted in *Topical Meeting on Machine Vision*, Technical Digest Series, Vol. 12, 1987, 160-167.

[106] D. Terzopoulos and K. Fleischer, "Deformable models," *The Visual Computer*, vol. 4, pp. 306–331, 1988.

[107] D. Terzopoulos and R. Szeliski, "Tracking with Kalman snakes," in *Active Vision* (A. Blake and A. Yuille, eds.), Artificial Intelligence, pp. 3–20, Cambridge, Massachusetts: The MIT Press, 1992.

[108] D. Terzopoulos, A. Witkin, and M. Kass, "Constraints on deformable models: Recovering 3D shape and nonrigid motion," *Artificial Intelligence*, vol. 36, no. 1, pp. 91–123, 1988.

[109] P. Thompson and A. W. Toga, "A surface-based technique for warping three-dimensional images of the brain," *IEEE Trans. on Medical Imaging*, vol. 15, pp. 402–417, Aug. 1996.

[110] M. Vaillant, C. Davatzikos, R. H. Taylor, and R. N. Bryan, "A path-planning algorithm for image-guided neurosurgery," in *Lecture Notes in Comp. Sci.:CVRMed-MRCAS'97*, vol. 1205, pp. 467–476, Mar. 1997.

[111] A. van Gelder and J. Wilhelms, "Topological considerations in isosurface generation," *ACM Trans. on Graphics*, vol. 13, pp. 337–375, 1994.

[112] D. von Seggern, *Practical Handbook of Curve Design and Generation.* CRC Press, Inc., 1994.

[113] R. Whitaker, "Volumetric deformable models: Active blobs," Tech. Rep. ECRC-94-25, European Computer-Industry Research Centre GmbH, 1994.

[114] B. Widrow, "The "rubber-mask" technique," *Pattern Recognition*, vol. 5, pp. 175–211, 1973.

[115] C. Xu, M. E. Etemad, D. N. Yu, D. L. Pham, and J. L. Prince, "A spherical map for cortical geometry." *4th International conference on Functional Mapping of the Human Brain (HBM)*, June 7-12, 1998; *NeuroImage* 7(4):734, 1998.

[116] C. Xu, D. L. Pham, M. E. Etemad, D. N. Yu, and J. L. Prince, "Reconstruction of the human cerebral cortex from magnetic resonance images." submitted to *IEEE Trans. on Medical Imaging* on September 8, 1998.

[117] C. Xu, D. L. Pham, and J. L. Prince, "Reconstruction of the human cortical surface from MR images." *4th International conference on Functional Mapping of the Human Brain (HBM)*, June 7-12, 1998; *NeuroImage* 7(4):715, 1998.

[118] C. Xu, D. L. Pham, and J. L. Prince, "Finding the brain cortex using fuzzy segmentation, isosurfaces, and deformable surface models," in *the XVth Int. Conf. Inf. Proc. Med. Imag. (IPMI)*, pp. 399–404, Springer-Verlag, 1997.

[119] C. Xu, D. L. Pham, J. L. Prince, M. E. Etemad, and D. N. Yu, "Reconstruction of the human cortical surface from MR images," in *Proc. of the First International Conference on Medical Image Computing and Computer Assisted Interventions (MICCAI)*, pp. 482–488, 1998.

[120] C. Xu and J. L. Prince, "A generalized gradient vector flow for active contour models," in *1997 Conf. Info. Sci. Syst., Johns Hopkins University*, pp. 885–890, 1997.

[121] C. Xu and J. L. Prince, "Gradient vector flow: A new external force for snakes," in *IEEE Proc. Conf. on Comp. Vis. Patt. Recog. (CVPR)*, pp. 66–71, 1997.

[122] C. Xu and J. L. Prince, "Generalized gradient vector flow external forces for active contours," *Signal Processing, An International Journal*, vol. 71, no. 2, pp. 132–139, 1998.

[123] C. Xu and J. L. Prince, "Snakes, shapes, and gradient vector flow," *IEEE Trans. on Image Processing*, vol. 7, pp. 359–369, Mar. 1998.

[124] A. L. Yuille, D. S. Cohen, and P. Hallinan, "Feature extraction from faces using deformable templates," *Int. J. Computer Vision*, vol. 8, pp. 99–112, 1992.

[125] S. C. Zhu and A. Yuille, "Region competition: Unifying snakes, region growing and bayes/mdl for multiband image segmentation," *IEEE Trans. on Pattern Anal. Machine Intell.*, vol. 18, no. 9, pp. 884–900, 1996.

[126] D. Zorin, P. Schröder, and W. Sweldens, "Interpolating subdivision for meshes with arbitrary topology," in *Proc. SIGGRAPH 1996, ACM SIGGRAPH*, pp. 189–192, 1996.

List of Publications

- Journal articles

  1. D. L. Pham, J. L. Prince, A. P. Dagher, and C. Xu. An automated technique for statistical characterization of brain tissues in magnetic resonance imaging. *International Journal of Pattern Recognition and Artificial Intelligence*, 11(8):1189-1211, 1997.
  2. C. Xu and J. L. Prince. Snakes, shapes, and gradient vector flow. *IEEE Trans. on Image Processing*, 7(3):359–369, March 1998.
  3. C. Xu and J. L. Prince. Generalized gradient vector flow external forces for active contours. *Signal Processing, An International Journal*, 71(2):132–139, December 1998.
  4. C. Xu, D. L. Pham, J. L. Prince, M. E. Etemad, and D. N. Yu. Reconstruction of the human cerebral cortex from magnetic resonance images. Submitted for publication in *IEEE Trans. on Medical Imaging*.

- Invited book chapters

  1. D. L. Pham, C. Xu, and J. L. Prince. Current Methods in Medical Image Segmentation. *Annual Review of Biomedical Engineering*, vol. 1, Jan. 1999. Submitted.
  2. J. L. Prince and C. Xu. Gradient Vector Flow Deformable Models. *Handbook of Medical Imaging*, edited by I. Bankman. In preparation.
  3. J. L. Prince and C. Xu. Deformable Models. *SPIE Handbook on Medical Imaging – Volume III: Medical Image Analysis*, edited by J.M. Fitzpatrick and M. Sonka. In preparation.

- Conference papers

  1. J. L. Prince and C. Xu. A new external force model for snakes. In *the Image and Multidimensional Signal Processing Workshop*, pages 30–31, 1996.

2. C. Xu and J. L. Prince. Gradient vector flow: A new external force for snakes. In *IEEE Proc. Conf. on Comp. Vis. Patt. Recog. (CVPR)*, pages 66–71, 1997.

3. C. Xu, D. L. Pham, and J. L. Prince. Finding the brain cortex using fuzzy segmentation, isosurfaces, and deformable surface models. In *Proc. of the XVth Int. Conf. Inf. Proc. Med. Imag. (IPMI)*, pages 399–404. Springer-Verlag, 1997.

4. C. Xu and J. L. Prince. A generalized gradient vector flow for active contour models. In *1997 Conf. Info. Sci. Syst., Johns Hopkins University*, pages 885–890, 1997.

5. J. L. Prince and C. Xu. Nonconservative force models in active geometry. To appear in *the IEEE Image and Multidimensional Digital Signal Processing (IMDSP) Workshop*, 1998.

6. C. Xu, D. L. Pham, J. L. Prince, M. E. Etemad, and D. N. Yu. Reconstruction of the human cortical surface from MR images. In *Proc. of the First International Conference on Medical Image Computing and Computer Assisted Interventions (MICCAI)*, pages 482–488, 1998.

- Abstracts

1. C. Xu, D. L. Pham, and J. L. Prince. Reconstruction of the human cortical surface from MR images. *4th Int. Conf. on Functional Mapping of the Human Brain*, June 7-12, 1998; *NeuroImage* 7(4):715, 1998.

2. C. Xu, M. E. Etemad, D. N. Yu, D. L. Pham, and J. L. Prince. A spherical map for cortical geometry. *4th Int. Conf. on Functional Mapping of the Human Brain*, June 7-12, 1998; *NeuroImage* 7(4):734, 1998.

Vita

Chenyang Xu was born in Yinchuan, Ningxia, P.R. China on April 19, 1970. He received the B.S. degree in computer science and engineering from the University of Science and Technology of China, Hefei, Anhui, P.R. China, in 1993, and the M.S.E. degree in electrical and computer engineering from The Johns Hopkins University, Baltimore, Maryland, in 1995. He is currently pursuing the Ph.D. degree in electrical and computer engineering at The Johns Hopkins University. His research interests include image processing and analysis, medical imaging, computer vision, computer graphics, deformable models, and brain mapping.